ABSTRACT

Title of Document: NOVEL ELECTROANALYTICAL TECHNIQUES AND IN SITU HIGH RESOLUTION TRANSMISSION ELECTRON MICROSCOPY INVESTIGATION FOR PHASE TRANSFORMATION ELECTRODE MATERIALS

Yujie Zhu, Doctor of Philosophy, 2013

Directed By: Associate Professor Chunsheng Wang,
Department of Chemical and Biomolecular Engineering

Lithium ion (Li-ion) batteries are currently being used to power an increasingly diverse range of applications, and have been recognized as a critical enabling technology to make electric vehicle/hybrid electric vehicle (EV/HEV) a success. It has been found that phase transformation electrode materials (such as $LiFePO_4$) are the promising electrode materials for high power Li-ion batteries. However the mechanism of the exceptional rate performance is still undergoing debates, since there is no accurate analysis method to study ion transport phenomena in the phase transformation regions. The analysis methods of current electrochemical techniques, including galvanostatic intermittent titration technique (GITT), potentiostatic intermittent titration technique (PITT), cyclic voltammetry (CV), and electrochemical impedance spectroscopy (EIS), can only be used to analyze the ion transport in solid

solution electrode materials, because they were developed mainly based on Fick's second law of diffusion without any consideration of the inter-phase boundary movement in phase transformation electrode materials.

Motivated by the increasing demand for accurate analysis methods for electroanalytical techniques and recent advances in the theory of phase transformation, a mixed-control phase transformation model is proposed by us. The mixed-control model accounts not only the ion diffusion, but also the phase boundary mobility that depends on the interface coherence, misfit strain/stress, deformations and defects. With $LiFePO_4$ as a specific example, we study the potential hysteresis and strain accommodation energy. By integrating the mixed-control model with GITT, PITT and CV, we determine the Li-ion diffusion coefficient and interface mobility of $LiFePO_4$ electrodes in two-phase region. For the first time, the interface mobility of $LiFePO_4$ is obtained.

The electrochemical lithiation of $FePO_4$ particles is investigated by *in situ* high resolution transmission electron microscopy (HRTEM), and the anisotropic lithiation mechanism is directly observed. For the first time, a sharp (010) phase boundary between $LiFePO_4$ and $FePO_4$ is observed, which migrates along the [010] direction during lithiation. Furthermore, our *in situ* HRTEM observations revealed misfit dislocation populations on the (010) phase boundary, overthrowing previous model assumption of fully coherent phase boundary. These misfit dislocations provide a mechanism for long-term lithium ion battery electrode fatigue and failure, due to repeated coherency loss.

NOVEL ELECTROANALYTICAL TECHNIQUES AND IN SITU HIGH RESOLUTION TRANSMISSION ELECTRON MICROSCOPY INVESTIGATION FOR PHASE TRANSFORMATION ELECTRODE MATERIALS

By

Yujie Zhu

Dissertation submitted to the Faculty of the Graduate School of the
University of Maryland, College Park, in partial fulfillment
of the requirements for the degree of
Doctor of Philosophy
2013

Advisory Committee:
Associate Professor Chunsheng Wang, Chair
Professor Raymond A. Adomaitis
Associate Professor Panagiotis Dimitrakopoulos
Assistant Professor Dongxia Liu
Professor Gregory Jackson, Dean's Representative

Dedicated to my family and Tong Meng.

Acknowledgements

First, I would like to sincerely thank my advisor, Prof. Chunsheng Wang, who gave me unreserved guidance, support and encouragement throughout my Ph.D. study period. His knowledge in electrochemistry, materials science and batteries helped me solve numerous research problems, and his enthusiasm for science and creative thinking will influence me on my whole career.

Second, I want to express my appreciations on my previous and current colleagues, Dr. Juchen Guo, Dr. Yunhua Xu, Dr. Xilin Chen, Ms. Yanting Luo, Mr. Yihang Liu, Mr. Alex Langrock, Ms. Yang Wen, Mr. Chao Luo and Ms. Ying Liu, who have been creating a warm and comfortable working atmosphere during the past five years. Moreover, I am deeply thankful to all my collaborators in Sandia National Laboratory and Massachusetts Institute of Technology, Dr. Jianyu Huang, Mr. Jiangwei Wang, Dr. Yang Liu, Dr. Xiaohua Liu, Dr. Akihiro Kushima and Prof. Ju Li, who have given me lots of help on the *in situ* TEM study and the corresponding manuscript preparation. I have learnt a lot from them through many insightful discussions.

I would also like to acknowledge Army Research Office and National Science Foundation for their financial support for my Ph.D. program.

Finally, I would like to thank my families, Tong Meng and all my dear friends for their unconditional love and support through all these years.

Table of Contents

List of Tables

List of Figures

List of Illustrations

Chapter 1: Background and Introduction

Fossil fuels currently are dominating the energy markets, especially in the automobile business. Most of modern vehicles are propelled by an internal combustion engine, fueled by gasoline, which causes greenhouse effect and contributes to climate change and global warming. Considering the emission of greenhouse gases, depletion of natural resources and rapid increase of oil price, alternative power systems are urgently needed. Over the past decades, a large amount of effort has been made to develop carbon-free and renewable energy sources, such as solar, wind and ocean (wave, currents and tides), etc. However, these renewable energy sources are seasonal and intermittent, so they usually need to be converted into electricity for storage and future use.

Lithium ion (Li-ion) batteries are currently being used to power an increasingly diverse range of applications, and have been recognized as a critical enabling technology to make electric vehicle/hybrid electric vehicle (EV/HEV) a success [1]. Compared to traditional battery systems, such as lead-acid, Ni-Cd and Ni-MH batteries, Li-ion batteries possess the highest energy densities (both gravimetric and volumetric) and also feature no memory effect and slow self-discharge, which make them popular in both consumer electronics and military use [2]. For most electrode materials in Li-ion batteries, phase transitions are usually involved in the charge-discharge processes of these electrode materials because their lithiated phase and delithiated phase usually have different structure properties (such as crystal structures and lattice parameters, etc.). Recently, it has been reported that phase transformation electrode materials (such as $LiFePO_4$, $Li_4Ti_5O_{12}$) have superior power densities compared to traditional $LiCoO_2$ and are the promising electrode materials for high power Li-ion batteries [3-5]. However the mechanism of the exceptional rate performance is still a controversial issue undergoing debates [3-7], since there is no accurate electroanalytical technique to probe ion transport phenomena in the phase transformation regions. The analysis methods of current electrochemical techniques, including galvanostatic intermittent titration technique (GITT) [8], potentiostatic intermittent titration technique (PITT) [8], cyclic voltammetry (CV) [9], and electrochemical impedance spectroscopy (EIS) [10], can only be used to analyze the ion transport in solid solution electrode materials, because they were developed mainly based on Fick's second law of diffusion without any consideration of the effect of inter-phase boundary movement on the ion transport in phase transformation electrode materials. The lack of accurate and reliable analysis methods for these electrochemical techniques has seriously delayed the development of Li-ion batteries based on the high-power phase transformation electrode materials. The main objective of this research is to develop novel electroanalytical methods that enable to precisely interpret the results of phase transformation electrode materials under different electrochemical techniques and to discover the precise structure-phase transformation-property relationships in phase transformation electrode materials and to fundamentally understand the phase transformation phenomena and develop next-generation of high power electrode materials.

1.1. A Li-Ion Battery System

A typical Li-ion battery consists of three main components: anode, electrolyte and cathode. Figure 1.1 is a schematic illustration of the operating principles of a Li-ion battery. During discharge, Li ions were extracted from anode materials (such as graphite, Si, etc.) and diffused through the electrolyte, which usually is a lithium salt dissolved in organic solvents (such as $LiPF_6$ in ethylene carbonate (EC) and dimethyl carbonate (DMC)), then inserted into the cathode materials (such as $LiCoO_2$, $LiFePO_4$, etc.). Meanwhile, the electrons moved from anode to cathode through the outer circuit, providing power for the outer circuit. During charge process, Li ions and electrons would move back from cathode to anode through the electrolyte and outer circuit, respectively.

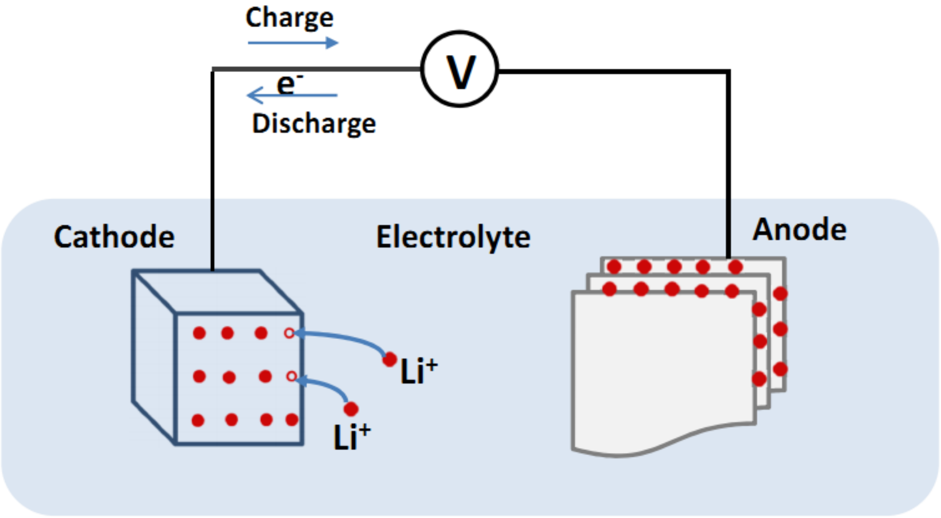

Figure 1.1. Schematic illustration of a lithium-ion battery system.

1.1.1. Anode Materials

The current choices of anode materials for Li-ion batteries mainly contain three categories [11]: alloy anode (Si, Sn etc.), carbon based materials (graphite, hard carbon etc.) and some new anode materials (such as TiO_2, $Li_4Ti_5O_{12}$). Table 1.1 shows the electrochemical properties for some major anode materials in Li-ion batteries.

Table 1.1. Properties of some typical anode materials for Li-ion batteries.

Materials / Properties	Li metal	Graphite (C)	$Li_4Ti_5O_{12}$	Silicon (Si)	Tin (Sn)
Potential vs. Li/Li^+ (V)	0	0.05	1.55	0.4	0.6
Lithiated phase	Li	LiC_6	$Li_7Ti_5O_{12}$	$Li_{4.4}Si$	$Li_{4.4}Sn$
Volume change (%)	100	12	1	320	260
Theoretical specific capacity (mAh/g)	3862	372	175	4200	994

In carbon based anode materials, graphite is the leading anode material for most of Li-ion batteries used in current portable electronic devices, and it has a theoretical capacity of 372 mAh/g. Li-ion can reversibly intercalate (and deintercalate) into graphite to form LiC_6 according to following reaction:

$$C_6 + Li^+ + e^- \leftrightarrow LiC_6$$

The intercalation of Li-ion into graphite usually happened by following first-order phase transformations between different phases (LiC_{24}, LiC_{26} and LiC_{12}), resulting into multiple voltage plateaus in the charge-discharge curves [11].

Another category of anode materials is alloy based anodes, which usually possess a much higher capacity than graphite (Table 1.1). However, they also suffer large volume change during lithiation and delithiation. This tremendous volume change will cause cracks and pulverization of materials, and finally the active materials will lose electronic contact with current collector, resulting into severe capacity loss. One of the most representative alloy based anode materials is silicon (Si), which has a high theoretical capacity of 4200 mAh/g (Table 1.1). However, it also suffers a 300% volume change upon lithiation and a low first-cycle reversible capacity. Recently, some novel nano-structured Si anodes, such as Si nanowires [12], Si nanotubes [13], hollow Si nanosphere [14], were investigated and the electrochemical cycling stability of Si anodes had been greatly improved.

Beside carbon and alloy based anode materials, some new materials, such as TiO_2, CuO and $Li_4Ti_5O_{12}$, were also proposed as the anode materials for Li-ion batteries. However, these materials usually show a low theoretical capacity and have a high voltage vs. Li/Li^+, which will result into a high energy penalty of full cells and low energy density.

1.1.2. Cathode Materials

Based on their different crystal structures, cathode materials of Li-ion batteries mainly fall into three categories [15]: layered structure ($LiTiS_2$, $LiMO_2$, M=Co, Mn, Ni etc.), spinel $Li_{1+x}Mn_{2-x}O_4$ system ($LiMn_2O_4$, etc.) and phosphate olivine ($LiMPO_4$, M=Fe, Mn, CO, Ni, etc.). Table 1.2 shows the electrochemical properties for some major cathode materials in Li-ion batteries.

Table 1.2. Properties of some typical cathode materials for Li-ion batteries [15].

Materials / Properties	$LiCoO_2$	$LiNiO_2$	$LiMn_2O_4$	$LiFePO_4$	$LiMnPO_4$
Potential vs. Li/Li^+ (V)	3.9	3.5	4.0	3.4	4.1
Specific capacity (mAh/g)	130	180	148	170	171
Specific energy (Wh/kg)	507	630	585	578	701

One of the most representative layered structure cathode materials is $LiCoO_2$, which was first introduced and successfully commercialized by Sony in 1991. Although $LiCoO_2$ has a theoretical specific capacity of 274 mAh/g, only half of Li-ion can be reversibly extracted/inserted from $LiCoO_2$, which results into the composition $Li_{0.5}CoO_2$ and a specific capacity of 140 mAh/g [16]. Once the Li-ion was completely removed from $LiCoO_2$, the resulted material became unstable and showed very poor cycling stability [16].

The spinel cathode $LiMn_2O_4$, which has an edge-shared Mn_2O_4 octahedral framework, shows good cycling stability when lithiation/delithiation is limited to $Li_xMn_2O_4$ ($0<x<1$) [15]. Further lithiation of $LiMn_2O_4$ will result in $Li_{1+x}Mn_2O_4$ ($0<x<1$) and a voltage plateau around 3 V, which usually leads to severe structure distortion and capacity decay due to leaching of Mn ions into electrolyte. Due to this reason, the accessible capacity of $Li_xMn_2O_4$ is limited to 120~125 mAh/g with a practical operating voltage greater than 3.5 V.

Phosphate olivine $LiMPO_4$ (M=Fe, Mn, Co, etc.) has the ordered-olivine structure, in which oxygen atoms are located in a hexagonal-close-packed arrangement, phosphorus atoms are located in tetrahedral sites, and iron and lithium atoms occupy octahedral 4a and 4c sites, respectively [17]. Among all phosphate olivine cathode materials, $LiFePO_4$ has been intensively studied over the past decades [18-20], and has been considered to be a very promising candidate material for the cathode of high-power, safe, low-cost and long-life Li-ion batteries required for hybrid electric vehicles and renewable energy storage. The most striking characteristic of this material is a very flat charge/discharge profile at the voltage of ~3.4 V vs. Li/Li^+ due to a phase transformation reaction between two end members of $LiFePO_4$ and $FePO_4$. This voltage is well suitable with the window of most carbonate based electrolytes. However, pure $LiFePO_4$ suffered from poor rate capability due to its low intrinsic electronic/ionic conductivity and slow phase transformation. Since its invention by Goodenough in 1997 [18], extensive research has been carried out to overcome the poor reaction kinetics of $LiFePO_4$. The most effective strategies include (1) to downsize the $LiFePO_4$ particles to nano-scale [21] and (2) to coat electronically conductive carbon [22] or an ionically conductive phase [20] onto the $LiFePO_4$ particle surface. Other phosphate olivines, including $LiMnPO_4$ [23] and $LiCoPO_4$ [24] with relatively higher operative voltages compared with $LiFePO_4$, are also under intensively investigation.

1.2. Traditional Electrochemical Techniques and Their Analysis Methods

Depending on the ways of how to apply the electrochemical signals on the electrochemical devices, the major electrochemical techniques can be divided into four categories. The basic principles of different electrochemical techniques are briefly introduced below.

1.2.1. Galvanostatic Intermittent Titration Technique (GITT) and Potentiostatic Intermittent Titration Technique (PITT)

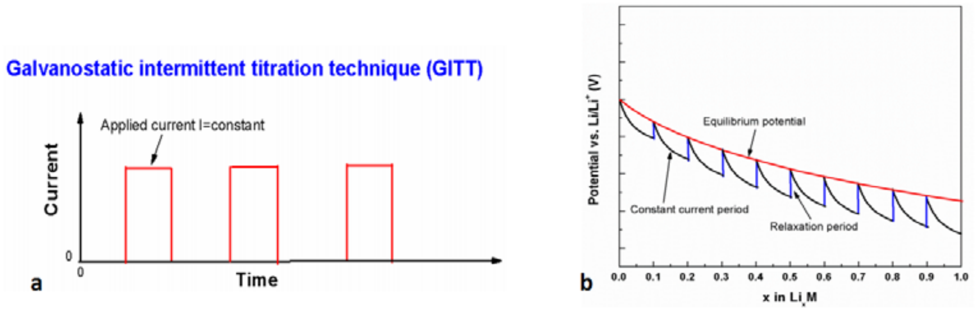

Figure 1.2. Illustration of GITT. (a) Applied signals, and (b) corresponding responses.

GITT is a standard electronanalytical technique to investigate the ion transport properties in solid solution electrode materials. Figure 1.2 is the schematic illustration of GITT, in which the electrode system is subjected to a small constant current for a time interval, and the voltage between the working electrode and reference electrode is measured as a function of time. Assuming one-dimensional diffusion in solid solution materials without consideration of Ohmic potential drop, double-layer charging, charge transfer kinetics and phase transformation, the chemical diffusion coefficient of active ions in the host materials can be calculated from the potential response by using following equation [8]

$$D_{GITT} = \frac{4}{\pi}\left(\frac{IV_M}{Z_A FS}\right)\left[\left.\frac{dE(x)}{dx}\right/\frac{dE(t)}{d\sqrt{t}}\right] \qquad (t \ll L^2/D_{GITT}) \qquad (1.1)$$

where D_{GITT} (cm^2/s) is the chemical diffusion coefficient of active ions determined from GITT, L (cm) is the characteristic length of electrode materials, F is the Faraday constant (96500 C/mol), Z_A is the charge number of electro-active species (for Li-ion battery, Z_A=1), S (cm^2) is the contact area between electrode and electrolyte, I (A) is the applied current and V_M (cm^3/mol) is the molar volume of the electrode material. x is the composition of Li-ion in host materials (Li_xM, M=host materials) and t is the transient time during the test. $E(t)$ is the transient voltage response of working electrode. $E(x)$ is the steady-state equilibrium potential of working electrode at the composition of Li_xM, which can be obtained from coulometric titration curve. The value of $\frac{dE(t)}{d\sqrt{t}}$ can be obtained from the plot of transient voltage versus square root of time during constant current pulse, and $\frac{dE(x)}{dx}$ can be measured by plotting steady-state equilibrium electrode voltage against electro-active material composition.

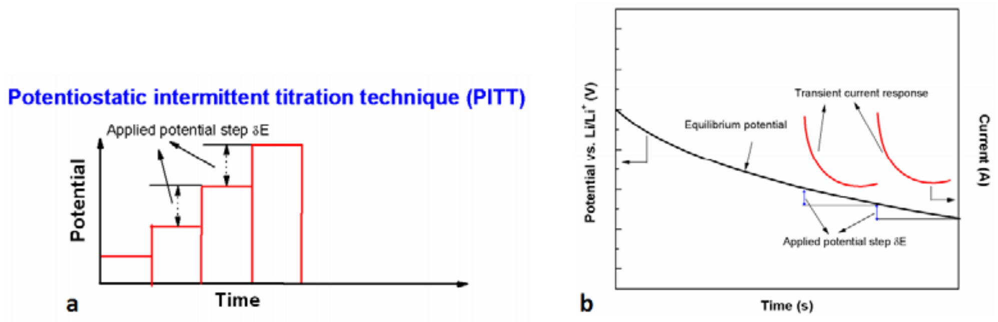

Figure 1.3. Illustration of PITT. (a) Applied signals, and (b) corresponding responses.

Instead of a current pulse as in GITT, a small voltage step is applied to the system under the PITT measurements, and the resulting current is measured as a function of time (Figure 1.3). Similar to GITT, which assumes one-dimensional diffusion in solid solution materials, the chemical diffusion coefficient of active ions in solid solution electrode materials can be estimated based on the current response during the PITT test by using following equation [8]

$$D_{PITT} = -\frac{d\ln I(t)}{dt}\frac{4L^2}{\pi^2} \qquad (t >> L^2/D_{PITT}) \qquad (1.2)$$

where D_{PITT} (cm^2/s) is the chemical diffusion coefficient of active ions measured from PITT, L (cm) is the characteristic length of electrode material and $I(t)$ is the transient current measured during the constant voltage step.

1.2.2. Cyclic Voltammetry (CV)

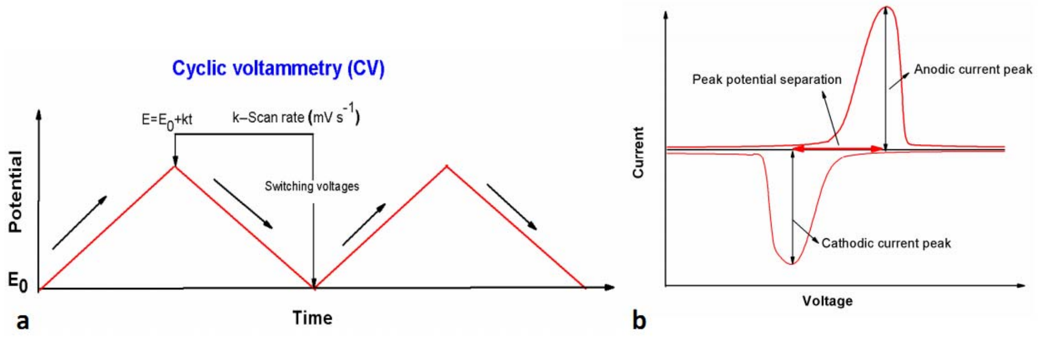

Figure 1.4. Illustration of CV. (a) Applied signals, and (b) corresponding responses.

Among the traditional electrochemical methods, CV is one of the most commonly used techniques for electrode kinetics studies. Unlike GITT and PITT methods, no thermodynamic information is needed for calculating the apparent diffusion coefficient. During CV tests, the electrode working potential is linearly cycled over some potential ranges at certain rates while the resulting current is recorded against time (potential) (Figure 1.4). By analyzing the resulting current versus potential profiles, both kinetic and thermodynamic information can be obtained. The chemical diffusion coefficient of the active ions in a solid solution electrode material can be calculated according to the linear relationship between the peak current and the square root of the scan rate (v) in Eq. (3) [9]

$$i_p = 0.4463\left(\frac{F^3}{RT}\right)^{\frac{1}{2}} n^{\frac{3}{2}} S D_{cv}^{\frac{1}{2}} C_0^* v^{\frac{1}{2}} \tag{1.3}$$

where i_p is the peak current (amperes), n is the number of electrons involved in the reaction (mol), S is the contact area between electrode and electrolyte (cm^2), D_{cv} is the chemical diffusion coefficient of active ions determined by CV (cm^2/s), C_0^* is the initial concentration of active ions (mol/m^3), v is the scan rate (V/s), and R and T have their usual meanings. Besides the diffusion coefficient, the potential difference between the cathodic and anodic peak current is normally used to evaluate the reversibility of the reaction. Also, high peak current, speculate peak shape and small peak potential separation are usually indicators for fast kinetics.

1.2.3. Electrochemical Impedance Spectroscopy (EIS)

EIS is another powerful technique to determine the chemical diffusion coefficients of active ions in the electrode materials. It perturbs the system from equilibrium using a

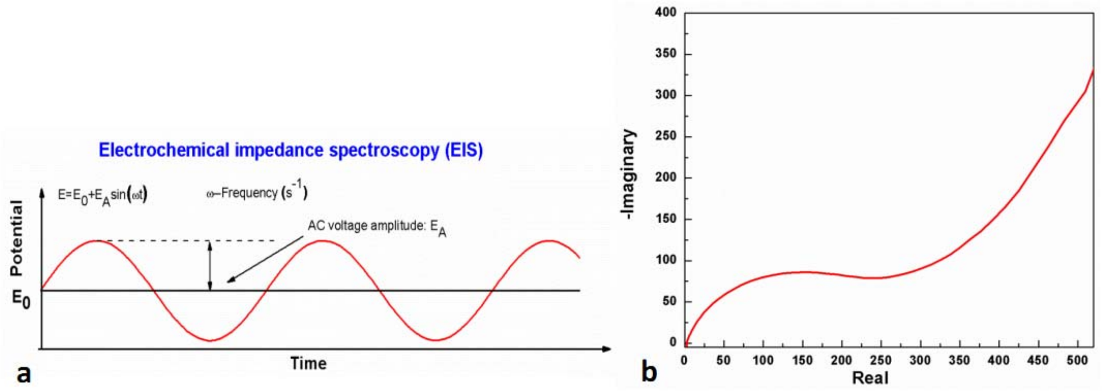

Figure 1.5. Illustration of EIS. (a) Applied signals, and (b) corresponding responses.

small AC potential (or current) at a variety of frequencies, and the resultant impedance is calculated (Figure 1.5). The chemical diffusion coefficient of active ions in a solid solution electrode can be obtained using Eq. (4) by analyzing the low frequency response with the same assumptions as the one GITT and PITT made [10]

$$D_{EIS} = \frac{1}{2}\left[\left(\frac{V_m}{FS\sigma}\right)\left(\frac{dE(x)}{dx}\right)\right]^2 \tag{1.4}$$

where D_{EIS} is the chemical diffusion coefficient of active ions obtained from EIS (cm^2/s), V_m is the molar volume of the host electrode (cm^3/mol), S (cm^2) is the surface area of the electrode, σ (Ω Hz$^{1/2}$) is the Warburg factor and $\frac{dE(x)}{dx}$ has the same meaning as it in Eq. (1).

1.2.4. Limitations of Traditional Analysis Methods for Electrochemical Techniques

Since the analysis methods for above different electrochemical techniques were derived with the assumption of active ions diffusion in single phase solid solution materials, they are only reliable in the case of a continuous concentration profile obeying Fick's second law of diffusion, and cannot be directly used in phase transformation electrode materials where the ions are transported through the movement of an inter-phase boundary. One compromise way is to obtain an 'apparent' chemical diffusion coefficient in the two-phase domain with above equations. However, the reliability of these 'apparent' diffusion coefficients is quite questionable. Markevich *et al.* [25] measured the chemical diffusion coefficients of Li-ion in graphite, which has three successive phase transformation regions during Li-ion intercalation, at different Li-ion insertion levels using the PITT and GITT methods. Their findings [25] demonstrated that the "apparent" Li-ion diffusion coefficient (10^{-13}~10^{-11} cm^2 s^{-1}) for phase 1 in the two-phase region is several orders of magnitude lower than that in the single-phase region (10^{-8} cm^2 s^{-1}) (Figure 1.6a). Obviously, these two diffusion coefficients should be equal or, at least, similar with each other, because phase 1 is under similar states whether the electrode material is in single-phase region or two-phase region. Lu *et al.* [26] measured the Li-ion diffusion coefficient for V_2O_5 thin film by PITT and EIS. They found sharp minima on the plot of diffusion coefficient versus potential in the vicinity of two-phase regions (Figure 1.6b), which are similar to the results for graphite. The chemical diffusion coefficient of Li-ion in $LiFePO_4$ was measured by Prosini *et al.* [27] with GITT and Xie *et al.* [28] with EIS, separately, and both of their results showed a minimum of Li-ion chemical diffusion coefficient at the phase transformation regions (Figure 1.6c). A reduced apparent diffusion coefficient in the two-phase region was also reported in $Li_4Ti_5O_{12}$ thin films [29]. Since the Li-ion chemical diffusion coefficient measured in the single-phase region is considered to be reliable, the significant reduction of the chemical diffusion coefficient in the two-phase regions should be attributed to the phase transformation.

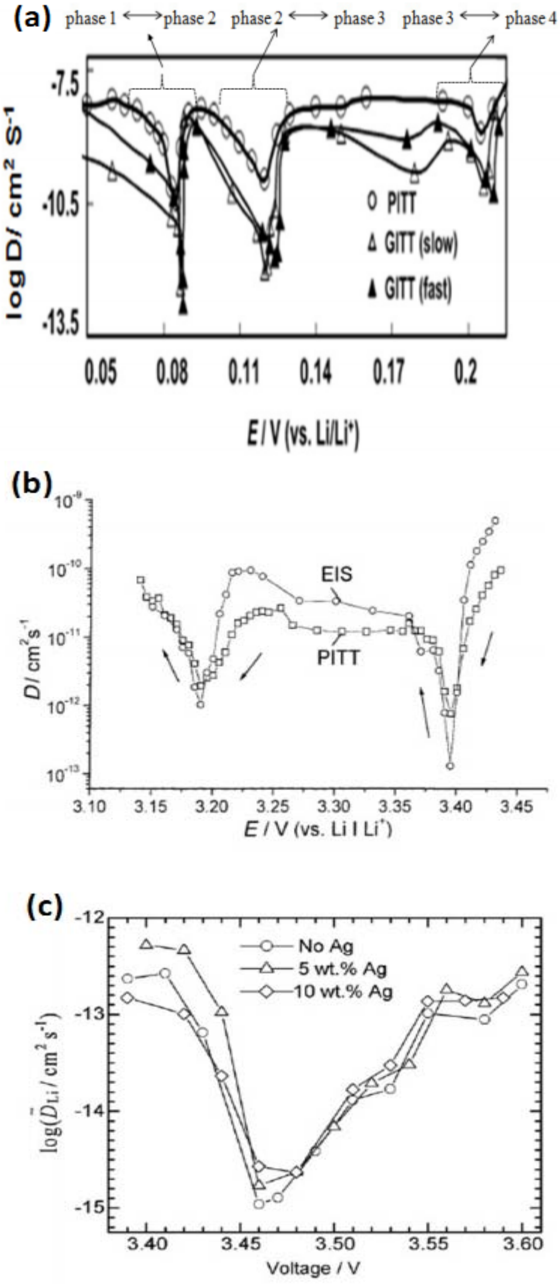

Figure 1.6. The Li-ion chemical diffusion coefficient in (a) graphite measured by GITT and PITT [25], (b) V_2O_5 measured by PITT and EIS [26], (c) $LiFePO_4$ measured by EIS [28].

Trying to address this problem, a moving boundary model was proposed to take the phase transformation into account, which assumes local equilibrium condition at the inter-phase boundary and no volume change (*no strain and stress*), i.e. diffusion is the only factor controlling the phase boundary movement during phase transformation [30]. With this model, a Li-ion chemical diffusion coefficient of 10^{-10}~10^{-11} cm^2 s^{-1} was obtained for phase 1 of graphite in the two-phase region [30-31], which is still significantly lower than that for phase 1 in the single-phase region (10^{-8} cm^2 s^{-1}). Newman *et al*. [32] proposed a three-dimensional shrinking-core model and integrated it with the porous theory to predict the discharge process of $LiFePO_4$. In their shrinking-core model, the phase transformation is assumed to be controlled by diffusion only, which means local equilibrium assumption at the phase boundary separating two phases. By fitting the experimental results with the simulated data, they obtained the Li-ion chemical diffusion coefficient in the order of 10^{-14} cm^2 s^{-1}, which was one order lower than that in single phase region. It is clear that the moving boundary (or shrinking-core in 3-D space) model, with the assumption of local equilibrium condition, considered diffusion as the only controlling factor of the phase transformation, which cannot capture the mechanism of phase transformation electrode materials.

1.3. Motivation and Objective

The traditional analysis methods for electroanalytical techniques (GITT, PITT, CV and EIS) derived from the Fickian diffusion equations are only suitable for solid solution electrode materials because the effect of inter-phase boundary movement on ion transport is not considered. Directly using these analysis methods to measure the apparent ion diffusion coefficient for phase transformation electrode materials resulted in considerable controversy [25-29]. The ion diffusion coefficient obtained from moving boundary model is also an apparent value, since phase transformation usually is not only controlled by ion diffusion, but also limited by the mobility of inter-phase boundary. The intrinsic kinetic parameters of phase transformation electrode materials, namely ion diffusion coefficient and interface mobility, cannot be obtained by any electroanalytical techniques with traditional analysis methods.

This work is motivated by the increasing demand for accurate analysis methods for electroanalytical techniques and recent advances in the theory of phase transformation achieved by us [33-34] and other investigators [35-37].

The ***first objective*** of this work is to develop a mixed-control model, which considers the effects of both ion diffusion and interface migration in the presence of lattice misfit strain between the two phases.

The ***second objective*** of this work is to integrate the mixed-control model with different electrochemical techniques (GITT, PITT, CV and EIS).

The ***third objective*** of this work is to use the mixed-control model to analyze the phase transformation electrode materials (such as $LiFePO_4$) under different electrochemical techniques.

The ***fourth objective*** of this work is to investigate the real-time lithiation/delithiation process of phase transformation electrode materials by *in situ* high resolution transmission electron microscopy (HRTEM), and to compare the experiment results with model prediction.

1.4. Dissertation Layout

To achieve the stated research objectives, the subsequent chapters of this dissertation are organized as follows.

In Chapter 2, we develop a mixed-control phase transformation model based on the discharge process of $LiFePO_4$, which is a typical phase transformation electrode material in Li-ion battery. We clarify the coupling between ion diffusion and phase boundary migration in the presence of strain accommodation energy due to misfit strain between the two phases. The chemical and mechanical contributions to the interface driving forces are determined, and the boundary conditions for the diffusion problem that is implied by interface kinetics are derived.

In Chapter 3, based on the relationships between equilibrium potentials and strain accommodation energy developed in Chapter 2, we explore the potential hysteresis and strain accommodation energy of two $LiFePO_4$ samples with different particle sizes. The characteristics inside the potential hysteresis region are studied by GITT, CV and EIS, and the results show that the $LiFePO_4$ inside potential hysteresis region behaves like a solid solution.

In Chapter 4, taking the $LiFePO_4$ system as a specific example, we determine the Li-ion diffusion coefficient and interface mobility of two $LiFePO_4$ electrodes in two-phase region by using the mixed-control model integrated GITT and PITT. For the first time, the interface mobility at different states of discharge for two $LiFePO_4$ samples is obtained.

In Chapter 5, we integrate the mixed-control model with CV. Besides ion diffusion and phase transformation, the electrolyte resistance and charge transfer effect are also considered in the mixed-control model integrated CV. The Li-ion diffusion coefficient and interface mobility of $LiFePO_4$ are obtained by fitting the measured CV data with simulation results. Moreover, the effect of phase transformation, ion diffusion coefficient, particle size, electrolyte resistance, and charge transfer resistance on the CV profiles is analyzed with the mixed-control model integrated CV.

In Chapter 6, the electrochemical lithiation of $FePO_4$ particles is investigated by *in situ* high resolution transmission electron microscopy (HRTEM), and the anisotropic lithiation mechanism is directly observed. For the first time and in contrast to the previous post mortem HRTEM observations, a sharp (010) phase boundary between $LiFePO_4$ and $FePO_4$ is observed, which migrates along the [010] direction during lithiation. Furthermore, our *in situ* HRTEM observations reveal misfit dislocation populations on the (010) phase boundary, overthrowing previous model assumption of fully coherent phase boundary. These misfit dislocations not only greatly relax the elastic energy, but also change the kinetics of nucleation and growth, as well as provide a mechanism for long-term lithium ion battery electrode fatigue and failure, due to repeated coherency loss in microparticles.

In Chapter 7, we summarize the major contributions and findings of this dissertation and some future work is proposed.

1.5. References

1. S. G. Chalk and J. F. Miller, Key challenges and recent progress in batteries, fuel cells, and hydrogen storage for clean energy systems. *J. Power Sources* **159**, 73-80 (2006).

2. J.-M. Tarascon and M. Armand, Issues and challenges facing rechargeable lithium batteries. *Nature* **414**, 359-367 (2001).
3. S. Y. Chung, J. T. Bloking, and Y. M. Chiang, Electronically conductive phospho-olivines as lithium storage electrodes. *Nat. Mater.* **1**, 123-128 (2002).
4. N. Meethong, H. -Y. S. Huang, S. A. Speakman, W. C. Carter, and Y. M. Chiang, Strain accommodation during phase transformations in olivine-based cathodes as a materials selection criterion for high-power rechargeable batteries. *Adv. Funct. Mater.* **17**, 1115-1123 (2007).
5. A. Funabiki, M. Inaba, T. Abe, and Z. Ogumi, Stage transformation of lithium-graphite intercalation compounds caused by electrochemical lithium intercalation. *J. Electrochem. Soc.* **146**, 2443-2448 (1999).
6. P. Subramanya Herle, B. Ellis, N. Coombs, and L. F. Nazar, Nano-network electronic conduction in iron and nickel olivine phosphates. *Nat. Mater.* **3,** 147-152 (2004).
7. C. Wang and J. Hong, Ionic/electronic conducting characteristics of $LiFePO_4$ cathode materials. *Electrochem. Solid-State Lett.* **10**, A65-A69 (2007).
8. C. J. Wen, B. A. Boukamp, and R. A. Huggins, Thermodynamic and mass transport properties of "LiAl". *J. Electrochem. Soc.* **12**6, 2258-2266 (1979).
9. A. J. Bard and L. R. Faulkner, *Electrochemical Methods*, John Wiley & Sons, Inc., New York, (1980).
10. C. Ho, I. D. Raistrick, and R. A. Huggins, Application of A-C techniques to the study of lithium diffusion in tungsten trioxide thin films. *J. Electrochem. Soc.* **127**, 343-350 (1980).

11. W.-J. Zhang, A review of the electrochemical performance of alloy anodes for lithium-ion batteries. *J. Power Sources* **196**, 13-24 (2011).

12. C. K. Chan, H. Peng, G. Liu, K. Mcilwrath, X. F. Zhang, R. A. Huggins, and Y. Cui, High-performance lithium battery anodes using silicon nanowires. *Nat.Nanotech.* **3**, 31-35 (2008).

13. H. Wu, G. Chan, J. W. Choi, I. Ryu, Y. Yao, M. T. McDowell, S. W. Lee, A. Jackson, Y. Yang, L. Hu, and Y. Cui, Stable cycling of double-walled silicon nanotube battery anodes through solid-electrolyte interphase control. *Nat. Nanotech.* **7**, 310-315 (2012).

14. H. Ma, F. Cheng, J. Chen, J. Zhao, C. Li, Z. Tao, and J. Liang, Nest-like Silicon Nanospheres for High-Capacity Lithium Storage. *Adv. Mater.* **19**, 4067-4069 (2007).

15. C. M. Hayner, X. Zhao, and H. H. Kung, Materials for rechargeable lithium-ion batteries. *Annu. Rev. Chem. Biomol. Eng.* **3**, 445-471 (2012).

16. M. S. Whittingham, Lithium batteries and cathode materials. *Chemical Review* **104**, 4271-4301 (2004).

17. L.-X. Yuan, Z.-H. Wang, W.-X. Zhang, X.-L. Hu, J.-T. Chen, Y.-H. Huang, and J. B. Goodenough, Development and chanlleges of $LiFePO_4$ cathode material for lithium-ion batteries. *Energy Environ. Sci.* **4**, 269-284 (2011).

18. A. K. Padhi, K. S. Nanjundaswamy, and J. B. Goodenough, Phospho-olivines as positive-electrode materials for rechargeable lithium batteries. *J. Electrochem. Soc.* **144**, 1188-1194 (1997).

19. X. L. Wu, L. Y. Jiang, F. F. Cao, Y. G. Guo, and L. J. Wan, $LiFePO_4$ nanoparticles embedded in a nanoporous carbon matrix: superior cathode material for electrochemical energy-storage devices. *Adv. Mater.* **21**, 2710-2714 (2009).

20. B. Kang and G. Ceder, Battery materials for ultrafast charging and discharging. *Nature* **458**, 190-193 (2009).

21. N. Meethong, H-Y. S. Huang, S. A. Speekman, W. C. Carter, and Y-M. Chiang, Size-dependent lithium miscibility gap in nanoscale $Li_{1-x}FePO_4$. *Electrochem. Solid-State Lett.* **10**, A134-A138 (2007).

22. M. M. Doeff, Y. Hu, F. Mclarnon, and R. Kostecki, Effect of surface carbon structure on the electrochemical performance of $LiFePO_4$. *Electrochem. Solid-State Lett.* **6**, A207-A209 (2003).

23. S. K. Martha, B. Markovsky, J. Grinblat, Y. Gofer, O. Haik, E. Zinigrad, D. Aurbach, T. Drezen, D. Wang, G. Deghenghi, and I. Exnar, $LiMnPO_4$ as an advanced cathode material for rechargeable lithium batteries. *J. Electrochem. Soc.* **156**, A541-A552 (2009).

24. N. N. Bramnik, K. G. Bramnik, T. Buhrmester, C. Baehtz, H. Ehrenberg, and H. Fuess, Electrochemical and structural study of $LiCoPO_4$-based electrodes. *J. Solid State Electrochem.* **8**, 558-564 (2004).

25. E. Markevich, M. D. Levi, and D. Aurbach, Comparison between potentiostatic and galvanostatic intermittent titration techniques for determination of chemical diffusion coefficients in ion-insertion electrodes. *J. Electroanal. Chem.* **580**, 231-237 (2005).

26. Z. Lu, M. D. Levi, G. Salitra, Y. Gofer, E. Levi, and D. Aurbach, Basic electroanalytical characterization of lithium insertion into thin, well-crystallized V_2O_5 films. *J. Electroanal. Chem.* **491**, 211-221 (2000).

27. P. P. Prosini, M. Lisi, D. Zane, M. Pasquali, Determination of the chemical diffusion coefficient of lithium in $LiFePO_4$. *Solid State Ionic*s **148**, 45-51 (2002).

28. J. Xie, N. Imanishi, T. Zhang, A. Hirano, Y. Takeda, and O. Yamamoto, Li-ion diffusion kinetics in $LiFePO_4$ thin film prepared by radio frequency magnetron sputtering. *Electrochim. Acta* **54**, 4631-4637 (2009).

29. Y. H. Rho and K. Kanamura, Li^+ ion diffusion in $Li_4Ti_5O_{12}$ thin film electrode prepared by PVP sol-gel method. *J. Solid State Chem.* **177**, 2094-2100 (2004).

30. M. D. Levi, E. Markevich, D. Aurbach, Comparison between Cottrell diffusion and moving boundary models for determination of the chemical diffusion coefficients in ion-insertion electrodes. *Eelectrochim. Acta* **51**, 98-110 (2005).

31. M. D. Levi, E. Markevich, C. Wang, and D. Aurbach, Chronoamperometric measurements and modeling of nucleation and growth, and moving boundary stages during electrochemical lithiation of graphite electrode. *J. Electroanal. Chem.* **600**, 13-22 (2007).

32. V. Srinivasan and J. Newman, Discharge model for the lithium iron-phosphate electrode. *J. Electrochem. Soc.* **151**, A1517-A1529 (2004).

33. C. Wang, U. Kasavajjula, and P. E. Arce, A discharge model for phase transformation electrode: formulation, experimental validation, and analysis. *J. Phys. Chem. C* **111**, 16656-16663 (2007).

34. U. Kasavajjula, C. Wang and P. E. Arce, Discharge model for $LiFePO_4$ accounting for the solid solution range. *J. Electrochem. Soc.* **155**, A866-A874 (2008).

35. G. P. Krielaart, J. Sietsma, and S. V. D. Zwaag, Ferrite formation in Fe-C alloys during austenite decomposition under non-equilibrium interface conditions. *Mater. Sci. Eng.* **A237**, 216-223 (1997).

36. C. Bos, and J. Sietsma, A mixed-mode model for partitioning phase transformations. *Scr. Mater.* **57**, 1085-1088 (2007).

37. J. Sietsma, M. G. Mecozzi, S. M. C. Van Bohemen, and S. V. Zwaag, Evolution of the mixed-mode character of solid-state phase transformations in metals involving solute partitioning. *Int. J. Mater. Res.* 97, 356-361 (2006).

Chapter 2: Development of the Mixed-Control Phase Transformation Model

2.1. General Discharge and Charge Processes of Phase Transformation Electrode Materials

Different electrode materials have various characteristics during discharge and charge processes, but in general, the discharge and charge processes of phase transformation electrode materials in Li-ion batteries include Li-ion insertion and extraction, and the nucleation and growth of a new phase in the parent phase. Below we take $LiFePO_4$ as an example to describe the discharge (lithiation) process in phase transformation electrode materials.

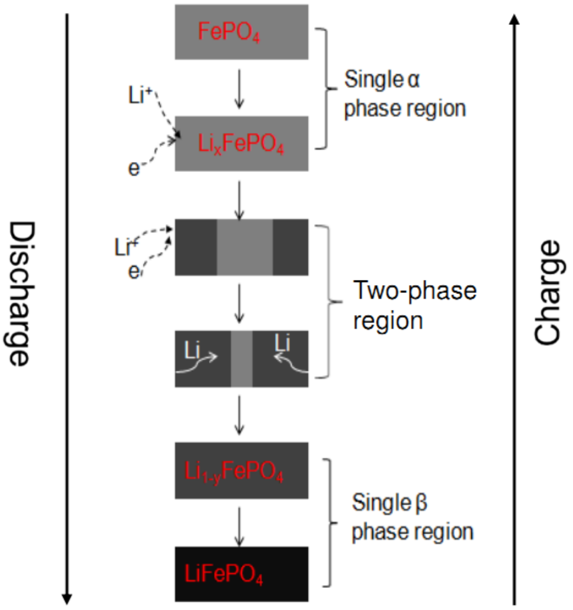

Figure 2.1. Schematic discharge/ charge processes of $LiFePO_4$.

At the beginning of Li-ion insertion (discharge), lithium ions insert into the particle surface layer and diffuse into the interior of the electrode particle to form a solid solution phase α (Li_xFePO_4, x is the Li-ion excess in the Li-ion deficient phase, Figure 2.1). During the Li-ion insertion, stress and strain are generated and stored in the α phase, resulting in the steady-state equilibrium lithiation potential drops below the theoretical (*unstrained*) equilibrium potential, e.g. the experimental discharge equilibrium potential E_{de} follows the line A-B in Figure. 2.2 instead of the theoretical line A-F (Figure 2.2). When the Li-ion insertion level reaches the solid solubility limit in the α phase (point B in Figure 2.2), phase transformation happens and a Li-

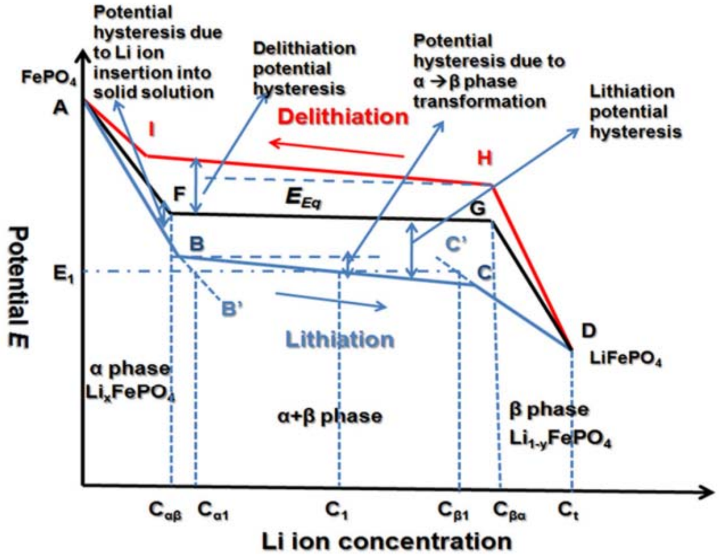

Solid black line (A-F-G-D) is the theoretical (strain-free) equilibrium potential-Li ion composition isotherm

Solid blue line (A-B-C-D) is the discharge equilibrium potential-Li ion composition isotherm after consideration of Li ion insertion strain

Solid red line (A-I-H-D) is the charge equilibrium potential-Li ion composition isotherm after consideration of Li ion extraction strain

$C_{\alpha\beta}$ --- Theoretical (strain-free) Li ion concentration in α phase equilibrium with β phase

$C_{\beta\alpha}$ --- Theoretical (strain-free) Li ion concentration in β phase equilibrium with α phase

$C_{\alpha1}$ --- Li ion concentration in α phase corresponding to equilibrium potential E_1

$C_{\beta1}$ --- Li ion concentration in β phase corresponding to equilibrium potential E_1

C_t --- Maximum Li ion concentration that can be incorporated in $FePO_4$

Figure 2.2. Schematic illustration of equilibrium potential changes during the discharge/charge processes in $LiFePO_4$.

ion rich phase, β phase ($Li_{1-y}FePO_4$, y is the Li-ion deficiency in the Li-ion rich phase, Figure 2.1), will be formed in the α phase matrix.

According to Gibbs phase rule, at two-phase regions under equilibrium condition, the degree of freedom is $f=c-p+2$ (f-degree of freedom, c-number of components, p-number of coexisting phases). At two-phase regions, given constant temperature and pressure, the degree of freedom is zero, so the theoretical equilibrium potential should remain constant with the change of Li-ion composition x during phase transformation, which will give a voltage plateau on the discharge curve (line F-G in Figure 2.2). However, due to the lattice misfit between α and β phase, the growth of the β phase inside the α phase during Li-ion insertion results in the accumulation of strain/stress, and this gradually decreases the measured discharge equilibrium potential E_{de}, which will follow B-C line instead of the theoretical F-G line in Figure 2.2. Once the α phase completely transforms into the β phase, subsequent lithium ions will start to dissolve into the β phase and form a solid solution with its maximum concentration C_t which is corresponding to $LiFePO_4$ (Figure 2.1), and the equilibrium potential for this region will follow C-D line in Figure 2.2.

When the measured discharge equilibrium potential follows B-C line, the equilibrium concentration of Li-ion in α phase varies along the extension of A-B line (B-B$^{'}$) and the equilibrium concentration of Li-ion in the β phase follows the extension of D-C line (C-C$^{'}$). For example, when the Li-ion insertion level reaches C_1, the electrode has an equilibrium potential of E_1 (Figure 2.2) and is a mixture of α phase with composition $C_{\alpha 1}$ and β phase with composition $C_{\beta 1}$. During lithiation, the measured discharge equilibrium potential changes with overall Li-ion composition (*capacity*) following the line A-B-C-D in Figure 2.2. Similarly, a reverse phase transformation occurs during Li-ion extraction but at a higher potential than that of Li-ion insertion, following the line of D-H-I-A in Figure 2.2. So, the measured equilibrium potentials show a significant potential hysteresis between charge and discharge, which is induced by the dissipation of energy to the surroundings due to elastic-plastic accommodation of strain resulting from the volume difference between the coexisting two phases [1-3].

2.2. Development of the Mixed-Control Model for Phase Transformation Electrode Materials

We take the discharge process of $LiFePO_4$ ($\alpha \rightarrow \beta$ phase transformation) as an example to develop the mixed-control phase transformation model. If we disregard the nucleation process of β phase in α phase, the α to β phase transformation mainly involves two processes. First, the β phase layer grows and phase boundary migrates occur simultaneously, which results in a gradual rearrangement of the lattice of parent phase α into the lattice of product phase β. Second, Li-ion diffusion occurs from the particle surface into the inter-phase boundary through the β phase layer.

The free energy change $\Delta G_{\alpha \rightarrow \beta}$ on α phase to β phase transformation can be expressed as Eq. (2.1) [3, 4]

$$\Delta G_{\alpha \rightarrow \beta} = \Delta G_{\alpha \rightarrow \beta}^{chem} + \Delta G_{\alpha \rightarrow \beta}^{accom} + \Delta G_{\alpha \rightarrow \beta}^{surface} \tag{2.1}$$

where $\Delta G_{\alpha \rightarrow \beta}^{chem}$ is the chemical free energy change on phase transformation from unstrained α phase to unstrained β phase, $\Delta G_{\alpha \rightarrow \beta}^{accom}$ is the free energy change accompanied with the elastic and/or plastic deformation due to the different lattice parameters between α and β phase, which is usually called accommodation energy [3], $\Delta G_{\alpha\to\beta}^{surface}$ is the surface free energy change associated with the transformation. Compared to the chemical free energy $\Delta G_{\alpha\to\beta}^{chem}$ and accommodation energy $\Delta G_{\alpha\to\beta}^{accom}$, $\Delta G_{\alpha\to\beta}^{surface}$ is small and will be neglected in this study.

2.2.1. Chemical Free Energy Change $\Delta G_{\alpha\to\beta}^{chem}$ on α to β Phase Transformation

For α to β phase transformation, the following reaction takes place at the phase boundary separating α phase and β phase

$$Li_xFePO_4(\alpha\text{ phase}) + (1-y-x)Li \xrightarrow{lithiation} Li_{1-y}FePO_4(\beta\text{ phase})$$

During discharge (lithiation) process, the chemical driving force $\Delta G_{\alpha\to\beta}^{chem}$ *associated with the production of one mole of new phase* can be derived from the difference between the chemical potentials related to the corresponding host material and Li-ion using Eq. (2.2) [5]

$$\Delta G_{\alpha\to\beta}^{chem} = x\left(u_{Li}^{\beta} - u_{Li}^{\alpha}\right) + \left(u_{FePO_4}^{\beta} - u_{FePO_4}^{\alpha}\right) \qquad (2.2)$$

where u_{Li}^{β} and u_{Li}^{α} are the chemical potentials of Li-ion in β and α phases, respectively, $u_{FePO_4}^{\beta}$ and $u_{FePO_4}^{\alpha}$ are the chemical potentials of $FePO_4$ in β and α phases, respectively. The chemical potentials in Eq. (2.2) disregard any mechanical force. The first term in Eq. (2.2) is the Gibbs free energy available for the trans-interface diffusion. The second term in Eq. (2.2) is the energy available for the change in lattice and the subsequent migration of the phase boundary [5]. Since the mobility of the Li-ion usually is much higher than that of the host material and the phase boundary is negligibly thin and sharp compared to the size of samples, the chemical potential of the Li-ion across the sharp interface would be continuous, which would give

$$u_{Li}^{\beta} = u_{Li}^{\alpha} \quad \text{(at the phase boundary)} \tag{2.3}$$

The continuity of carbon chemical potential across the phase boundary between α-ferrite (or martensite) and γ-austenite has been well-recognized in Fe-C alloys [5-8]. The diffusion of interstitially dissolved carbon atoms across the phase boundary between α-ferrite and γ-austenite in Fe-C alloys is similar to the diffusion of Li-ion across the phase boundary between the α and β phases in $LiFePO_4$.

So, the chemical driving force for phase transformation in Eq. (2.2) is reduced to

$$\Delta G_{\alpha \to \beta}^{chem} = u_{FePO_4}^{\beta} - u_{FePO_4}^{\alpha} \tag{2.4}$$

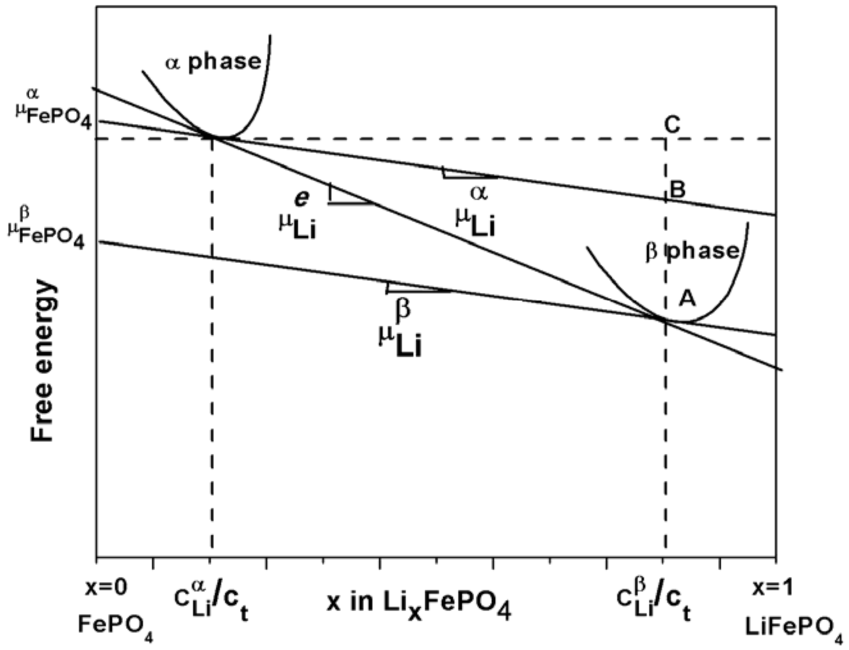

Figure 2.3. Molar free energy versus Li-ion concentration for unstrained α and β phase.

Due to the strong phase separation behavior of Li_xFePO_4 system, the molar free energy for unstrained Li_xFePO_4 system is usually assumed to follow the regular solution model with a positive heat of solution [9-11], which is depicted in Figure 2.3. As shown in Figure 2.3, the slope of the tangent of free energy with respect to Li-ion concentration x, where x is the fraction of occupied Li-ion interstitial sites, is the Li-ion chemical potential, and the intercept of the tangent with vertical axis at x=0 is the chemical potential of host material $FePO_4$ [12]. If there is no strain/stress, the equilibrium composition of Li-ion in α and β phase can be determined by the common tangent of two free energy curves [12-13]. The theoretical equilibrium potential during the phase transformation can be expressed as the difference of the Li-ion chemical potential between cathode and anode [12-13]

$$E_e = -\frac{(u_{Li}^{e} - u_{Li}^{anode})}{z_{Li}F} \tag{2.5}$$

where u_{Li}^{e} is the Li-ion chemical potential in unstrained cathode material $LiFePO_4$ during phase transformation, which is the slope of the common tangent of two free energy curves (Figure 2.2), u_{Li}^{anode} is the Li-ion chemical potential in anode (which usually is lithium metal, so u_{Li}^{anode} can be taken to be constant), Z_{Li} is the number of charge of Li-ion which is equal to 1, and F is the Faraday constant. Since u_{Li}^{e} is constant for unstrained cathode materials during phase transformation, the theoretical equilibrium potential for unstrained $LiFePO_4$ should be constant during phase transformation (F-G line in Figure 2.2).

Since we assume that the phase transformation is controlled by both Li-ion diffusion and phase boundary mobility, unlike the local equilibrium condition assumed in moving boundary model, the Li-ion concentration at the phase boundary between α and β phase will deviate from its equilibrium values. Also, with the assumption that Li-ion chemical potential is continuous at the phase boundary during any moment of dynamic discharge process, the slopes of the tangent of free energy curves with respect to Li-ion concentrations will be equal between α phase and β phase at the phase boundary, which is shown as $u_{Li}^{\beta} = u_{Li}^{\alpha}$ in Figure 2.3. So, the chemical potential difference of FePO$_4$ between α phase and β phase at the phase boundary is actually the length of A-B line in Figure 2.3. If the deviation between interface Li-ion concentration and its unstrained equilibrium value is small, according to geometry relationship, the length of A-B line can be obtained as

$$u_{FePO_4}^{\beta} - u_{FePO_4}^{\alpha} = -|AB| = -\left(\frac{C_{Li}^{\beta} - C_{Li}^{\alpha}}{C_t}\right)\left(u_{Li}^{\beta} - u_{Li}^{e}\right) \tag{2.6}$$

where $\left(\frac{C_{Li}^{\beta} - C_{Li}^{\alpha}}{C_t}\right)$ is the number of Li-ion needed to convert one mole of α phase to one mole of β phase at the phase boundary.

According to Eq. (2.5), above equation can be expressed as

$$u_{FePO_4}^{\beta} - u_{FePO_4}^{\alpha} = -\left(\frac{C_{Li}^{\beta} - C_{Li}^{\alpha}}{C_t}\right)\left(u_{Li}^{\beta} - u_{Li}^{e}\right) = -\left(\frac{C_{Li}^{\beta} - C_{Li}^{\alpha}}{C_t}\right) F \frac{\left(-\left(u_{Li}^{e} - u_{Li}^{anode}\right) - \left(-u_{Li}^{\beta} + u_{Li}^{anode}\right)\right)}{F}$$

$$= -\left(\frac{C_{Li}^{\beta} - C_{Li}^{\alpha}}{C_t}\right) F\left(E_e - E_i\right) \tag{2.7}$$

where E_i is the potential corresponding to interface Li-ion chemical potential u_{Li}^{β} or u_{Li}^{α}.

So, the chemical free energy change during phase transformation from α phase to β phase can be expressed as

$$\Delta G_{\alpha\to\beta}^{chem} = u_{FePO_4}^{\beta} - u_{FePO_4}^{\alpha} = -\left(\frac{C_{Li}^{\beta} - C_{Li}^{\alpha}}{C_t}\right) F\left(E_e - E_i\right) \tag{2.8}$$

2.2.2. Strain Accommodation Energy $\Delta G_{\alpha\to\beta}^{accom}$ during α to β Phase Transformation

Considering reversible isothermal change for the system's energy, the two-phase equilibrium happens when [13]

$$Z_{Li} F E_{de} = -\left[\left(u_{Li}^{e} - u_{Li}^{anode}\right) + \frac{V_M^I}{\Delta n_{\alpha\to\beta}} \frac{du_{accomm}}{dV_f}\right] \tag{2.9}$$

where V_M^I is the molar volume of parent phase, $\Delta n_{\alpha\to\beta}$ is the number of lithium atoms to convert parent phase to new phase, V_f is the volume fraction of new phase in the electrode material, and u_{accomm} is the strain accommodation energy per volume of the electrode material.

Eq. (2.9) can be converted into

$$Z_{Li} F E_{de} = -\left[\left(u_{Li}^{e} - u_{Li}^{anode}\right) + \frac{V_M^I}{\Delta n_{\alpha\to\beta}} \frac{\frac{dU_{accomm}}{dN_{II}} V_T - \left(V_M^{II} - V_M^I\right) U_{accomm}}{N_T V_M^I V_M^{II}}\right] \tag{2.10}$$

where V_M^{II} is the molar volume of new phase ($m^3\ mol^{-1}$), N_{II} is the amount of new phase (mol), U_{accomm} is the total accommodation energy ($J\ mol^{-1}$), V_T is the total volume of the electrode material (m^3), N_T is the total amount of electrode material (mol).

For the electrode materials with small volume change during lithiation and delithiation processes, such as $Li_4Ti_5O_{12}$ ($\frac{\Delta V}{V}$~0%) and $LiFePO_4$ ($\frac{\Delta V}{V}$~6.8%) etc., the molar volumes of parent phase and new phase can be approximately assumed to be equal with each other, so

$$V_M^I \approx V_M^{II} \tag{2.11}$$

Eq. (2.10) can be simplified into

$$Z_{Li}FE_{de} = -\left[\left(u_{Li}^e - u_{Li}^{anode}\right) + \frac{1}{\Delta n_{\alpha\to\beta}} \frac{dU_{accomm}}{dN_{II}}\right] \tag{2.12}$$

which can be rearranged into

$$\frac{dU_{accomm}}{dN_{II}} = \Delta n_{\alpha\to\beta}\left[-\left(u_{Li}^e - u_{Li}^{anode}\right) - Z_{Li}FE_{de}\right] \tag{2.13}$$

$\frac{dU_{accomm}}{dN_{II}}$ in Eq. (2.13) is the *accommodation energy associated with the production of one mole of new phase*, which is $\Delta G_{\alpha\to\beta}^{accomm}$ in Eq. (2.1).

Plugging in Eq. (2.5) into Eq. (2.13), we can get that

$$\frac{dU_{accomm}}{dN_{II}} = \Delta n_{\alpha\to\beta} F \Delta E \tag{2.14}$$

where ΔE is the potential difference between the measured equilibrium potential and the theoretical unstrained potential.

Combining Eq. (2.8) and (2.14), we can get that the free energy change during α to β phase transformation can be expressed as

$$\Delta G_{\alpha\to\beta} = \Delta G^{chem}_{\alpha\to\beta} + \Delta G^{accom}_{\alpha\to\beta} = -\left(\frac{C^{\beta}_{Li} - C^{\alpha}_{Li}}{C_t}\right) F\left(E_e - E_i\right) + \Delta n_{\alpha\to\beta} F \Delta E \qquad (2.15)$$

2.2.3. Kinetics of Mixed-Control Model during Phase Transformation

Here, we take the lithiation process in $LiFePO_4$ under constant current (condition under GITT test) as an example to develop the mixed-control model. Before and after the phase transformation, $LiFePO_4$ is a solid solution material, and the movement of Li-ion inside the material can be described with Fick's second law of diffusion with the corresponding boundary conditions. When phase transformation happens, the movement of Li-ion in the two-phase region also follows Fick's diffusion law with a sharp phase boundary separating the two phases (Figure 2.4).

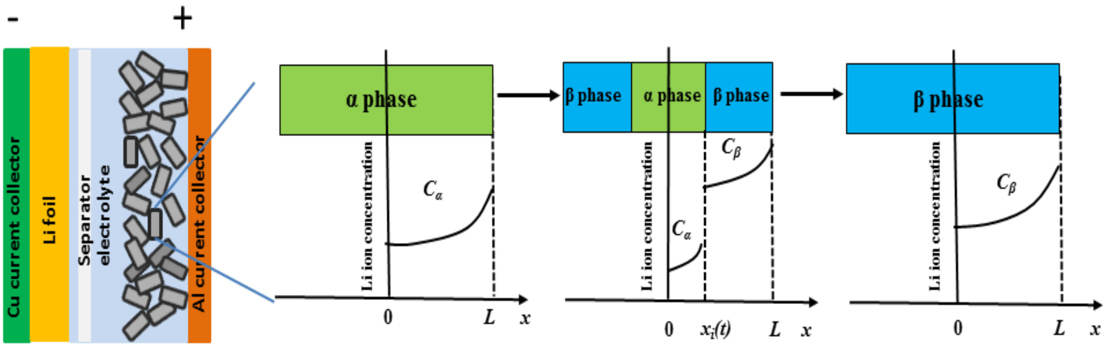

Figure 2.4. Schematic Li-ion concentration distribution during discharge process of $LiFePO_4$ starting from fully charged state (single α phase region).

Under the mixed-control phase transformation model, the corresponding initial and boundary conditions for one-dimensional discharge (lithiation) process (assuming slab geometry) are listed below. If we start from fully charged state (α phase, $FePO_4$) (Figure 2.4) and assume concentration independent chemical diffusion coefficient (*the solid solution region outside the miscibility gap is narrow~*$Li_{0.05}FePO_4$) and neglect the charge transfer effect occurring at the interface between electrode and electrolyte, the control equations for discharge process can be described as

For single α phase region

$$\frac{\partial C_\alpha}{\partial t} = D_\alpha \left(\frac{\partial^2 C_\alpha}{\partial x^2} \right) \tag{2.16}$$

$$t=0 \quad 0 \le x \le L\,,\; C_\alpha = C_\alpha^0 \tag{2.17}$$

$$t>0 \quad x=L, \qquad -\frac{D_\alpha \left(\frac{\partial C_\alpha}{\partial x} \right) F}{\rho L} = I \tag{2.18}$$

$$x=0, \qquad D_\alpha \left(\frac{\partial C_\alpha}{\partial x} \right) = 0 \tag{2.19}$$

where C_α is the Li-ion concentration in α phase (mol/cm^3), D_α is the chemical diffusion coefficient of Li-ion in α phase (cm^2/s), L is the characteristic length of LiFePO$_4$ slab (cm) (Figure 2.4), and C_α^0 is the initial concentration of Li-ion in α phase (mol/cm^3), ρ is the density of electrode material (g/cm^3), and I is the applied constant current (A/g^1). Eq. (2.19) is due to the symmetric condition at the center of the slab.

When the Li-ion concentration at the particle surface exceeds the solid solubility in α phase, phase transformation occurs. If we disregard the nucleation process and only consider the growth process of new phase, according to the mixed-control phase transformation model [5, 14], the control equations for the two-phase region are

For the β phase

$$\frac{\partial C_\beta}{\partial t} = D_\beta \left(\frac{\partial^2 C_\beta}{\partial x^2} \right) \tag{2.20}$$

$t=0 \quad x_i(t) \le x \le L,\ C_\beta = C_{\beta i}$ (2.21)

$$t>0 \quad x=L, \quad -\frac{D_\beta\left(\dfrac{\partial C_\beta}{\partial x}\right)F}{\rho L} = I \tag{2.22}$$

For the α phase

$$\frac{\partial C_\alpha}{\partial t} = D_\alpha\left(\frac{\partial^2 C_\alpha}{\partial x^2}\right) \tag{2.23}$$

$t=0 \quad 0 \le x \le x_i(t),\ C_\alpha = C_{\alpha i}$ (2.24)

$$t>0 \quad x=0, \quad D_\alpha \frac{\partial C_\alpha}{\partial x} = 0 \tag{2.25}$$

where C_β is the Li-ion concentration in the β phase (mol/cm^3), D_β is the chemical diffusion coefficient of Li-ion in the β phase (cm^2/s), $x_i(t)$ is the position of phase boundary which separates the α and β phase (cm), $C_{\alpha i}$ is the initial Li-ion concentration profile in the α phase (mol/cm^3), which is the concentration at the end of single α phase region, $C_{\beta i}$ is the initial Li-ion concentration profile in the β phase (mol/cm^3), which can be calculated according to the Li-ion concentration relationship between two phases, and all other symbols have the same meanings as above.

Since we assume a continuous Li-ion chemical potential across the α/β phase boundary, it suggests that there exists a relationship of Li-ion concentration between two phases at the phase boundary. By extrapolating the steady-state equilibrium potential versus composition lines in the single α and β regions, the relationship between discharge potential and Li-ion concentration in the α phase and β phase can be approximately expressed as a linear relationship (Figure 2.2).

$$E_\alpha(C_\alpha) = k_1 C_\alpha + b_1 \text{ (for α phase)} \tag{2.26}$$

$$E_\beta(C_\beta) = k_2 C_\beta + b_2 \text{ (for β phase)} \tag{2.27}$$

where k_1 and k_2 are the slopes of equilibrium potential versus Li-ion concentration for single α and β phases, and b_1 and b_2 are the intercepts.

So, according to mass balance and mixed-control theory, at the phase boundary separating α and β phase, the boundary conditions can be written as

at the phase boundary $x=x_i(t)$,

$$\frac{dx_i(t)}{dt} = \frac{D_\alpha\left(\frac{\partial C_\alpha}{\partial x}\right) - D_\beta\left(\frac{\partial C_\beta}{\partial x}\right)}{(C_\beta - C_\alpha)} \tag{2.28}$$

$$\frac{dx_i(t)}{dt} = M\Delta G_{\alpha\to\beta} = M(\Delta G_{\alpha\to\beta}^{chem} + \Delta G_{\alpha\to\beta}^{accom}) \tag{2.29}$$

$$E_\alpha(C_\alpha) = E_\beta(C_\beta) \tag{2.30}$$

where M (m mol J^{-1} s^{-1}) is the interface mobility and depends on the degree of interface coherence, the buildup of stress, and the deformation in the electrode material. Under the expression of Eq. (2.29), the interface mobility M of the phase boundary is actually the velocity of the phase boundary under unit driving force [5, 14]; and $\Delta G_{\alpha\to\beta}$ is the total driving force for the phase transformation (J/mol), which can be obtained from Eq. (2.15). Eq. (2.30) comes from the assumption that during the charge/discharge process, the chemical potential of Li-ion is continuous across the phase boundary, where $E_\alpha(C_\alpha)$ and $E_\beta(C_\beta)$ are the expressions between equilibrium potential and Li-ion concentration for the α and β phase, respectively. It can be shown that when $b_1=b_2$, Eq. (2.30) reduced to the boundary condition in Ref. [15].

Since we assumed that the accommodation energy only depends on the relative phase amount, Eq. (2.29) can be rewritten as at $x=x_i(t)$

$$\frac{dx_i(t)}{dt} = M(\Delta G_{\alpha\rightarrow\beta}^{chem} + \Delta G_{\alpha\rightarrow\beta}^{accom}) = M[(\frac{C_\beta - C_\alpha}{C_{\max}})F(E_i - E_e) + f(x_i(t))] \tag{2.31}$$

where $f(x_i(t))$ is the relationship between accommodation energy $\Delta G_{\alpha\rightarrow\beta}^{accom}$ and the phase fraction.

When the phase boundary reaches the center of the particles, phase transformation is considered to be finished. The electrode material becomes a solid solution again (single β phase in Figure 2.4). The main equations for this region are

single β phase region

$$\frac{\partial C_\beta}{\partial t} = D_\beta\left(\frac{\partial^2 C_\beta}{\partial x^2}\right) \tag{2.32}$$

$$t=0 \quad 0 \le x \le L \quad C_\beta=C_{\beta f} \tag{2.33}$$

$$t \ge 0 \quad x=0 \qquad \frac{\partial C_\beta}{\partial x} = 0 \tag{2.34}$$

$$x=L, \qquad -\frac{D_\beta\left(\frac{\partial C_\beta}{\partial x}\right)F}{\rho L} = I \tag{2.35}$$

where $C_{\beta f}$ is the initial Li-ion concentration profile for the single β phase region, which is the same as the Li-ion concentration profile at the end of the phase transformation region.

Overall, Eqs. (2.16)-(2.25) and Eqs. (2.28)-(2.35) describe the discharge process under constant current (condition for GITT test), which starts from the fully charged state (α phase region in Figure 2.4), goes through the phase transformation region (two-phase region in Figure 2.4), and finally ends at the fully discharged state (β phase region in Figure 2.4). By changing the boundary conditions, above equations can be modified to describe the discharge process under other electrochemical techniques, such as PITT, CV and EIS. The above equations are also suitable for the charge process. Unlike the discharge process, for the charge process, β phase is inside and α phase is outside.

2.2.4. Solution Procedures

For single-phase regions, above differential equations with corresponding initial and boundary conditions have the corresponding analytical solution or can be easily solved numerically [16]. For phase transformation region, above equations form a moving boundary problem, also known as Stefan problem [17]. Since the boundary conditions for above partial differential equations are complicated, it is impossible to obtain analytical solutions for above problem. Below we used Landau transformation to solve the Stefan problem numerically [17].

The Landau transformation introduced two new positional variables. For α phase from *x=0* to *x=x_i(t)* (Figure 2.4), $u = \frac{x}{x_i(t)}$ was introduced to fix α phase to the domain $0 \le u \le 1$. We write $C_\alpha^{'} = C_\alpha^{'}(u,t) = C_\alpha(x,t)$ to denote the concentration in terms of new positional variable, and then the governing equations (2.23) and (2.25) for α phase at the phase transformation region can be written as

$$\frac{\partial C_\alpha^{'}}{\partial t} = D_\alpha \frac{\partial^2 C_\alpha^{'}}{\partial u^2} \frac{1}{x_i(t)^2} + \frac{\partial C_\alpha^{'}}{\partial u} \frac{u}{x_i(t)} \frac{dx_i(t)}{dt} \tag{2.36}$$

$$D_\alpha \left. \frac{\partial C_\alpha^{'}}{\partial u} \right|_{u=0} = 0 \tag{2.37}$$

For β phase from $x=x_i(t)$ to $x=L$, if we define $v=\frac{x-x_i(t)}{L-x_i(t)}$, the β phase domain can be described as fixed domain $0\le v\le 1$. We write $C_\beta^{'}=C_\beta^{'}(v,t)=C_\beta(x,t)$ to denote the concentration in terms of new positional variable in β phase, and then the governing equations (2.20) and (2.22) for β phase at the phase transformation region can be written as

$$\frac{\partial C_\beta^{'}}{\partial t}=D_\beta\frac{\partial^2 C_\beta^{'}}{\partial v^2}\frac{1}{[L-x_i(t)]^2}+\frac{1-v}{L-x_i(t)}\frac{\partial C_\beta^{'}}{\partial t}\frac{dx_i(t)}{dt} \tag{2.38}$$

$$-D_\beta\left.\frac{\partial C_\beta^{'}}{\partial v}\right|_{v=1}=\frac{I\rho L}{F}(L-x_i(t)) \tag{2.39}$$

At the phase boundary, the governing equation (2.28) can be transformed to

$$\frac{D_\alpha}{x_i(t)}\frac{\partial C_\alpha^{'}}{\partial u}-\frac{D_\beta}{L-x_i(t)}\frac{\partial C_\beta^{'}}{\partial v}=(C_\beta^{'}-C_\alpha^{'})\frac{dx_i(t)}{dt} \tag{2.40}$$

The Landau transformation has simplified the problem in that all of the boundaries are now fixed, so any numerical methods developed to solve systems of partial differential equations with fixed boundaries can be used to solve this problem. Here, the above equations are converted to dimensionless form and solved with the numerical method of lines (MOL) approach. In the MOL approach, the partial differential equations can be discretized over spatial variable to convert into a system of differential-algebraic equations (DAEs). By numerically solving the DAEs, we are able to obtain the Li-ion concentration profiles at any time during discharge process.

2.3. References

1. J.L. Allen, T. R. Jow, and J. Wolfenstine, Kinetic study of the electrochemical $FePO_4$ to $LiFePO_4$ phase transition. *Chem. Mat.* **19**, 2108-2111 (2007)

2. X. P. Wang, G. Corbel, S. Kodjikian, Q. F. Fang, and P. Lacorre, Isothermal kinetic of phase transformation and mixed electrical conductivity in Bi_3BbO_7. *J. Solid State Chem.* **179**, 3338-3346 (2006).
3. B. W. Leitch and S.-Q. Shi, Accommodation energy of formation and dissolution for a misfitting precipitate in an elastic-plastic matrix. *Model. Simul. Mater. Sci. Eng.* **4**, 281-292 (1996).
4. E. Gamsjager, T. Antretter, C. Schmaranzer, W. Preis, C. M. Chimani, N. K. Simha, J. Svoboda, and F. D. Fischer, Diffusional phase transformation and deformation in steels. *Comput. Mater. Sci.* **25**, 92–99 (2002).
5. J. Svobaoda, F. D. Fischer, P. Fratzl, E. Gamsjager, and N. K. Simha, Kinetics of interfaces during diffusional transformations. *Acta Mater.* **49**, 1249-1259 (2001).
6. M. J. Santofimia, L. Zhao, and J. Sietsma, Model for the interaction between interface migration and carbon diffusion during annealing of martensite-austenite microstructure in steels. *Scr. Mater.* **59**, 159-162 (2008).
7. M. J. Santofimia, J. G. Speer, A. J. Clarke, L. Zhao, and J. Sietsma, Influence of interface mobility on the evolution of austenite-martensite grain assemblies during annealing. *Acta Mater.* **7**, 4548-4557 (2009).
8. J. G. Speer, R. E. Hackenberg, B. C. Decooman, and D. K. Matlok, Influence of interface migration during annealing of martensite/austenite mixtures. *Philosophical Magazine Letters* **87**, 379-382 (2007).
9. R. A. Huggins, *Advanced batteries: materials science aspect*. Springer, New York, London, 2009.

10. M. Z. Bazant, Phase-field theory of ion intercalation kinetics. arXiv:1208.1587v1.

11. P. Bai, D. A. Cogswell, and M. Z. Bazant, Suppression of phase separation in $LiFePO_4$ nanoparticles during battery discharge. *Nano Lett.* **11**, 4890-4896 (2011).

12. A. Van der Ven, and M. Wagemaker, Effect of surface energies and nano-particle size distribution on open circuit voltage of Li-electrodes. *Electrochem. Commun.* **11**, 881-884 (2009).

13. N. Meethong, H. -Y. S. Huang, S. A. Speakman, W. C. Carter, and Y. M. Chiang, Strain accommodation during phase transformations in olivine-based cathodes as a materials selection criterion for high-power rechargeable batteries. *Adv. Funct. Mater.* **17**, 1115-1123 (2007).

14. D. A. Porter and K. E. Easterling, *Phase transformations in metal and alloys*; New York, 1981; p287-290.

15. C. Wang, U. Kasavajjula, and P. E. Arce, A discharge model for phase transformation electrodes: formulation, experimental validation, and analysis. *J. Phys. Chem. C* **111**, 16656-16663 (2007).

16. C. J. Wen, B. A. Boukamp, and R. A. Huggins, Thermodynamic and mass transport properties of 'LiAl'. *J. Electrochem. Soc.* **126**, 2258-2266 (1979).

17. T. C. Illiingworth, and I. O. Golosnoy, Numerical solutions of diffusion-controlled moving boundary problems which conserve solute. *J. Comp. Phys.* **209**, 207-225 (2005).

Chapter 3: Strain Accommodation and Potential Hysteresis of $LiFePO_4$ Cathode during Lithiation and Delithiation

In Chapter 2, we developed a mixed-control model for phase transformation electrode materials, which considered the elastic-plastic accommodation energy induced by lattice mismatch between the two phases during phase transition. Similar to the metal-hydrogen system in which the presence of transformation strain usually resulted into pressure hysteresis between the hydride formation and decomposition [1], the strain accommodation energy during lithiation and delithiation in phase transformation electrode materials will also cause potential hysteresis between charge and discharge processes. In this Chapter, we use $LiFePO_4$ as an example to study the strain accommodation and potential hysteresis during phase transition.

$LiFePO_4$ has been considered to be a promising candidate material for the cathode of high-power, safe, low-cost and long-life Li-ion batteries required for hybrid electric vehicles and renewable energy storage. The most striking characteristic of this material is a flat charge/discharge profile at the potential of ~3.4 V versus Li/Li^+ due to the phase transformation. However, pure $LiFePO_4$ suffered from poor rate capability due to low intrinsic electronic/ionic conductivity and slow phase transformation. A significant amount of efforts, such as size reduction [2], cation doping [3] and surface coating [4], have been put to improve the electrochemical performances of $LiFePO_4$. However, only few studies have been focused on the phase transformation [5-8]. Since most capacity of $LiFePO_4$ comes from a first-order phase transformation, an understanding of the kinetics of the phase transformation is critical to achieving a high power density for $LiFePO_4$, especially for the carbon-coated nano-$LiFePO_4$ where the electronic and ionic transport have been greatly improved and the slow phase transformation may be a limiting step for the rate performance. Recent research demonstrated that the phase transformation in $LiFePO_4$ is strongly controlled by the strain accommodation effect induced from the volume difference between the lithiated and delithiated phases [5]. The misfit strain between the triphylite phase ($Li_{1-y}FePO_4$, y=0.1~0.2) and the heterosite phase (Li_xFePO_4, x=0.05~0.1) in nano-$LiFePO_4$ particles was detected using X-ray diffraction (XRD) [5], and dislocations induced by misfit strain were observed in plate-like $LiFePO_4$ particles using transmission electron microscopy (TEM) [9]. Such a strain-induced energy penalty can decrease the driving force for phase transformation [10], resulting in decrease of the phase transformation rate [11]. The accommodation energy decreases the lithiation equilibrium potential but increases the delithiation potential, resulting in an equilibrium potential hysteresis [1]. It was reported that shrinking the $LiFePO_4$ particle size can narrow the miscibility gap between the lithiated and delithiated phases and decrease the equilibrium potential hysteresis [5]. The fast phase transformation may be one of the reasons for the excellent rate performance of carbon-coated nano-$LiFePO_4$.

3.1. Experimental Methods

Two $LiFePO_4$ samples were provided by a commercial supplier. Transmission electron microscopy (TEM) images for both samples were recorded on a Hitachi HF-2000 FEG-TEM, and the results were shown in Figure 3.1. The $LiFePO_4$ samples consisted of aggregates of secondary nano-scale crystals with average sizes of 40 nm (Figure 3.1a) and 100 nm (Figure 3.1b). The thin carbon coating (2-4 nm) and crystalline single phases of $LiFePO_4$ can be clearly observed in the high resolution TEM images (Figure 3.1c), in which the boundaries between $LiFePO_4$ crystal and carbon coating have been marked by red dashed line. All electrochemical tests in this Chapter were performed by using three-electrode pouch cells. The $LiFePO_4$ cathodes containing 82 wt% active material, 10 wt% carbon black and 8 wt% poly(vinylidesfluoride) (PVDF) in 1-methyl-2-pyrrolidinone (NMP) solvent were prepared by the slurry coating method. The formulation was coated onto aluminum foil with a loading of 2.5 mg/cm^2 of $LiFePO_4$. The three-electrode pouch cells were assembled in an Ar-filled glove box, using lithium metal as the reference and counter electrodes, 1M $LiPF_6$ in 1:1:1:3 ethylene carbonate (EC):dimethyl carbonate (DMC):diethyl carbonate (DEC):ethylmethyl carbonate (EMC) as electrolyte and Celgard 3501 as the separator.

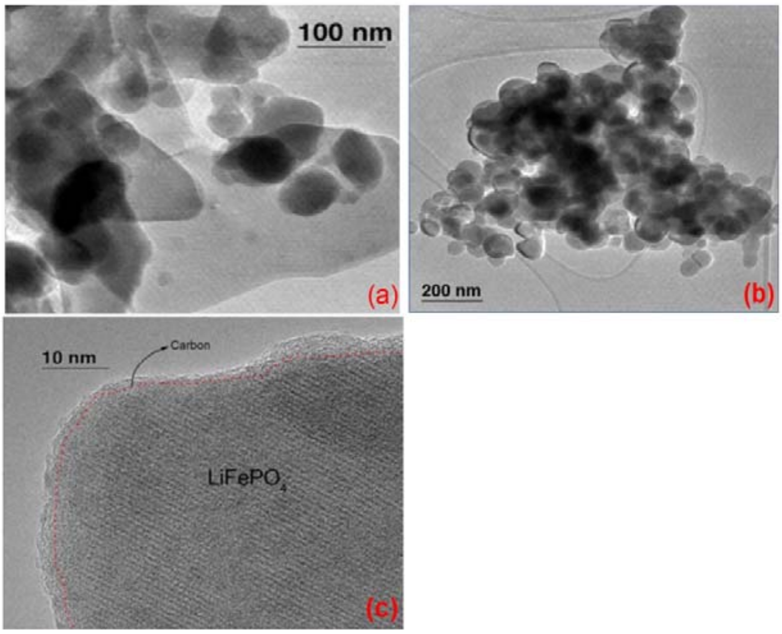

Figure 3.1. TEM images for (a) $LiFePO_4$ with secondary particle size ~40 nm and (b) $LiFePO_4$ with secondary particle size ~100 nm; (c) The carbon coating layer on a crystal $LiFePO_4$ particle is marked in HRTEM.

To measure the relationship between equilibrium potential (fully relaxed open-circuit-potential (OCP)) and state of charge (SOC) or state of discharge (SOD), cells were tested using a galvanostatic intermittent titration technique (GITT). All the GITT tests have been performed by using *Arbin* test station. GITT measurements consisting of a series of current pulses were applied to the three-electrode pouch cells at a low current less than $0.022C$ for 2 h, each followed by a 16 h rest process. The OCP at the end of the 16th h is considered to be the equilibrium potential. The potential decay during the rest process includes both relaxation and self-discharge. $LiFePO_4$ electrodes cannot be fully relaxed to equilibrium if the relaxation time is too short. However, a relaxation time that is too long will greatly increase the testing time, resulting in noticeable self-discharge. The potential decay will be mainly controlled by self-discharge if relaxation time is much longer than 16 h, as evidenced from the capacity difference between charge GITT and discharge GITT. The relaxation time of 16 h was selected to allow full relaxation of OCP and to minimize the self-discharge of $LiFePO_4$ during the test. The potentials of 2.2 V and 4.2 V were used as the low and high cutoff voltages in GITT tests.

To characterize the equilibrium potential hysteresis of $LiFePO_4$ in the phase transformation region, cyclic voltammetry (CV) at a scan rate of 0.05 mV/s was performed on electrodes at the middle of potential hysteresis between 50% SOC and 50% SOD using different scan potential amplitudes. A low scan rate of 0.05 mV/s is used here to decrease the influence of lithium ion diffusion on the current but detect the phase transformation current [12]. Similarly, electrochemical impedance spectroscopy (EIS) was also applied on the $LiFePO_4$ cathodes at 50% SOC, 50%

SOD and at the middle of potential hysteresis between 50% SOC and 50% SOD. Before CV and EIS tests, the electrodes were charged/discharged between 2.2 to 4.2 V at 0.1*C* current for two cycles. Both CV and EIS tests were performed on Solatron 1260/1287 Electrochemical Interface (Solatron Metrology, UK).

3.2. Equilibrium Potential Hysteresis of $LiFePO_4$ Induced by Accommodation Energy

Delithiation/lithiation of $LiFePO_4$ is usually accompanied by phase transformation between heterosite phase (α phase) and triphylite phase (β phase) [5]. The formation of potential hysteresis during delithiation and lithiation of $LiFePO_4$ is discussed below. In brief, during Li-ion insertion, the lattice parameters of the Li_xFePO_4 ($0<x<1$) system vary with the lithium stoichiometry x and phase transformation. Since the newly formed phase has a different molar volume with that of the matrix [5, 13], strain and stress will be generated during Li-ion insertion into $FePO_4$ to accommodate the volume change. For a purely elastic matrix, elastic energy will be stored in the matrix and the newly formed phase during phase transformation [14]. For a plastic matrix with a low yield strength, the elastic energy stored in the matrix will be relaxed and spent in creating plastic deformation [15]. Normally, the electrode materials are elastic-plastic solid, the transformation energy is accommodated by both elastic and plastic energy [14]. The plastic deformation in $LiFePO_4$ during phase transformation has been evidenced from the existence of dislocations and fracture [9, 16]. The elastic-plastic accommodation energy is an energy barrier against lithiation and delithiation [10]. It increases the free energy of the material and decreases the lithiation equilibrium potential. According to Chapter 2, the decrease of lithiation equilibrium (open-circuit) potential $\Delta E_{lithiation}$ can be determined from [14, 17]

$$\Delta E_{lithiation} = E_e - E_{de} = \frac{\Delta G_{lithiation}^{elastic} + \Delta G_{lithiation}^{plastic}}{\Delta nF} \tag{3.1}$$

where E_e is the theoretical (*stress-free*) equilibrium potential, E_{de} is the discharge equilibrium potential measured by experiments during Li-ion insertion, Δn is the number of lithium atoms to convert parent phase to new phase and F is the Faraday's constant. The accommodation energy increases with the depth of discharge process, which is similar to the strain-hardening phenomenon observed in phase transformation of metal hydrides [18].

During Li-ion extraction, a reverse phase transformation will occur. The volume changes during the Li-ion extraction will also be accommodated by the elastic-plastic process outlined above. Different from the lithiation process, the accommodation energy during Li-ion extraction increases the electrode potential. The potential increase during the charge (delithiation) process can be calculated as

$$\Delta E_{delithiation} = E_{ce} - E_e = \frac{\Delta G_{delithiation}^{elastic} + \Delta G_{delithiation}^{plastic}}{\Delta nF} \tag{3.2}$$

where E_{ce} is the charge equilibrium potential measured by experiments during delithiation. The accommodation processes during Li-ion insertion and extraction dissipate energy to the surroundings, resulting in an open-circuit-potential hysteresis ($\Delta E_{lithiation} + \Delta E_{delithiation}$). Therefore, the open-circuit-potential hysteresis during Li-ion insertion and extraction can be calculated from the accommodation energy. From the accommodation energy of Li-Sn alloy, Hirai *et al.* [10] calculated the lithiation equilibrium potential of Sn using Eq. (3.1), which is in excellent agreement with measured data. Eqs. (3.1) and (3.2) have also been applied in the metal-hydrogen system for determining the pressure hysteresis of metal-hydrides from their accommodation energy [1].

Equilibrium potential hysteresis of phase transformation electrode materials during lithiation and delithiation can easily be determined by using GITT, however, the accommodation energy is very difficult to obtain especially for new electrode materials. Based on the relationship between potential hysteresis and accommodation energy shown in Eqs. (3.1) and (3.2), the accommodation energy can be calculated from equilibrium potential hysteresis.

The following reaction occurs during phase transformation from heterosite (Li_xFePO_4) to triphylite ($Li_{1-y}FePO_4$).

$$Li_xFePO_4(\alpha\text{ phase}) + (1-y-x)Li \xrightarrow{lithiation} Li_{1-y}FePO_4(\beta\text{ phase}) \quad (3.3)$$

When the accommodation energy ($\Delta G^{accomm}_{lithiation} = \Delta G^{elastic}_{lithiation} + \Delta G^{plastic}_{lithiation}$) change during lithiation is defined as the energy associated with *the production of one mole of new phase*, the accommodation energy for the lithiation process can be expressed as

$$\Delta G^{accomm}_{lithiation} = (1-x-y)F\Delta E_{lithiation} \quad (3.4)$$

Since the values of *x, 1-y* and $\Delta E_{lithiation}$ can be obtained from the equilibrium potential-composition isotherm curves [14], the accommodation energy can be calculated by using Eq. (3.4). Similarly, the accommodation energy during delithiation can also be obtained by using

$$\Delta G^{accomm}_{delithiation} = (1-x-y)F\Delta E_{delithiation} \quad (3.5)$$

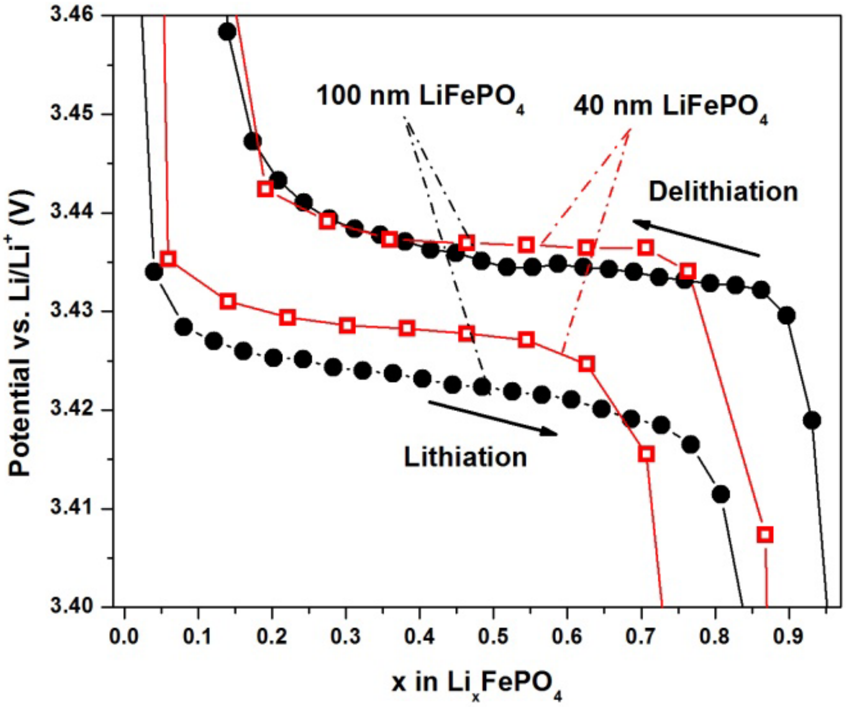

Figure 3.2. GITT equilibrium potentials for $LiFePO_4$ with different particle sizes.

The equilibrium potential of $LiFePO_4$ with secondary particle sizes of 40 nm and 100 nm were tested at different levels of lithiation and delithiation (Figure 3.2). The equilibrium potentials of both $LiFePO_4$ electrodes gradually decreased with Li-ion insertion but increased with Li-ion extraction. This is also observed by other research group [6]. Both $LiFePO_4$ particles have a similar delithiation equilibrium potential within the miscibility gap; however, the lithiation equilibrium potential of 40 nm $LiFePO_4$ is 5-6 mV higher than that of 100 nm $LiFePO_4$, which is well in agreement with the observations of other research groups [19]. Since the delithiation equilibrium potentials are almost the same for both $LiFePO_4$ samples, the high lithiation potential of 40 nm $LiFePO_4$ results in a smaller potential hysteresis (8-10 mV), compared to the 12-15 mV for 100 nm $LiFePO_4$. In addition, nano-scale (40 nm) $LiFePO_4$ has a reduced miscibility gap compared to coarser-grained (100 nm) materials. The variation in equilibrium potential of 40 nm $LiFePO_4$ during Li-ion insertion and extraction is less than that of 100 nm $LiFePO_4$. The results in Figure 3.2 are consistent with data reported by other researchers [5, 6, 19].

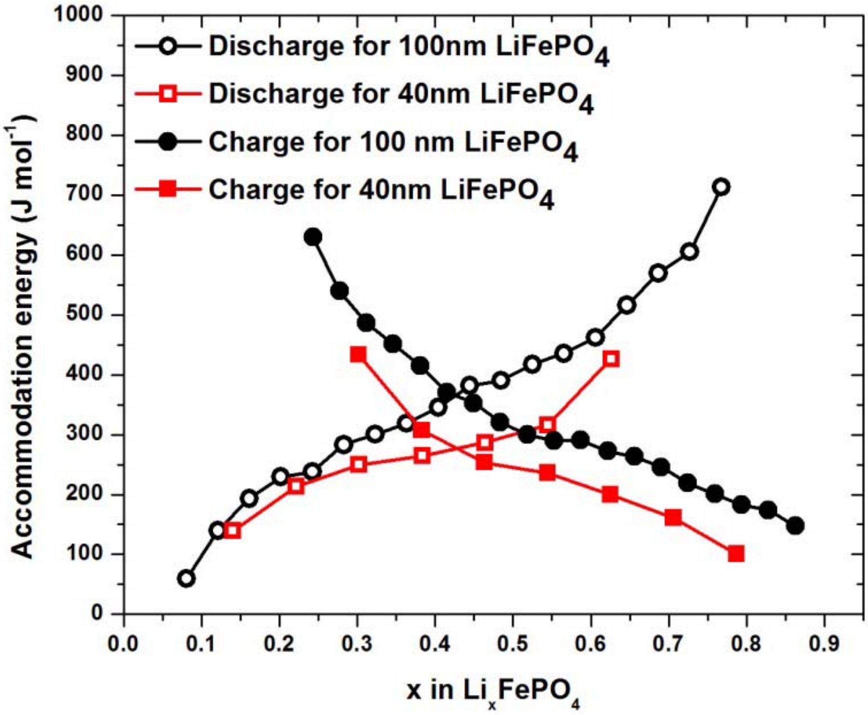

Figure 3.3. Discharge and charge accommodation energy for $LiFePO_4$ with different particle sizes.

The accommodation energy of $LiFePO_4$ with different particle sizes during the first cycle of lithiation and delithiation in the phase transformation region was calculated by using Eqs. (3.4) and (3.5) and shown in Figure 3.3. The theoretical equilibrium potential E_e is defined as the average values of potential, at which the charge and discharge phase transformation initiated. The accommodation energy of both $LiFePO_4$ samples increased with SOD and SOC. At $Li_{0.5}FePO_4$, the discharge (lithiation) accommodation energy is larger than the charge (delithiation) accommodation energy. The reduced accommodation energy in charge compared to discharge may be one of the reasons for higher charge rate capability of $LiFePO_4$ than that for discharge [20]. Compared to 100 nm $LiFePO_4$, 40 nm $LiFePO_4$ has a lower accommodation energy due to a small potential hysteresis and a reduced miscibility gap in nano-sized $LiFePO_4$ [6]. Both the short diffusion length and a low accommodation energy in nano-$LiFePO_4$ accelerate the phase transformation rate, resulting in high rate performance [5].

It has been reported that dislocations and other defects were generated during the first cycle of Li-ion insertion/extraction in $LiFePO_4$ [9, 16]. These defects change the accommodation energy in the following cycles. Therefore, the accommodation energy in the second charge/discharge cycle may be different from the values in the first cycle. Figure 3.4a compares the equilibrium potentials of 100 nm $LiFePO_4$ in the first and second charge/discharge cycles. The corresponding accommodation energies in the first and second charge and discharge cycles are illustrated in Figure 3.4b. As shown in Figure 3.4a, the discharge equilibrium potential in the second charge/discharge cycle is almost the same as that in the first cycle, but the charge equilibrium potential in the second charge/discharge cycle is lower than that in the first cycle at later SOC. The lower charge equilibrium potential induced lower charge accommodation energy in the second charge cycle. These behaviors are most likely due to (i) the introduction of dislocations and/or fractures in micro-$LiFePO_4$ in the first charge/discharge cycle, which lowered the energy required for phase growth for the second charge cycle, and (ii) the volume expansion/shrinkage of $LiFePO_4$ during the first charge/discharge cycle, which may locally rearrange the position of $LiFePO_4$ particles to accommodate the stress. The reduced accommodation energy during the initial charge/discharge cycles is consistent with the activation process of $LiFePO_4$

electrodes. However, why these defects only affect the charge accommodation energy but not the discharge accommodation energy is not clear.

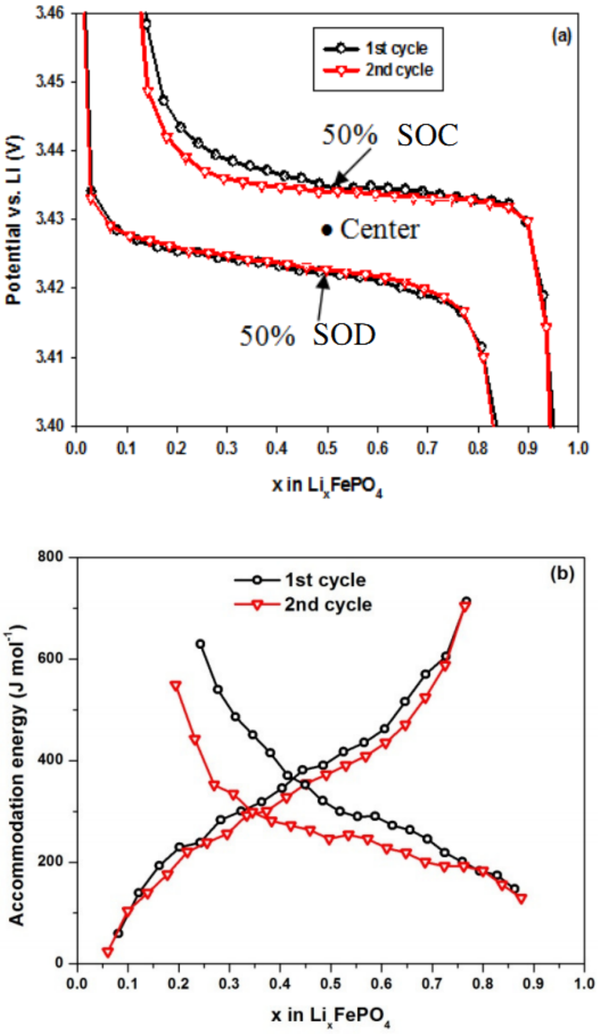

Figure 3.4. (a) GITT equilibrium potential at different cycles, (b) charge and discharge accommodation energy at different cycles.

As shown in Figure 3.4b, the discharge accommodation energy of 100 nm LiFePO$_4$ increased up to 750 J/mol when Li$_x$FePO$_4$ (α phase) gradually transformed into Li$_{1-y}$FePO$_4$ (β phase). The maximum accommodation energy (750 J/mol) of LiFePO$_4$ during phase transformation from Li$_x$FePO$_4$ to Li$_{1-y}$FePO$_4$ is less than the accommodation energy (972 J/mol) of Nb during phase transformation from Nb to

NbH [14] and is much smaller than the accommodation energy (9630 J/mol) of Sn during phase transformation from Sn to $Li_{0.4}Sn$ [10]. Therefore, the exceptional rate performance of $LiFePO_4$ may be partially attributed to the lower accommodation energy during phase transformation compared to Sn anode for Li-ion battery and Nb-hydride anodes for Ni/MH batteries.

3.3. Characterization of Potential Hysteresis with GITT

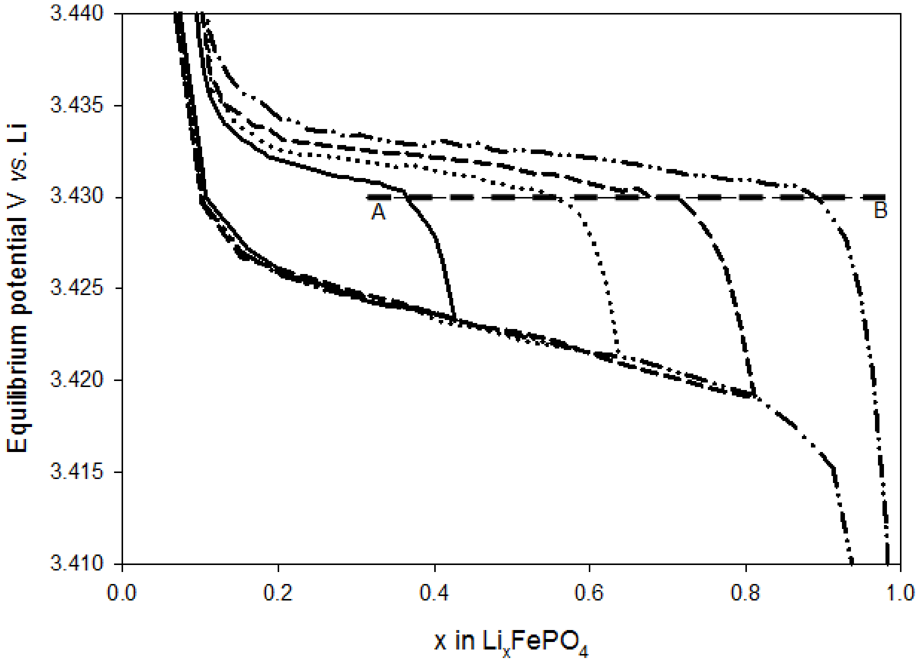

Figure 3.5. Charge equilibrium potential of 100 nm $LiFePO_4$ following SOD 40%, 60%, 80, and 100%. Discharge and charge current: 0.022C, discharge time: 2h, charge time: 0.33h for 40% and 0.67h for 60, 80 and 100%. Rest time for charge and discharge: 8h.

To characterize the property of equilibrium potential hysteresis in $LiFePO_4$, the delithiation equilibrium potential of 100 nm $LiFePO_4$ was measured after being equilibriately discharged to different levels (SOD: 40%, 60%, 80% and 100%) using GITT, and the result was shown in Figure 3.5. At a given Li-ion concentration, the charge equilibrium potential increased with the depth of the previous SOD. For example, the electrode with composition $Li_{0.3}FePO_4$, which was previously completely discharged, has the highest charge equilibrium potential, while the $Li_{0.3}FePO_4$ electrode that was previously discharged to $Li_{0.4}FePO_4$ has the lowest charge equilibrium potential. At a given SOC, the more Li-ion insertion into $FePO_4$ in the previous discharge, the higher the equilibrium potential of the following charge process. However, the initial potential for the phase transformation from β to α phase during charge process occurs at the same value (see A-B line in Figure 3.5) no matter how much Li-ion was inserted into $FePO_4$ in the previous discharge process. If the charge equilibrium potential curves following SOC 40%, 60% and 80% are moved to the charge potential curve following SOC 100% discharge state along the A→B direction, four charge lines will be completely overlapped. Therefore, the charge equilibrium potentials following different SOD levels are solely attributed to the fraction of newly formed α phase rather than the fraction of α phase left during previous SOD.

To illustrate the kinetics of charge and discharge of $LiFePO_4$, the potential responses during each current pulse in the GITT measurement were recorded and shown in Figure 3.6. Due to the resolution limitation of *Arbin* equipment, the potential jump due to solid-electrolyte-interphase (SEI) resistance and fast charge transfer reaction cannot be monitored. The polarization curves recorded in Figure 3.6 only reflect voltage change due to Li-ion diffusion and the phase transformation. As demonstrated in Figure 3.6, the overpotential increased with the fraction of phase transformation (both in charge and discharge).

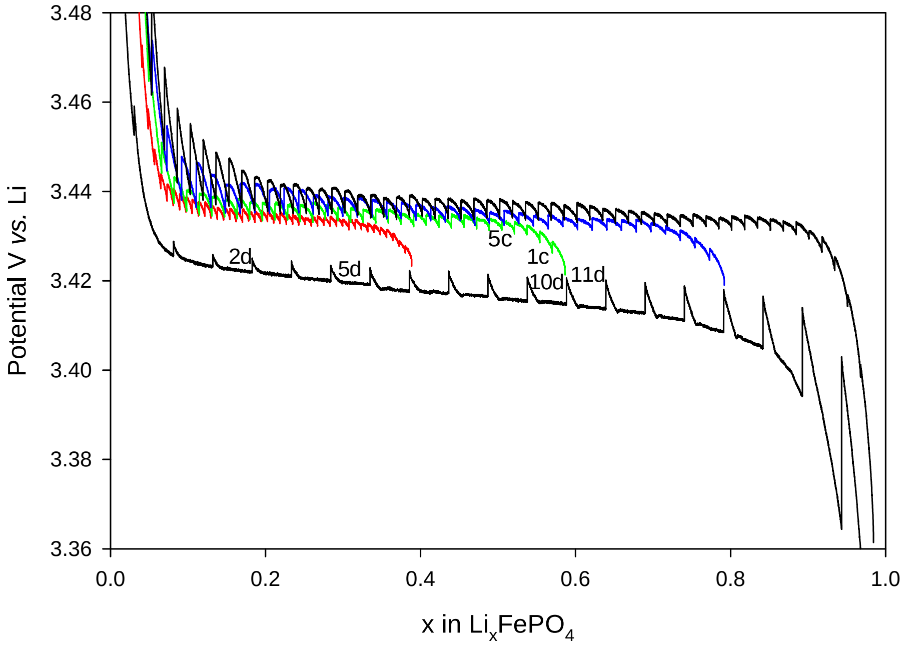

Figure 3.6. Charge GITT curves following different SOD.

To investigate the kinetics of discharge at different SOD, the GITT potential-time profiles at the 2nd, 5th and 10th discharge pulse were compared by shifting their initial open-circuit potentials together, as shown in Figure 3.7. The change in OCP (ΔE in Figure 3.7) for three current pulses is almost the same. However, overpotential (the potential difference between fully relaxed OCP and the potential at the end of the current pulse) in Figure 3.7 increased with SOD. By carefully comparing the potential response in each current pulse (Figure 3.7), we found that the initial potential exponentially drops, followed by an almost linear decrease with time. The initial potential drop is due to the Li-ion diffusion, and the later slow decrease in potential is attributed to the phase transformation. The diffusion polarization quickly increases with SOD, but the phase transformation polarization only slightly changes with SOD. Figure 3.7 demonstrates that the increase in overpotential with SOD is mainly attributed to the increase in Li-ion diffusion length due to growth of the β phase. The increase in diffusion overpotential with phase transformation was also observed in the lithiation/delithiation of graphite [21].

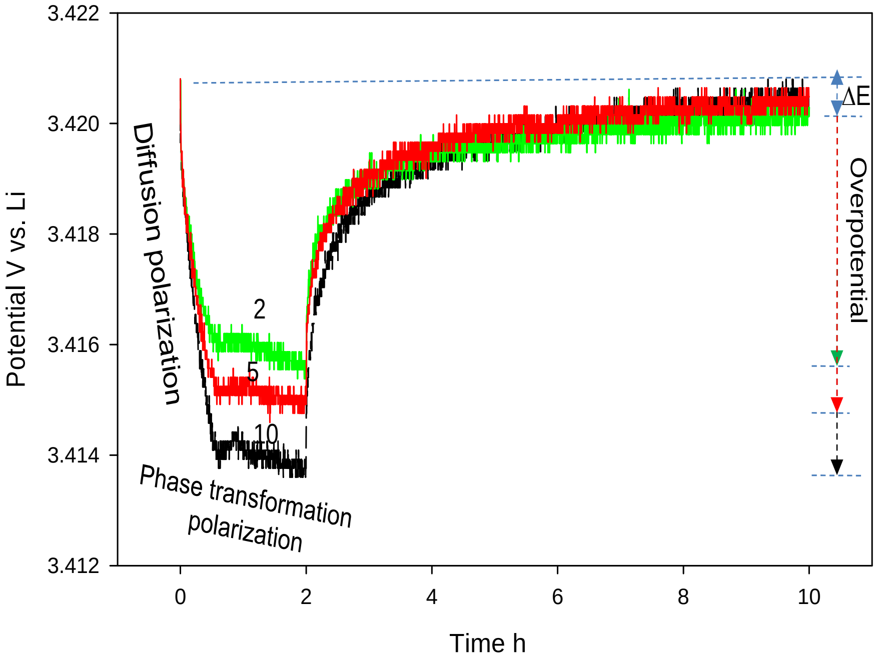

Figure 3.7. Discharge and following rest processes during GITT at the 2nd, 5th and 10th current pulses.

The charge GITT following different SOD was used to characterize potential hysteresis. As shown in Figure 3.6. the polarization curves are SOD-independent, i.e. the potential responses in charge GITT following different SOD were similar at the same potential level except for 40% SOD in which the charge time of $LiFePO_4$ was shortened from 0.66 h (for all other SOD) to 0.33 h to get more equilibrium potential data. To clearly show the potential response, the discharge and charge GITT curves at 60% SOD were enlarged and shown in Figure 3.8. The potential response in each charge GITT curve shows only exponential increase (diffusion polarization) without linear polarization (phase transformation polarization) until the 7th charge GITT curve, where the polarization potential exceeds the charge equilibrium potential and phase transformation occurs. Therefore, no phase transformation occurs inside potential hysteresis region. Although in the potential hysteresis region, $LiFePO_4$ still consists of two phases, it behaves like a solid solution. Here, we need to point out that during charge/discharge, in the potential hysteresis region, Li ions can penetrate across the phase boundary, and the phase boundary between two phases in $LiFePO_4$ does not move, which is different from the behavior of phase transformation and similar to solid solution. The solid solution behavior in the potential hysteresis region is also supported by the fact that the charge polarization curves after different SOD are similar to the charge polarization curves after fully discharged (100% SOD), shown in Figure 3.6, and the fully discharged (100% SOD) $LiFePO_4$ is a solid solution before the charge potential reaches the charge equilibrium potential. In addition, the first charge overpotential is much smaller than the previous discharge overpotentials. For example, the overpotential at the 10th discharge GITT (10d in Figure 3.8) is around 6.0 mV at the discharge current of 0.022C. However, the overpotential in the first charge GITT (1c in Figure 3.8) is only 3 mV at the same current, while the overpotential in the following discharge GITT (11d in Figure 3.8) is 7 mV. The difference between the 11th discharge and the 1st charge is that phase transformation occurs in the 11th discharge, while no phase transformation takes place in the 1st charge. The phase transformation overpotential at the 11th discharge GITT is around 4.0 mV, which is 57% of the total (phase transformation and diffusion) overpotential.

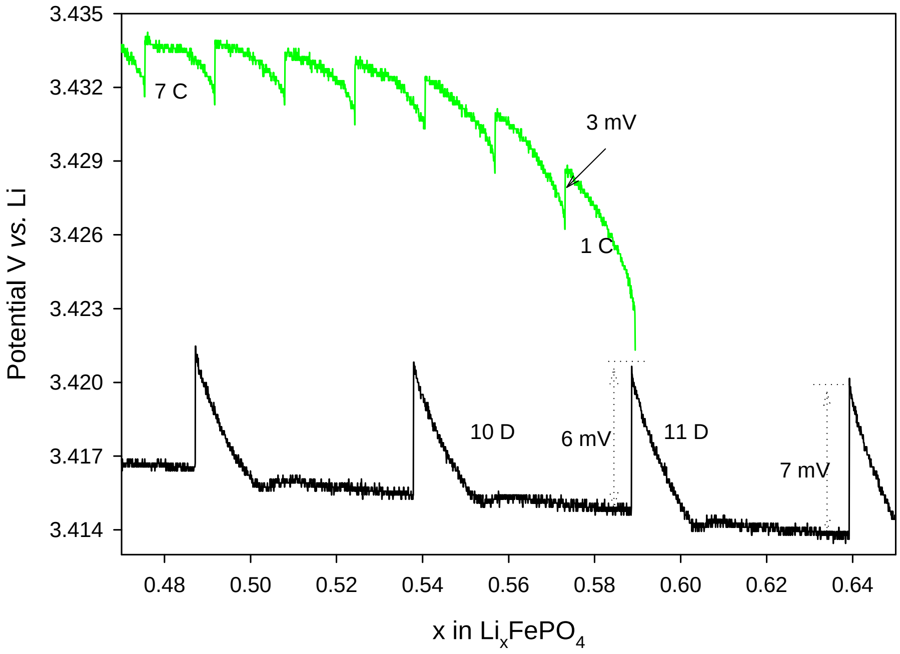

Figure 3.8. Charge and discharge GITT at 60% SOD.

3.4. Characterization of Phase Transformation Potential Hysteresis with CV and EIS

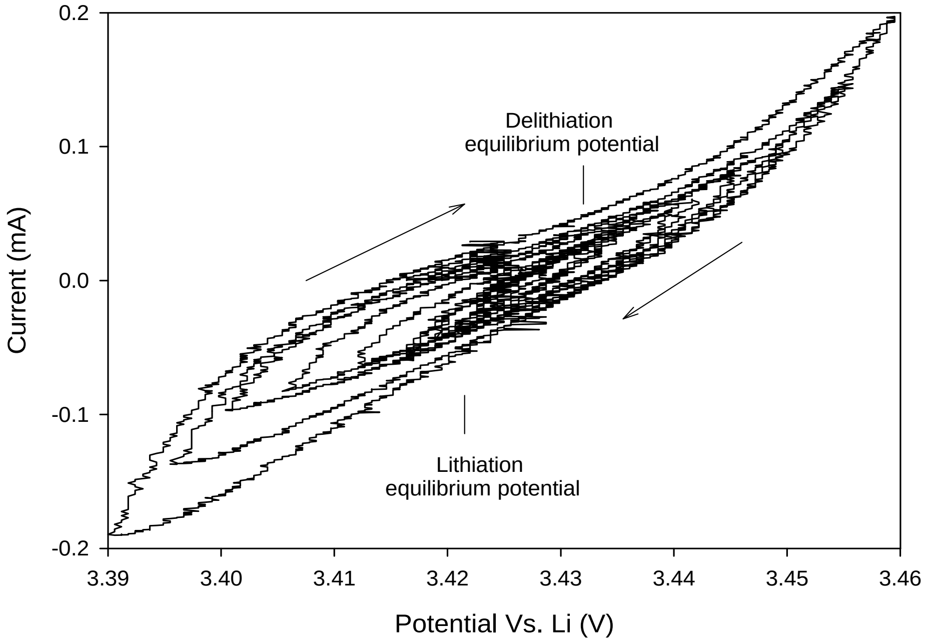

Figure 3.9. CV performed at the middle of voltage hysteresis with different amplitude.

Phase transformation in $LiFePO_4$ occurs only when the applied potential is lower than the lithiation equilibrium potential or higher than delithiation equilibrium potential. $LiFePO_4$ in the potential hysteresis range can be considered as a solid solution material. Cycle voltammetry (CV) is a common and useful tool to distinguish the phase transformation from a solid solution behavior because the current will be enhanced in the phase transformation region. Figure 3.9 shows the CV scans of 100 nm $LiFePO_4$ at the center of potential hysteresis (marked in Figure 3.4a) by using different scan potential amplitudes but a fixed scan rate of 0.05 mV/s. Before each CV measurement, the 100 nm $LiFePO_4$ electrode was fully charged to 4.2 V and then discharged to SOD 50% followed by charging the electrode to 3.427 V and holding the electrode at this potential for 2 h. 3.427 V is the potential halfway between lithiation potential (3.422 V) and delithiation potential (3.432 V). By changing the amplitude of CV (±2, ±4, ±6, ±8, ±10, ±12, ±15, ±20, ±25, ±30, ±35 mV), the reversibility of the reactions inside and outside of the potential hysteresis range was characterized. When the amplitudes of CV are similar or less than the half value of potential hysteresis (6-8 mV), the potential almost linearly changed with current. However, for CV with a large amplitude (>12 mV), a rapid increase in current was observed when the lithiation potential was below 3.42 V and delithiation potential was above 3.435V, which is due to the phase transformation. The CV scans starting at the center of potential hysteresis with different potential amplitudes demonstrated solid solution behavior inside the potential hysteresis and phase transformation characteristic outside of the potential hysteresis range.

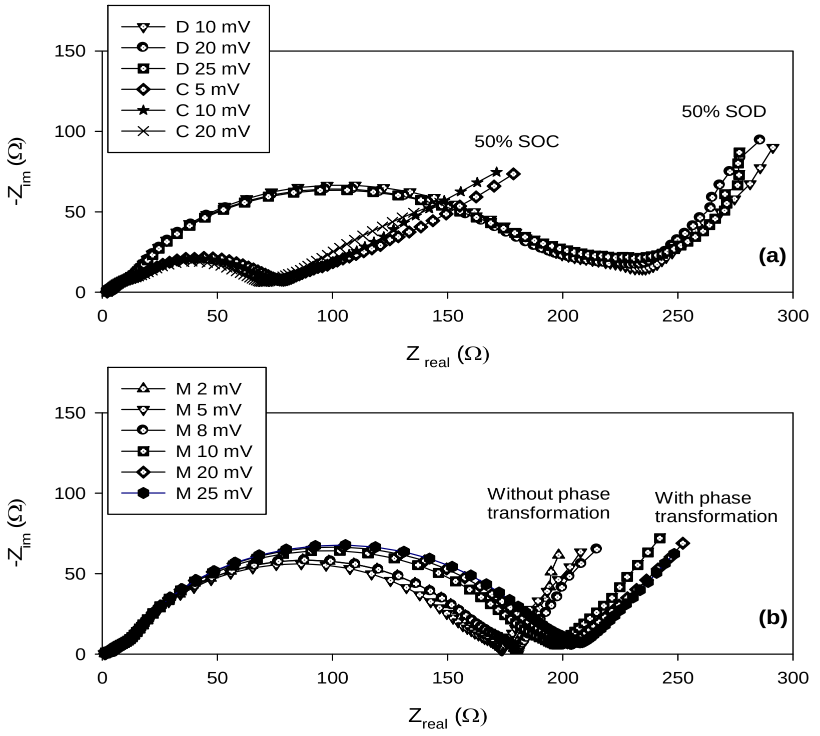

Figure 3.10. EIS plots measured at (a) OCP of 50% SOD and 50% SOC, and (b) the middle of the potential hysteresis with different voltage amplitudes.

EIS has been widely used in Li-ion batteries to evaluate the charge/discharge kinetics. A reliable EIS can be obtained only if the system satisfies the criteria of linearity and time invariance (LTI) [22]. If EIS is measured at the open-circuit after charging or discharging to a given state, the phase transformation occurs only in the forward potential scan, not in the backward potential scan, resulting in a SOD or SOC shift during EIS measurement. Therefore, $LiFePO_4$ is not a linear and time invariant system if EIS is measured at the certain charge or discharge states, and the EIS tests normally measured at different SOD or SOC are not reliable. A reliable and useful EIS can only be obtained by shifting the testing potential to the center of the potential hysteresis. Figure 3.10 shows the EIS plots measured at 50% SOD, 50% SOC and in the center of the potential hysteresis (marked in Figure 3.4a) with different potential amplitudes. To alleviate OCP shift during the EIS measurement, the $LiFePO_4$ sample after each EIS measurement at 50% SOD (or 50% SOC) was fully re-charged (or fully re-discharged for SOC) and then discharged to 50% SOD (or charged to 50% SOC) for the following EIS tests. The impedances of $LiFePO_4$ in Figure 3.10 consist of two semicircles and a sloped line. For a solid solution electrode, the high frequency semicircle in EIS is attributed to the SEI film, middle frequency semicircle to charge transfer, and low frequency line to diffusion. The impedance at 50% SOC is much smaller than that at 50% SOD, resulting in higher rate capability in charge than in discharge. EIS in both 50% SOD and 50% SOC are less sensitive to signal amplitude. Since the EIS performed at charge or discharge equilibrium states is not reliable, EIS should be performed at the center of potential hysteresis. When the EIS test is conducted at the center of potential hysteresis using amplitudes less than half of the potential hysteresis, the $LiFePO_4$ can be treated as a solid solution since no phase transformation occurs in the potential hysteresis region. When the amplitude of EIS test is much larger than half of the potential hysteresis, the phase transformation can happen. In this case, if the kinetics of forward phase transformation is similar to the backward phase transformation, a reliable EIS can still be obtained. The EIS measured at the center of potential hysteresis using different amplitudes was shown in Figure 3.10b. The impedances with amplitudes larger than half of the potential hysteresis have a larger second semicircle than those with amplitudes less than the potential hysteresis, which indicate that phase transformations cause additional impedance. The phase transformation impedance appears at a higher frequency than Li-ion diffusion impedance and is mixed with the impedance of the charge transfer reaction. The phase transformation impedance of $LiFePO_4$ was be obtained by subtracting impedance without phase transformation from phase transformation impedance. The phase transformation impedance of $LiFePO_4$ is around 20 Ω. The phase transformation impedance is 50% of total (phase transformation + ion diffusion) impedance, which is similar to the overpotential ratio (57%) obtained using GITT in Figure 3.8.

3.5. Summary

Equilibrium potential hysteresis in $LiFePO_4$ is a thermodynamic property, which is induced by strain accommodation energy. The OCP hysteresis of $LiFePO_4$ in the phase transformation region was determined by using the GITT method, and the corresponding accommodation energy was calculated according to the potential hysteresis. 40 nm $LiFePO_4$ has low accommodation energy during lithiation and delithiation, which is attributed to the narrow miscibility gap and small potential hysteresis. Phase transformation only occurs at a potential level above charge OCP or below discharge OCP. The $LiFePO_4$ inside potential hysteresis region behaves like a solid solution. Normal EIS obtained at different SOD or SOC cannot satisfy the criteria of linearity and time invariance (LTI). A reliable EIS can be obtained at the center of potential hysteresis, and phase transformation impedance can be obtained by changing the amplitude of the EIS signal from less than to greater than half of the potential hysteresis.

3.6. References

1. R. Balasubramaniam, Hysteresis in metal-hydrogen systems. *J. Alloy Compd.* **253**, 203-206 (1997).

2. X. L. Wu, L. Y. Jiang, F. F. Cao, Y. G. Guo, and L. J. Wan, $LiFePO_4$ nanoparticles embedded in a nanoporous carbon matrix: superior cathode material for electrochemical energy-storage devices. *Adv. Mater.* **21**, 2710-2714 (2009).
3. S. Y. Chung, J. T. Bloking, and Y. M. Chiang, Electronically conductive phospho-olivines as lithium storage electrodes. *Nat. Mater.* **1**, 123-128 (2002).
4. B. Kang and G. Ceder, Battery materials for ultrafast charging and discharging. *Nature* **458**, 190-193 (2009).
5. N. Meethong, H. -Y. S. Huang, S. A. Speakman, W. C. Carter, and Y. M. Chiang, Strain accommodation during phase transformations in olivine-based cathodes as a materials selection criterion for high-power rechargeable batteries. *Adv. Funct. Mater.* **17**, 1115-1123 (2007).
6. N. Meethong, Y. H. Kao, M. Tang, H. Y. Huang, W. C. Carter, and Y. M. Chiang, Electrochemically induced phase transformation in nanoscale olivines $Li_{1-x}MPO_4$ (M=Fe, Mn). *Chem. Mater.* **20**, 6189-6198 (2008).
7. C. Delmas, M. Maccario, L. Croguennec, F. L. Cras, and F. Well, Lithium deintercalation in $LiFePO_4$ nanoparticles via a domino-cascade model. *Nat. Mater.* **7**, 665-671 (2008).
8. G. Kobayashi, S. I. Nishimura, M. S. Park, R. Kanno, M. Yashima, T. Ida, and A. Yamada, Isolation of solid solution phases in size-controlled Li_xFePO_4 at room temperature. *Adv. Funct. Mater.* **19**, 395-403 (2009).

9. H. Gabrisch, J. Wilcox, and M. M. Doeff, TEM study of fracturing in spherical and plate-like $LiFePO_4$ particles. *Electrochem. Solid-state Lett.* **11**, A25-A29 (2008).

10. K. Hirai, T. Ichistubo, T. Uda, A. Miyazaki, S. Yagi, and E. Matsubara, Effects of volume strain due to Li-Sn compound formation on electrode potential in lithium-ion batteries. *Acta Materi.* **56**, 1539-1545 (2008).

11. E. Gamsjager, T. Antretter, C. Schmaranzer, W. Preis, C. M. Chimani, N. K. Simha, J. Svoboda, and F. D. Fischer, Diffusional phase transformation and deformation in steels. *Comput. Mater. Sci.* **25**, 92–99 (2002).

12. M. D. Levi and D. Aurbach, Simultaneous measurements and modeling of the electrochemical impedance and the cyclic voltammetric characteristics of graphite electrodes doped with lithium. *J. Phys. Chem. B* **101**, 4630-4640 (1997).

13. S-I. Pyun, J-Y. Go, and T-S. Jang, An investigation of intercalation-induced stresses generated during lithium transport through $Li_{1-\delta}CoO_2$ film electrode using a laser beam deflection method. *Electrochim. Acta* **49**, 4477-4486 (2004).

14. R. Balasubramaniam, Accommodation effects during room temperature hydrogen transformation in the niobium-hydrogen system. *Acta Metall. Mater.* **41**, 3341-3349 (1993).

15. H. K. Bimbaum, M. L. Grossbeck, and M. Amano, *J. Less-common Metals* 49, 357 (1976).

16. G. Y. Chen, X. Y. Song, and T. J. Richardson, Electron microscopy study of the $LiFePO_4$ to $FePO_4$ phase transition. *Electrochem. Solid State Lett.* **9**, A295-A298, (2006).

17. C. R. Krenn, Continuum modeling of transformation hysteresis in a metal hydride system. *Model. Simul. Mater. Sci. Eng*. **12**, S415-S424 (2004).

18. Y. Y. Earmme, W. C. Johnson, and J. K. Lee, Plastic relaxation of the transformation strain energy of a misfitting spherical precipitate: linear and power-law strain hardening. *Metall. Trans. A* **12**, 1521-1530 (1981).

19. K. T. Lee, W. H. Kan, and L. F. Nazar, Proof of intercrystallite ionic transport in $LiMPO_4$ electrodes (M=Fe, Mn). *J. Am. Chem. Soc.* **131**, 6044-6045 (2009).

20. V. Srinivasan and J. Newman. Existence of path-dependence in the $LiFePO_4$ electrode. *Electrochem. Solid-state Lett.* **9**, A110-A114 (2006).

21. C. Wang, I. Kakwan, A. J. Appleby, and F. E. Little, In situ investigation of electrochemical lithium intercalation into graphite powder. *J. Electroanal. Chem.* **489**, 55-67 (2000).

22. McC Siebert, W. *Circuits, Signals and System;,* The MIT Press and McGraw-Hill Book Company, New York, **1986**.

Chapter 4: Galvanostatic Intermittent Titration Technique and Potentiostatic Intermittent Titration Technique for Phase Transformation Electrode Materials

In Chapter 3, we investigated the potential hysteresis and accommodation energy for $LiFePO_4$ cathodes. We show that the thermodynamics of $LiFePO_4$ cathode is affected by its particle size. Rapid phase transformation through coherent or semi-coherent interface between $Li_{1-y}FePO_4$ and Li_xFePO_4 phases has been considered as one of the major reasons accounting for the fast electrochemical performance in nanosized $LiFePO_4$ [1, 2]. However, how the crystal structure, defects and particle size affect the diffusion coefficient of lithium ion and interface mobility of phase transformation electrodes are still not fully understood [1, 3-5] due to lack of reliable electro-analytical techniques for measuring lithium ion transport in phase transformation electrode materials. As shown in Chapter 1, since the analysis methods for both GITT and PITT were derived with the assumption of classical Fick's diffusion law, they are not reliable for measuring the ion diffusion coefficient in two-phase region of phase transformation electrode materials, where the ions are transported through both ion diffusion and movement of a phase boundary.

In this Chapter, we integrate the mixed-control model developed in Chapter 2 with GITT and PITT, which, for the first time, enable us to precisely determine the ion diffusion coefficient and the interface mobility of phase transformation electrode materials in the two-phase region. Taking the $LiFePO_4$ system as a specific example, we determined the Li-ion diffusion coefficient and interface mobility of two $LiFePO_4$

electrodes in two-phase region with average particle size of 500 nm and 1μm by using the mixed-control model integrated GITT and PITT. Since traditional analysis methods for GITT and PITT are considered to be reliable only in single phase region, the similarity between the diffusion coefficients in two-phase region determined by using mixed-control model integrated GITT and the ones in single phase region obtained from traditional GITT and PITT validates the mixed-control model.

4.1. Experiments

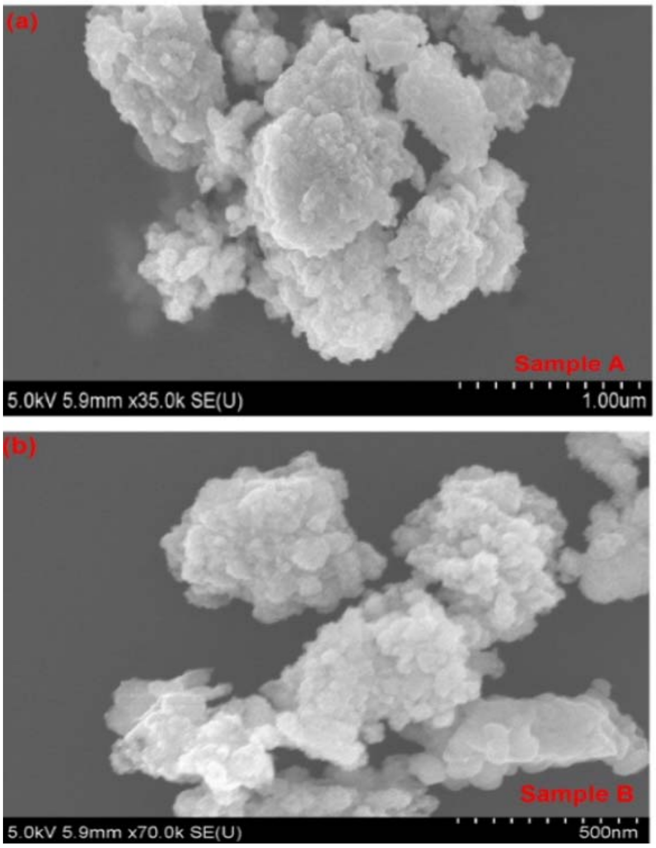

Figure 4.1. SEM images of two $LiFePO_4$ samples: (a) sample A~1μm primary particle aggregated with 100 nm second crystal particles; (b) sample B ~500nm primary particle consisting of 40 nm second crystal particles.

Two carbon-coated $LiFePO_4$ samples with particle sizes of ~1μm (sample A) and ~500 nm (sample B) were supplied by a commercial supplier. The 1μm $LiFePO_4$

sample consisted of highly dense aggregates of secondary nanosized crystal particles with an average size of 100 nm as shown in Figure 4.1a. Similarly, the 500 nm $LiFePO_4$ particles were aggregates of secondary particles with an average size of 40 nm as shown in Figure 4.1b. Due to the high density, it is believed that the electrolyte cannot penetrate into the $LiFePO_4$ particles through the nano-crystal grain boundary, and thus, the ion diffusion length should be half of the particle size rather than the crystal size (the size of the secondary particles). However, the crystal size will affect the strain accommodation energy and equilibrium potential during phase transformation [1, 2, 6, 7]. The X-ray diffraction (XRD) patterns of the two $LiFePO_4$ samples, shown in Figure 4.2, demonstrated the two commercial $LiFePO_4$ powders were well crystallized without any noticeable impurity.

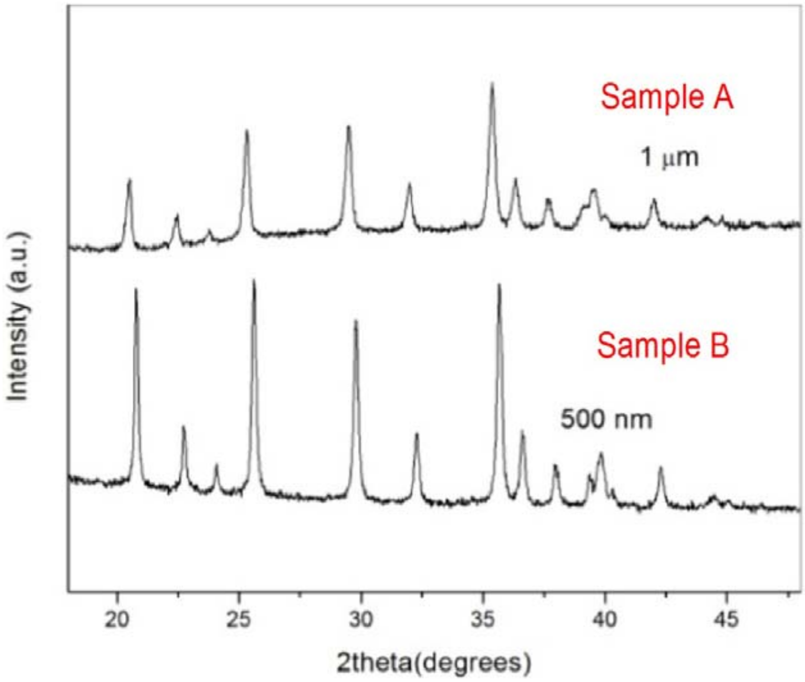

Figure 4.2. X-ray diffraction patterns of two $LiFePO_4$ samples.

A three-electrode pouch cell consisting of a $LiFePO_4$ cathode, a Li foil anode, a Li wire reference electrode, polypropylene (PP) micro-porous film separators and 1.0 M

$LiPF_6$ in EC-DEC-DMC-EMC (1:1:1:3 by volume) liquid electrolyte (Ferro Corporation) was used for electrochemical measurements. The $LiFePO_4$ electrodes were prepared by using the slurry coating method. $LiFePO_4$ active materials were mixed with 10 wt% carbon black and 8 wt% polyvinylidene fluoride (PVDF) in 1-methyl-2-pyrrolidinone (NMP) solvent to form a viscous paste, which was then mixed for 45 minutes using a planetary ball milling machine. The paste obtained was then coated onto carbon-coated aluminum foil and dried in a vacuum oven at 120 °C overnight. After the foil cooled to room temperature, 2 cm×2 cm electrodes with active material loading of 2 mg/cm^2 were cut out. GITT and PITT tests were performed on the three-electrode pouch cells after the $LiFePO_4$ electrodes were fully charged and discharged between 4.2 V and 2.5 V for two cycles. GITT measurements consisting of a series of current pulses were applied to the three-electrode pouch cell at a low current of less than 0.05*C*, each followed by a 16 h relaxation period. The relaxation time of 16 h was selected to allow full relaxation of OCP (open-circuit-potential), which requires more than >10 h for 100 nm $LiFePO_4$ and to minimize the self-discharge of $LiFePO_4$ during the test [7]. The potentials of 2.2 V and 4.2 V were used as low and high cutoff voltages in GITT. In PITT test, a series of potential steps of 20 mV were applied to the $LiFePO_4$ electrodes in three-electrode pouch cells within a potential range of 4.1 V to 3.5 V until the current was less than 0.01*C*. To increase accuracy in the two-phase region, a smaller potential step of 4 mV was used in the phase transformation range (3.5 V~3.412 V).

4.2. Application of Mixed-Control Model Integrated GITT to $LiFePO_4$

Recent research has shown the diffusion of Li-ion is highly anisotropic in $LiFePO_4$ single crystal, which causes Li-ion to diffuse mainly in the one-dimensional channel parallel to the *b*-direction (space group *pnma*) of the orthorhombic $LiFePO_4$ crystal [8]. Moreover, electron microscopy [9] and high-resolution electron energy loss spectroscopy (HREELS) [10] studies of chemically delithiated $LiFePO_4$ crystallites showed that the phase boundary separating the α and β phases was parallel to the *bc* plan (perpendicular to the *a*-axis), which demonstrated Li-ion diffuse through the phase boundary between $FePO_4$ and $LiFePO_4$ with negligible transfer occurring in either the $FePO_4$ or $LiFePO_4$ phase (mechanism I in Figure 4.3a). The phase transformation kinetics in $LiFePO_4$ single particle was investigated by Singh *et al.* based on mechanism I with consideration of the anisotropic lithiation and surface reaction limited dynamics [11]. However, if multiple nano-$LiFePO_4$ crystals agglomerate to form a dense primary $LiFePO_4$ particle (SEM pictures in Figure 4.1), Li-ion insertion/extraction into these aggregated particles at agglomerate scale can still be approximately described by using mechanism II where the phase boundary between α and β phase parallel to the *ac* plane (perpendicular to the *b*-axis, Figure 4.3b) although the Li-ion insertion into individual crystal follows the mechanism I [9, 12]. Mechanism II has been suggested by Chen *et al.* in phase decomposition of $LiFePO_4$, although it has a higher energy than mechanism I [13]. In mechanism I, the phase boundary moves orthogonally to the direction of the surface flux indicates that diffusion path does not change with state of discharge (SOD) or state of charge (SOC). However, in mechanism II, the Li-ion diffusion length increases with phase transformation (growth of β phase). To check if the Li-ion insertion into aggregated $LiFePO_4$ particles (Figure 4.1) can be approximately described by mechanism II, the variation of diffusion overpotential with SOD and SOC of agglomerated $LiFePO_4$ was measured by using GITT as shown in Figure 4.4. It is clear that discharge and charge overpotentials of both $LiFePO_4$ samples increased with SOD and SOC, which means the diffusion length was becoming longer, and our mixed-control model (developed based on mechanism II) can be used for analyzing the phase transformation process of both $LiFePO_4$ samples with aggregated nanoparticles. Moreover, the path-dependence in the $LiFePO_4$ observed by Srinivasan and Newman *et al.* can also be reasonably explained by using mechanism II [14].

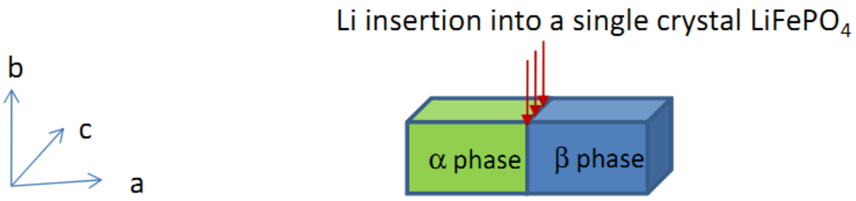

(a) mechanism I

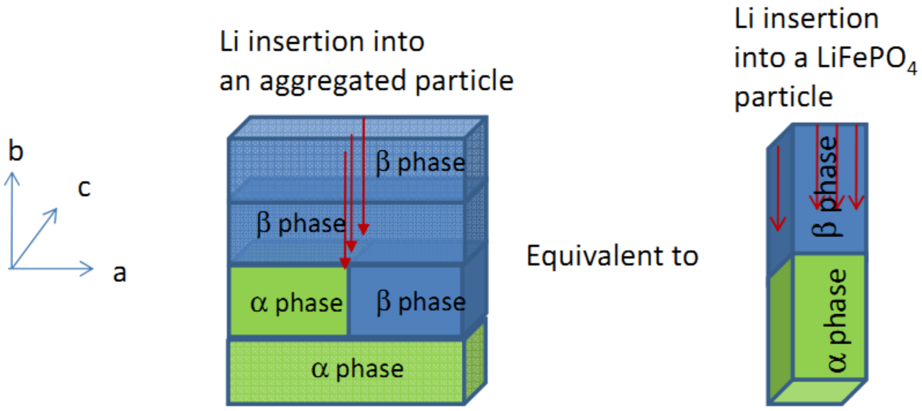

(b) mechanism II

Figure 4.3. Schematic illustration of lithium intercalation in $LiFePO_4$ at different scales.

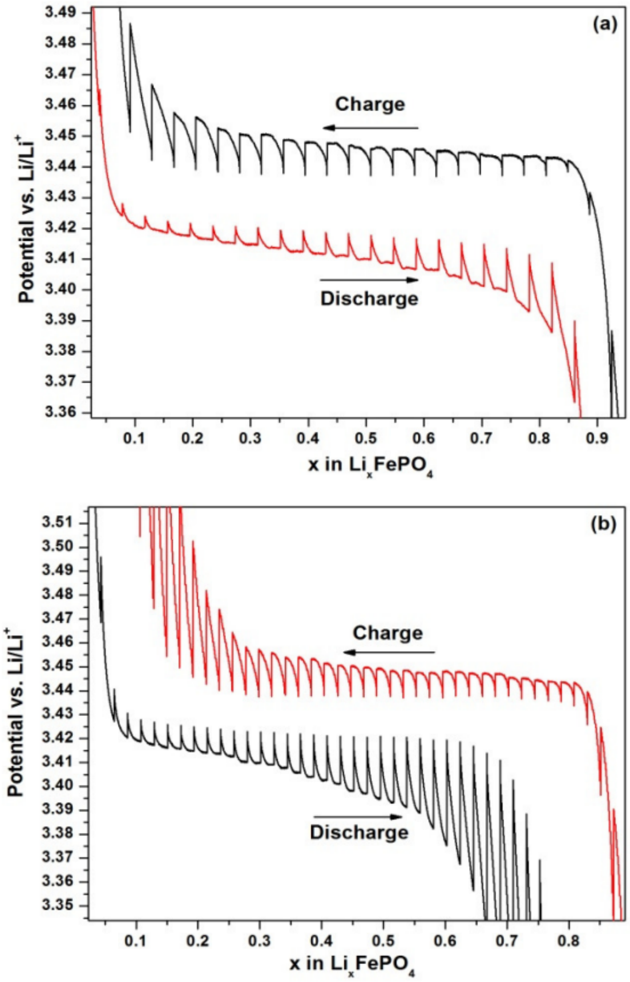

Figure 4.4. Charge/discharge GITT curves for (a) sample A, and (b) sample B.

To reduce the complexity of the problem, we assume that all the diffusion channels of single crystallite particles are arranged in the same direction for $LiFePO_4$ in this study, which reduces the 3D diffusion problem into 1D in agglomerate scale.

4.2.1. Parameters Determination

Most parameters in the mixed-control model can be obtained from the plot of charge/discharge equilibrium potential vs. Li-ion composition, which can be measured by using GITT. Figure 4.5 shows the equilibrium potential vs. Li-ion composition during charge and discharge obtained by using GITT for sample A.

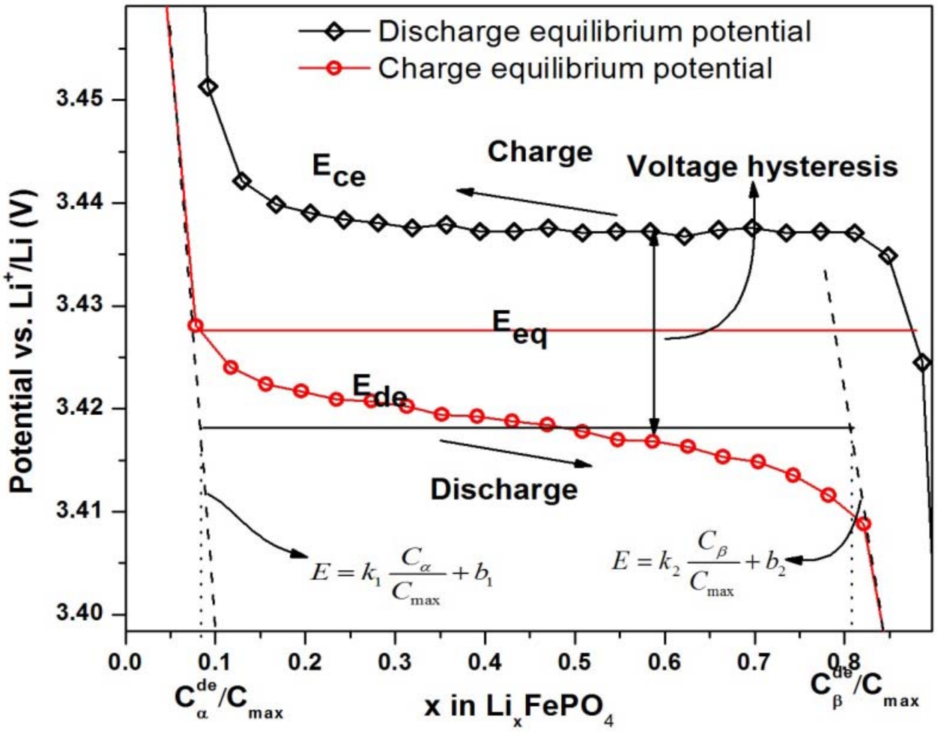

Figure 4.5. Equilibrium potential vs. Li-ion composition of sample A obtained using GITT.

Similar to the results shown in Chapter 3, a potential hysteresis presents between the discharge and charge equilibrium potentials. The theoretical (*strain-free*) equilibrium potential (E_{eq}) is approximately estimated by averaging the discharge equilibrium potential (E_{de}) and charge equilibrium potential (E_{ce}). The expression between Li-ion concentration and the OCP can be obtained from the linear fitting according to Eqs. (2.26) and (2.27).

The discharge accommodation energies (dots) calculated from Eq. (2.14) for sample A and B were plotted vs. Li-ion concentration x in Li$_x$FePO$_4$ in Figure 4.6. The sample B with small second particle size (< 40 nm) had lower accommodation energy than sample A with large second particle size (> 100 nm). The reduced accommodation energy of sample B is attributed to the shrinking of Li-ion miscibility gap with decreasing particle size [15]. To solve the ODEs and PDEs in the mixed-control model, the measured accommodation energy at different Li-ion insertion levels in Figure 4.6 was fitted using a 3^{rd} order polynomial function (dashed lines in Figure 4.6). Table 4.1 lists all the parameters used for solving the mixed-control model.

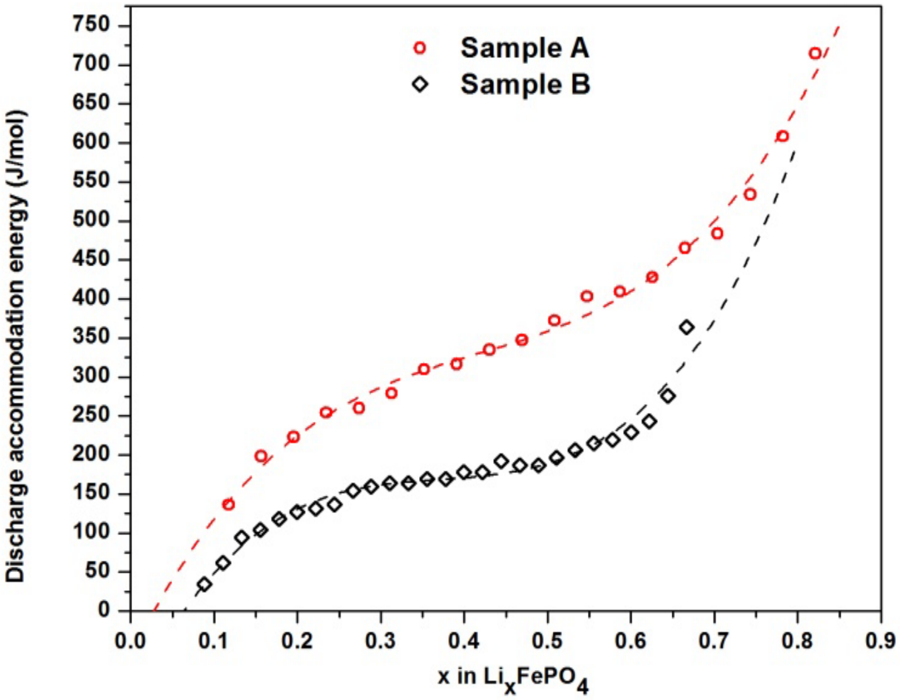

Figure 4.6. Discharge accommodation energy for sample A and B (experiment data: dots; simulated data: dashed line).

4.2.2. Solution Procedure

As mentioned in Chapter 2, Landau transformation is first applied to change the Stefan problem to fixed boundary problem. Then, the equations are converted to dimensionless form and solved with the numerical method of lines (MOL) approach. In the MOL approach, the partial differential equations are discretized over spatial variable to convert into a system of differential-algebraic equations (DAEs). The DAEs are numerically solved by Maple software with a built-in program (see

Appendix A for detailed solving procedure). By numerically solving the equations, we can obtain the Li-ion concentration profiles during discharge process.

Table 4.1. Parameters used for GITT and PITT simulations.

Parameters	Sample A	Sample B
Particle size (*nm*)	1000	500
Second particle size (*nm*)	40	100
Density of $FePO_4$ particle (ρ) (g/cm^3)	3.6	3.6
Molar volume of $LiFePO_4$(cm^3/mol)	46	46
$C_{\max}$ (mol/cm^3)	0.02119	0.02119
Current density for GITT (*A/g*)	0.0060	0.00350
Strain-free equilibrium potential E_{eq} (*V*)	3.4276	3.4292
$\Delta G_{accom} = f(x_i)$ (*J/mol*)	$f(x_i) = 690.15 - 1429.50x_i$ $+2095.80x_i^2 - 1215.93x_i^3$	$f(x_i) = 321.89 - 811.45x_i$ $+1500.93x_i^2 - 976.51x_i^3$
k_1	-12.03	-5.99
b_1	3.94	3.68
k_2	-4.80	-3.42
b_2	7.57	6.04

4.2.3. Li-Ion Diffusivity Obtained Using Mixed-Control Model Integrated GITT

By solving the mixed-control model numerically at different initial conditions, we can obtain discharge curves at different SODs. We fit the experiment results with simulated curves by changing parameters (D_α, D_β and M) in the mixed-control model. Figure 4.7 shows typical discharge GITT curves of sample A at 10%, 30%, 60% and 90% of SODs, and the simulated data by using mixed-control model integrated GITT at corresponding SODs. In Figure 4.7, the simulated discharge curves agree well with the experimental data, with deviation less than 2 mv.

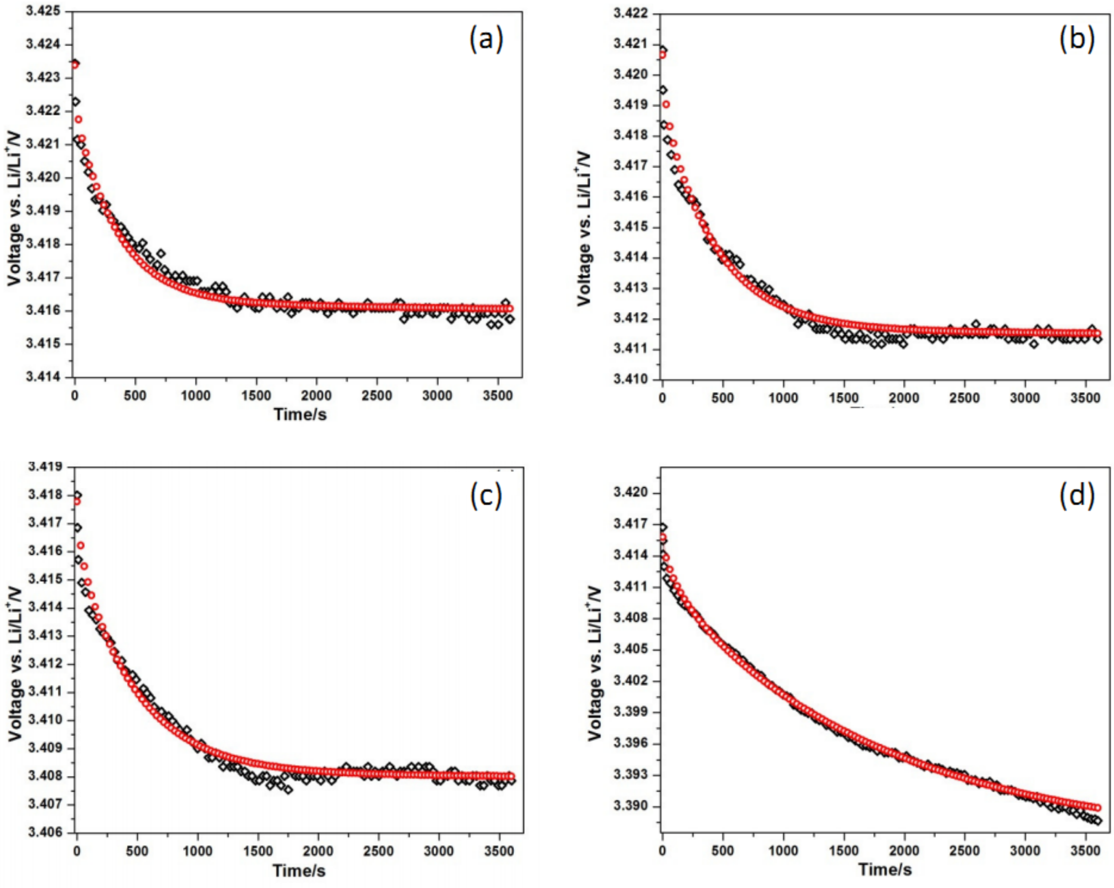

Figure 4.7. Experimental and simulated data of sample A at different SODs (a) 10%; (b) 30%; (c) 60%; (d) 90%. (Black diamond: experimental data; red circle: simulated data).

The D_α and D_β values obtained by fitting the GITT discharge curves in the two-phase region at different SODs were plotted vs. Li-ion concentration x in Li_xFePO_4 as shown in Figure 4.8. For comparison, the apparent diffusion coefficients calculated by using traditional analysis method (Eq. (1.1)) in both the single and two-phase regions are also shown in Figure 4.8. As reported by other groups [16], the diffusion coefficients in two-phase region obtained by using traditional GITT analysis methods are 3 orders of magnitude lower than those in single phase region. This result is unreasonable because the composition and structure of the α phase before and after β phase deposition is almost the same; therefore, the Li-ion diffusion coefficient in the

α phase should be similar to that during phase formation. The reduced diffusion coefficient in the two-phase region calculated by using traditional GITT is induced by a nearly zero gradient of equilibrium potential ($\frac{dE(x)}{dx}$ in Eq. (1.1)) in the two-phase region. Theoretically, the gradient of equilibrium potential of $LiFePO_4$ in the two-phase region should be zero, and the gradient of equilibrium potential in the two-phase region is induced by the strain accommodation energy or particle size distribution. On the basis of traditional GITT, the diffusion coefficient of phase transformation electrode materials in the two-phase region will increase with accommodation energy, which is unreasonable. The diffusion coefficients in the α and β phases in the two-phase region determined by using mixed-control model integrated GITT are similar to the values in single phase regions calculated from Eq. (1.1) by using traditional GITT. Since the diffusion coefficient in single phase regions obtained by using traditional GITT is reliable, the similarity between diffusion coefficients in the single phase and two-phase region validated the mixed-control model. The diffusion coefficient of the α is about 10^{-12} cm^2 s^{-1}, which is 5-10 times higher than the diffusion coefficient in the β phase. The enhanced diffusion coefficient in the α phase agrees with theoretical predictions [8]. In Figure 4.8, the diffusion coefficient in the β phase decreases slightly with Li-ion insertion, which may be attributed to gradually increased accommodation energy during the α to β phase transformation (Figure 4.6). Using traditional GITT (Eq. (1.1)), we can only obtain one apparent diffusivity of α+ β composite in the two-phase region without any information about Li-ion diffusivity in either the α or β phase. However, by using the mixed-control model, we obtained Li-ion diffusivity in both the α and β phases in the two-phase region.

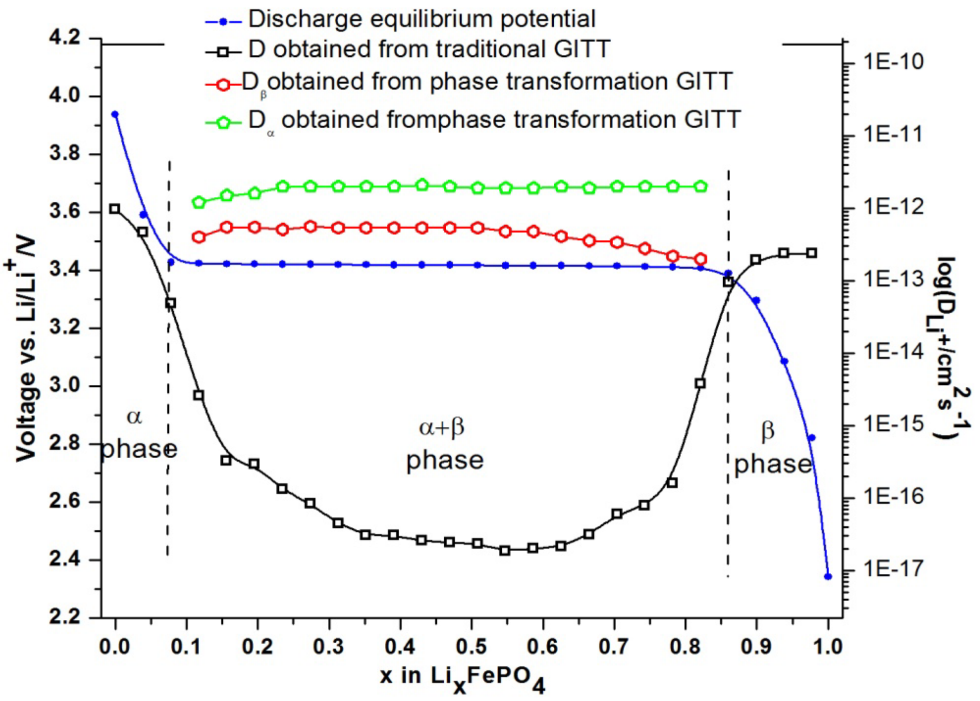

Figure 4.8. Li-ion diffusion coefficients of sample A at different Li-ion insertion levels obtained by using traditional discharge GITT and phase transformation (mixed-control model integrated) discharge GITT. The phase region is marked based on the discharge equilibrium-composition curve.

Figure 4.9 shows the experimental data and well-fitted values for sample B at different SOD. The obtained diffusion coefficients from fitting the experimental data to the model are shown in Figure 4.10. The diffusion coefficient calculated by using traditional GITT analysis method (Eq. (1.1)) is also shown in Figure 4.10 for comparison. The diffusion coefficient in sample B is similar to the value in sample A. Therefore, the diffusion coefficient seems not to be affected by the size of the secondary particle. As for sample A, the diffusion coefficients of sample B in the α and β phases in the two-phase region determined by using mixed-control model are similar to the values in single-phase regions calculated from traditional GITT. The diffusion coefficients of the two $LiFePO_4$ samples obtained using traditional GITT are in the same range as results from other researchers (Table 4.2), indicating that the parameters obtained through GITT are reliable.

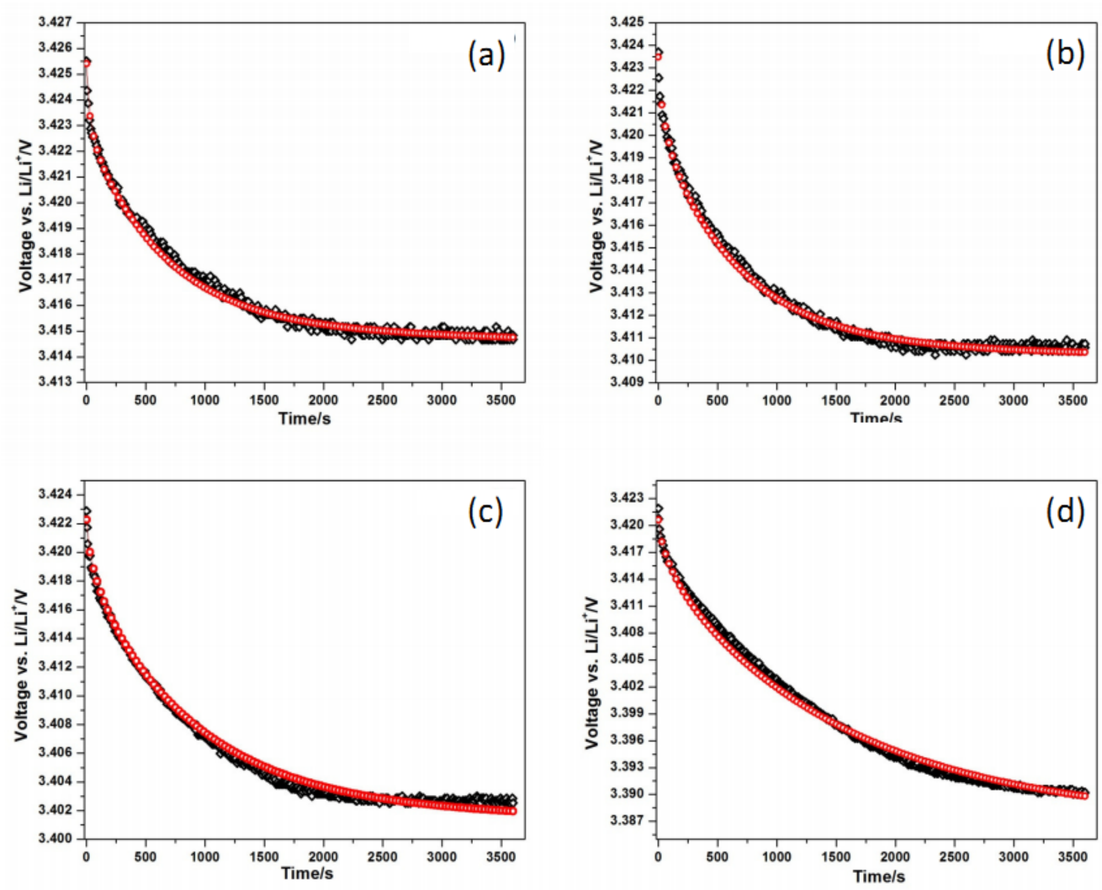

Figure 4.9. Experimental and simulated data of sample B at different SODs (a) 10%; (b) 30%; (c) 60%; (d) 90%. (Black diamond: experimental data; red circle: simulated data).

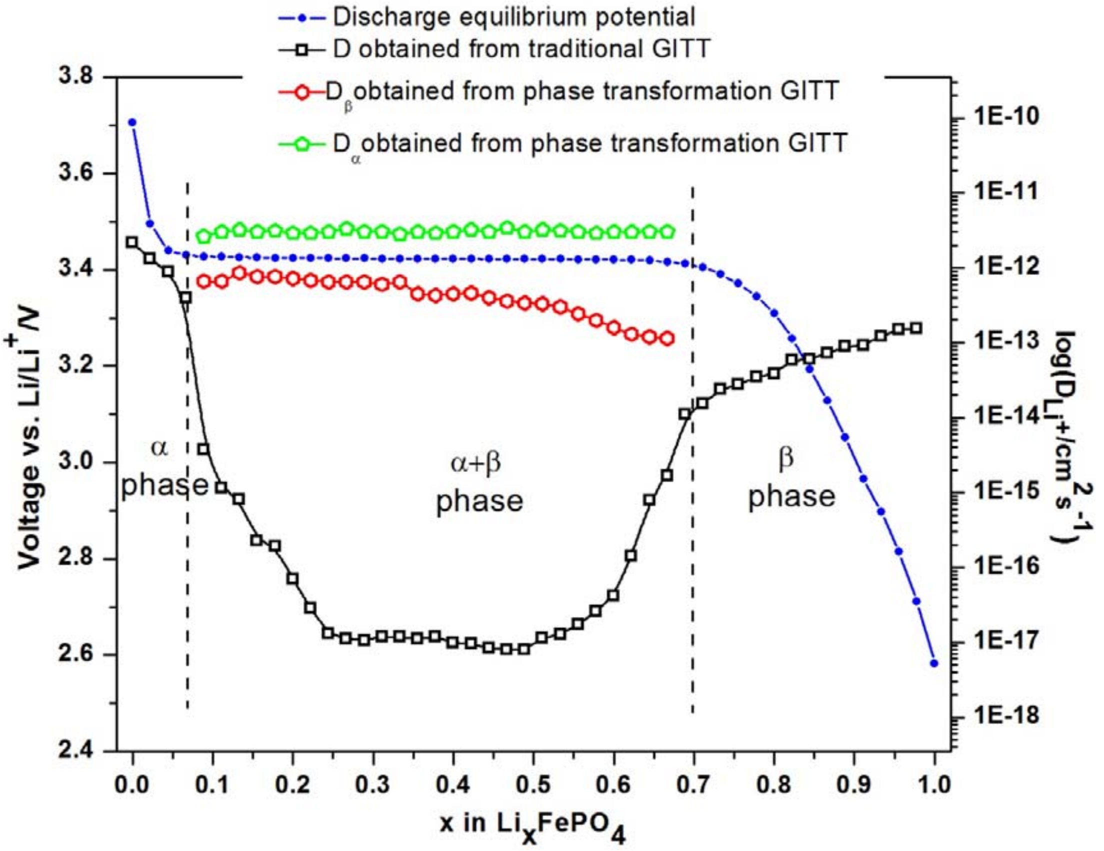

Figure 4.10. Li-ion diffusion coefficients of sample B at different Li-ion insertion levels obtained by using traditional discharge GITT and phase transformation discharge GITT. The phase region is marked based on the discharge equilibrium-composition curve.

Table 4.2. Comparison of Li ion diffusion coefficient of LiFePO$_4$ obtained using different methods.

Technology	D_{Li^+} in one phase region/cm^{2}s^{-1}	D_{Li^+} in two phase region / cm^{2}s^{-1}	Ref.
GITT, EIS	10^{-15}~10^{-14}	10^{-17}~10^{-16}	[16]
PITT	10^{-14}~10^{-12}	10^{-13}	[17]
EIS	10^{-13}	10^{-15}~10^{-14}	[17]
CITT	10^{-15}~10^{-14}	10^{-16}~10^{-15}	[18]
GITT/PITT	10^{-14}~10^{-12}	10^{-18}~10^{-15}	Present work
Mixed-control model integrated GITT/PITT		10^{-14}~10^{-12}	Present work

4.2.4. Li-Ion Diffusivity Cross-Checked by Mixed-Control Model Integrated PITT

To further validate the mixed-control model, the diffusion coefficient of the two $LiFePO_4$ samples was also crosschecked by using the traditional PITT method (Eq. (1.2)) and mixed-control model integrated PITT. In the PITT measurement, potential steps of 20 mV in the single phase region (3.00-3.41 V) and 4 mV in the two-phase region (3.43-3.41 V) were used. Since the potential range in the two-phase region is very narrow (less than 20 mV), only a few data points were obtained in the two-phase region. Two typical simulated current density versus time curves for sample B by using mixed-control model integrated PITT were compared with experimentally measured current density at different voltages in the two-phase region (Figure 4.11). The D_α and D_β obtained from mixed-control model integrated PITT are plotted versus the voltage in Figure 4.12. Similar to traditional GITT, the diffusion coefficient calculated by using traditional PITT in the two-phase region was also lower than that in the single-phase region, while the diffusion coefficient (marked in Figure 4.12) obtained in the two-phase region using mixed-control model integrated PITT is similar to the value in the single phase region obtained by traditional PITT. D_α and D_β in the two-phase region obtained by using mixed-control model integrated PITT are similar to the value obtained from mixed-control model integrated GITT and in correspondence to the values in the single-phase region measured by using traditional PITT, demonstrating the reliability of mixed-control model.

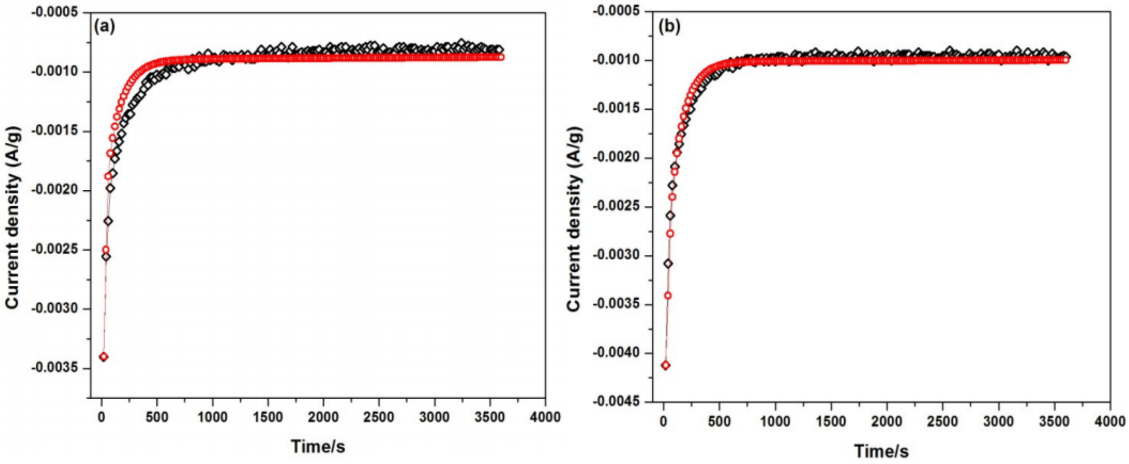

Figure 4.11. Comparing experimental data and simulated data in PITT for sample B, (a) voltage decreases from 3.424V to 3.420V; (b) voltage decreases from 3.422V to 3.416V**.**

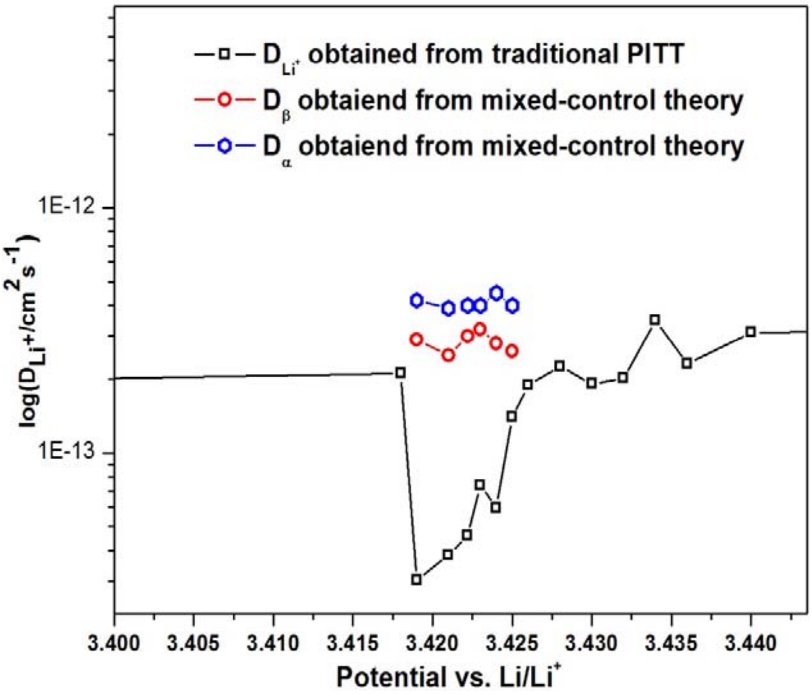

Figure 4.12. Li ion diffusion coefficient calculated from traditional PITT and mixed-control model integrated PITT for sample B.

4.2.5. Interface Mobility Obtained from Mixed-Control Model Integrated GITT and PITT

In addition to the diffusion coefficient, the interface mobility *M* of the phase transformation electrode materials can also be obtained by using mixed-control model. The interface mobility values of two $LiFePO_4$ samples at different SOD are obtained by using mixed-control model integrated GITT and PITT and shown in Figure 4.13.

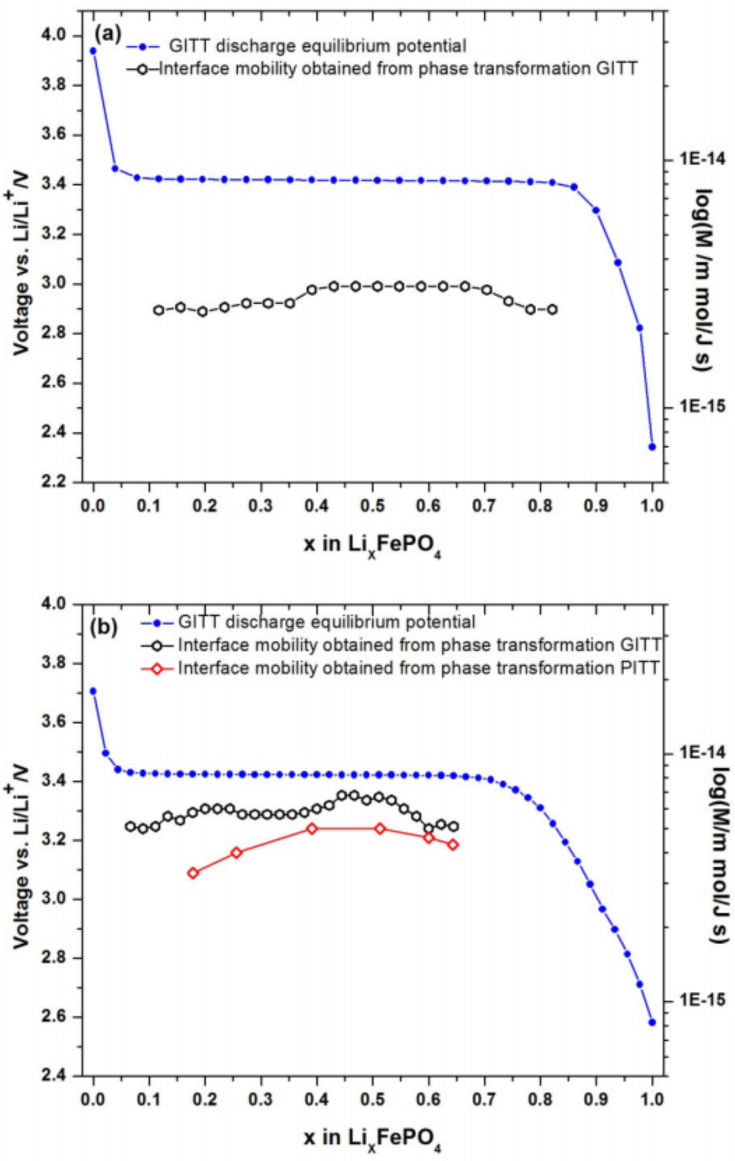

Figure 4.13. Interface mobility of sample A and B obtained from mixed-control model integrated GITT.

In Figure 4.13, the interface mobility M is about 10^{-15} m mol J^{-1} s^{-1} for both samples. The average value of M (5.7×10^{-15} m mol J^{-1} s^{-1}) for sample B with small secondary particles is two times higher than that of sample A (2.75×10^{-15} m mol J^{-1} s^{-1}) with large secondary particles. Since the interface mobility depends on interface coherence, strain/stress and deformations of the materials [19], the high interface mobility of sample B may be attributed to the coherent interface and low accommodation energy for $LiFePO_4$ with small secondary particles. Sample B consisting of 40 nm secondary particles has a narrow miscibility gap (Figure 4.4), which decreases the lattice mismatch, as demonstrated by the low accommodation energy in Figure 4.6. The low lattice strain can potentially form a coherent phase boundary between Li_xFePO_4 and $Li_{1-y}PO_4$ [1], and the coherent interface causes high cooperative phase boundary movement upon electrochemical reaction with minimal formation of dislocations or cracks [1]. The high interface mobility for small size $LiFePO_4$ is in agreement with the reported results that the rate performance of $LiFePO_4$ increases with decreases in particle size [1].

The interface mobility is usually temperature-dependent, which can be expressed as [20]

$$M = M_0 \exp\left(-\frac{Q_M}{RT} \right) \tag{4.1}$$

where M_0 is the pre-exponential factor, which depends on temperature and the average atomic spacing in two phases and Q_M is the activation energy for interface movement [20], which is determined by the coherent/incoherent character of the interface between the two phases. Santofimia *et al.* [21] calculated the interface mobility of the martensite-austenite phase transformation. Their results showed that, at the annealing temperature of 350 °C, if the interface is coherent, the interface mobility is 2.45×10^{-20} m^4 J^{-1} s^{-1} (corresponding to 3.5×10^{-15} m mol J^{-1} s^{-1}). The interface mobilities of the two $LiFePO_4$ samples studied in this Chapter are on the order of 10^{-15} m mol J^{-1} s^{-1} at room temperature, which are similar to the interface mobility of the martensite-austenite phase transformation with a coherent interface at 350 °C.

4.3. Summary

The mixed-control phase transformation model, developed in Chapter 2, is integrated into GITT and PITT methods. The mixed-control model integrated GITT and PITT are able to determine the ion diffusion coefficient and interface mobility of phase transformation electrode materials at two-phase regions. Applying the mixed-control model integrated GITT on two agglomerated $LiFePO_4$ electrodes with different secondary particle size, the effect of crystal size of $LiFePO_4$ on accommodation energy, diffusion coefficient, and interface mobility is investigated during discharge. The diffusion coefficient (10^{-11}~10^{-12} cm^2 s^{-1}) in α phase is 5-10 times higher than that in β phase in two-phase region, and the diffusion coefficient in β phase slightly decreases with increasing SOD probably due to the increase in accommodation energy. The diffusion coefficients in α phase and β phase in two-phase region are similar to the values in single α and single β regions. This contradicts all reported results that the diffusion coefficient in two phase region is 2-3 orders of magnitude lower than that in the single phase region calculated by using traditional GITT.

The accommodation energy and interface mobility of $LiFePO_4$ are found to be size-dependent. $LiFePO_4$ with 40 nm crystal size has a lower accommodation energy and higher interface mobility when compared to those for $LiFePO_4$ with a 100 nm crystal size. The interface mobility (10^{-15} m mol J^{-1} s^{-1}) of $LiFePO_4$ at room temperature is comparable to the values for the martensite-austenite transformation in a Fe-C alloy with a semi-coherent interface at 350 ^{o}C. The mixed-control model can be applied to any ion insertion phase transformation electrode materials such as $LiMnPO_4$, $Li_4Ti_5O_{12}$, and graphite for Li-ion batteries and metal-hydride materials for Ni/MH batteries.

4.4. References

1. N. Meethong, H. -Y. S. Huang, S. A. Speakman, W. C. Carter, and Y. M. Chiang, Strain accommodation during phase transformations in olivine-based cathodes as a materials selection criterion for high-power rechargeable batteries. *Adv. Funct. Mater.* **17**, 1115-1123 (2007).
2. N. Meethong, H-Y. S. Huang, S. A. Speekman, W. C. Carter, and Y-M. Chiang, Size-dependent lithium miscibility gap in nanoscale $Li_{1-x}FePO_4$. *Electrochem. Solid-State Lett.* **10**, A134-A138 (2007).
3. P. Subramanya Herle, B. Ellis, N. Coombs, and L. F. Nazar, Nano-network electronic conduction in iron and nickel olivine phosphates. *Nat. Mater.* **3,** 147-152 (2004).
4. C. Wang and J. Hong, Ionic/electronic conducting characteristics of $LiFePO_4$ cathode materials. *Electrochem. Solid-state Lett.* **10**, A65-A69 (2007).
5. A. Funabiki, M. Inaba, T. Abe, and Z. Ogumi, Stage transformation of lithium-graphite intercalation compounds caused by electrochemical lithium intercalation. *J. Electrochem. Soc.* **146**, 2443-2448 (1999).

6. G. Kobayashi, S. I. Nishimura, M. S. Park, R. Kanno, M. Yashima, T. Ida, and A. Yamada, Isolation of solid solution phases in size-controlled Li_xFePO_4 at room temperature. *Adv. Funct. Mater.* **19**, 395-403 (2009).
7. N. Meethong, Y. H. Kao, M. Tang, H. Y. Huang, W. C. Carter, and Y. M. Chiang, Electrochemically induced phase transformation in nanoscale olivines $Li_{1-x}MPO_4$ (M=Fe, Mn). *Chem. Mater.* **20**, 6189-6198 (2008).
8. D. Morgan, A. V. D. Ven, and G. Ceder*,* Li conductivity in Li_xMPO_4 (M=Mn, Fe, Co, Ni) olivine materials. *Electrochem. Solid-state Lett.* **7**, A30-A32 (2004).
9. G. Chen, X. Song, and T. J. Richardson, Electron microscopy study of the $LiFePO_4$ to $FePO_4$ phase transition. *Electrochem. Solid-state Lett.* **9**, A295-A298 (2006).
10. L. Laffont, *et al.* Study of the $LiFePO_4/FePO_4$ two-phase system by high-resolution electron energy loss spectroscopy. *Chem. Mater.* **18**, 5520-5529 (2006).
11. G. K. Singh, G. Ceder, and M. Z. Bazant, Intercalation dynamics in rechargeable battery materials: General theory and phase-transformation waves in $LiFePO_4$. *Electrochimica Acta* **53**, 7599-7613 (2008).
12. C. Delmas, M. Maccario, L. Croguennec, F. L. Cras, and F. Well, Lithium deintercalation in $LiFePO_4$ nanoparticles via a domino-cascade model. *Nat. Mater.* **7**, 665-671 (2008).
13. G. Chen, X. Song, and T. J. Richardson, Metastable solid-solution phases in the $LiFePO_4/FePO_4$ system. *J. Electrochem. Soc.* **154**, A627-A632 (2007).

14. V. Srinivasan and J. Newman, Existence of path-dependence in the $LiFePO_4$ electrode. *Electrochem. Solid-state Lett.* **9**, A110-A114 (2006).

15. D. Burch and M. Z. Bazant, Size-dependent spinodal and miscibility gaps for intercalation in nanoparticles. *Nano Lett.* **9**, 3795-3800 (2009).

16. P. P. Prosini, M. Lisi, D. Zane, and M. Pasquali, Determination of the chemical diffusion coefficient of lithium in $LiFePO_4$. *Solid State Ionics* **148**, 45-51 (2002).

17. J. Xie, N. Imanishi, T. Zhang, A. Hirano, Y. Takeda, and O. Yamamoto, Li-ion diffusion kinetics in $LiFePO_4$ thin film prepared by radio frequency magnetron sputtering. *Electrochimica Acta* **54**, 4631-4637 (2009).

18. X-C. Tang, L-X. Li, Q-L. Lai, X-W. Song, and L-H. Jiang, Investigation on diffusion behavior of Li^+ in $LiFePO_4$ by capacity intermittent titration technique (CITT). *Electrochimica Acta* **54**, 2329-2334 (2009).

19. D. A. Porter and K. E. Easterling, *Phase Transformations in Metals and Alloys*, second edition, Chapman & Hall, London, **1992**.

20. R. G. Thiessen, I. M. Richardson, J. Sietsma, Physically based modeling of phase transformations during welding of low-carbon steel. *J. Mater. Sci. Eng.* **A427**, 223-231 (2006).

21. M. J. Santofimia, L. Zhao, and J. Sietsma, Model for the interaction between interface migration and carbon diffusion during annealing of martensite-austenite microstructure in steels. *J. Scr. Mater.* **59**, 159-162 (2008).

Chapter 5: Cyclic Voltammetry for Phase Transformation Electrode Materials

Recently, CV has been extensively used to study phase transformation electrode materials as a complementary method for constant current charge/discharge tests [1-10]. Like GITT, PITT, and EIS, the analysis method of CV data is also based on Fick's diffusion law without consideration of phase transformation. Thus, there is controversy surrounding the application of CV to phase transformation electrode materials. For example, some researchers have found that Li-ion insertion into $LiFePO_4$ is quasi-reversible because peak current varied linearly with scan rates, and the potential separation between cathodic and anodic current peaks varied with scan rates [4, 6], while others reported that the lithiation/delithiation of $LiFePO_4$ is reversible due to an observed linear relationship between the peak current and the square root of scan rate [1, 2, 5]. Also, the apparent Li-ion diffusion coefficient in $LiFePO_4$ obtained from traditional CV scans varied widely from 10^{-15} to 10^{-13} cm^2 s^{-1}. Since recent researchers have demonstrated that phase transformation plays a critical role in the charge/discharge of phase transformation electrode materials [11-13], the above results may come from the effect of phase transformation.

In previous Chapter, we developed a mixed-control phase transformation model and integrated it with GITT and PITT methods. For the first time, the Li-ion diffusion coefficient and interface mobility of two $LiFePO_4$ samples in the two-phase region were obtained by using mixed-control model integrated GITT and PITT. In this Chapter, the mixed-control model is integrated into CV to study the phase transformation electrode materials. In addition to ion diffusion and phase transformation, electrolyte resistance and charge transfer effect are also considered in the mixed-control model integrated CV. In this study, the Li-ion diffusion coefficient and interface mobility of $LiFePO_4$ are obtained by fitting the experimentally measured CV data with simulation results obtained from the mixed-control model. These parameters are compared with the values calculated from traditional CV. Also, the effect of phase transformation, ion diffusion coefficient, particle size, electrolyte resistance, and charge transfer resistance on the CV profiles is analyzed with the mixed-control model integrated CV, and the results are compared with the experimental CV curves of $LiFePO_4$ and $LiMnPO_4$ and the reported results in literatures.

5.1. Experiments

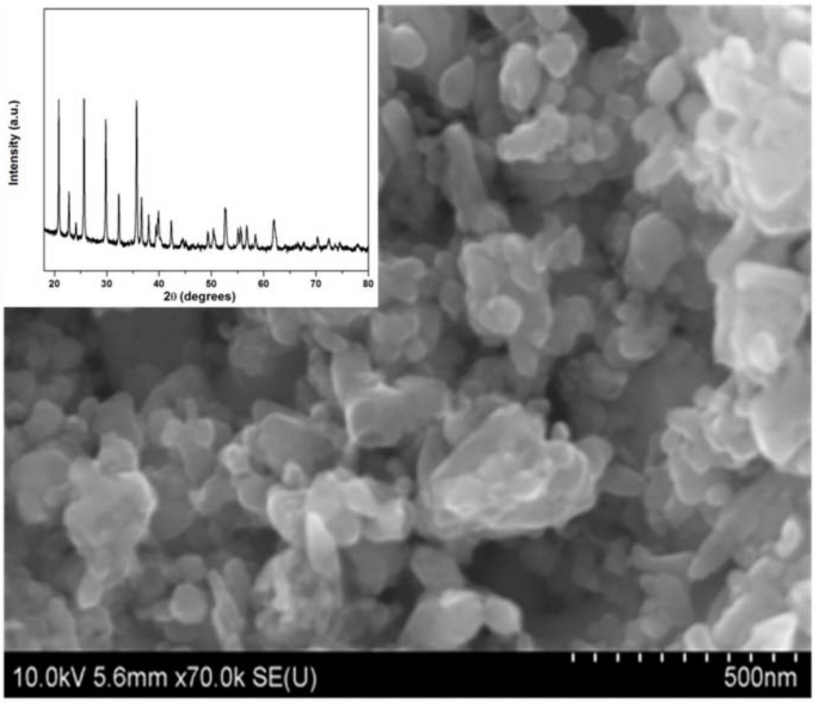

Figure 5.1. SEM image of the $LiFePO_4$ sample with the inset showing the XRD pattern.

The carbon-coated $LiFePO_4$ powder was purchased from a commercial supplier. As shown in the SEM picture in Figure 5.1, the $LiFePO_4$ sample mainly consists of aggregations of small particles (300 nm) with a secondary particle size around 50 nm. The X-ray diffraction (XRD) pattern of the $LiFePO_4$ sample, shown as the inset in Figure 5.1, demonstrates that the $LiFePO_4$ sample is in a crystalline single phase. The $LiMnPO_4$ sample, provided by Prof. Manthiram at University of Texas, Austin, shows a particle size similar to the $LiFePO_4$ sample.

Three-electrode pouch cells each consisting of a working cathode, a Li foil anode, a Li wire reference electrode, polypropylene (PP) micro-porous film separators, and 1.0 M $LiPF_6$ in EC-DEC-DMC-EMC (1:1:1:3 by volume) liquid electrolyte (Ferro Corporation) were used for electrochemical measurements. The cathodes were prepared by using the slurry coating method. The active materials were mixed with 10 wt% carbon black and 8 wt% polyvinylidene fluoride (PVDF) in 1-methyl-2-pyrrolidinone (NMP) solvent to form a viscous paste, which was then mixed for 45 minutes with a planetary ball milling machine. The obtained paste was then coated onto carbon-coated aluminum foil and dried in a vacuum oven at 120 °C for overnight. After the foil cooled down to room temperature, 2 cm×2 cm electrodes with active material loadings of 2 mg/cm^2 were cut out as cathodes for pouch cell assembly.

Before any electrochemical tests, the electrode was activated with five charge/discharge cycles from 2.2 to 4.2 V with a 0.1*C* current. To obtain the equilibrium potential-composition isotherm, the GITT tests were performed using *Arbin* instrumentation by repeatedly applying a current (less than 0.05C) for 1 h and then resting for 16 h. Potentials of 4.2 and 2.2 V were used as high and low cutoff potentials in the GITT tests. For the CV measurements, the pouch cells were charged/discharged at different scan rates, ranging from 0.01 mV/s to 1 mV/s, from potentials of 2.5 to 4.2 V. Before each CV test, the electrode was discharged to 2.5 V using 0.1*C* current and held at 2.5 V for 2 h. Electrochemical impedance spectroscopy (EIS), with frequency ranging from 10^{-3} to 10^{6} Hz and 10 mV potential amplitude, was used to measure the exchange current density of cathodes at different discharge/charge states. The EIS measurement was performed after the electrode was charged or discharged to desired state of charge (SOC) or state of discharge (SOD) and then rest for 2 h. Both CV and EIS were performed by using *Solartron* 1287/1260.

5.2. Development of Mixed-Control Model Integrated Cyclic Voltammetry

The mixed-control phase transformation model is integrated into CV with the consideration of both charge transfer resistance and electrode resistance (including electrolyte resistance and solid electrolyte interphase (SEI) resistance, etc.). Before and after the phase transformation, $LiFePO_4$ is a solid solution material, and the movement of Li-ion inside the material can be described with Fick's diffusion law with the corresponding boundary conditions. When phase transformation happens, the movement of Li-ion in the two-phase region also follows Fick's diffusion law with a sharp phase boundary separating the two phases. Under mixed-control phase transformation model, the corresponding initial and boundary conditions for CV for one dimensional charge/discharge process (assuming slab geometry) are listed below.

If we start from fully charged state (α phase), the control equations for discharge process can be described as

single α phase region

$$\frac{\partial C_\alpha}{\partial t} = D_\alpha \left(\frac{\partial^2 C_\alpha}{\partial x^2} \right) \tag{5.1}$$

t=0 for $0 \le x \le L$, $C_\alpha = C_\alpha^0$ (5.2)

$t \ge 0$ x=0, $\frac{\partial C_\alpha}{\partial x} = 0$ (5.3)

x=*L*,

$$-\frac{D_\alpha \left(\frac{\partial C_\alpha}{\partial x} \right) F}{\rho L} = i_0 \left[\frac{1 - C_\alpha}{1 - C_\alpha^e} \exp\left(-\frac{\gamma F}{RT} \left(E_{app} - E_{de} - I(t) R_e \right) \right) - \frac{C_\alpha}{C_\alpha^e} \exp\left(\frac{(1-\gamma) F}{RT} \left(E_{app} - E_{de} - I(t) R_e \right) \right) \right] \tag{5.4}$$

In above equations, C_α is the Li-ion concentration in α phase, Eq. (5.2) expresses the initial condition of the Li-ion concentration, L is the characteristic length of $LiFePO_4$ slab, and C_α^0 is the initial concentration of Li-ion in α phase. Eq. (5.3) is corresponding to the symmetry condition at the slab center. Eq. (5.4) is based on the assumption that the current due to insertion reaction follows the Butler-Volmer expression [14], in which D_α is the chemical diffusion coefficient of Li-ion in the α phase; ρ is the density of $LiFePO_4$; i_0 is the exchange current density; C_α^e is the equilibrium concentration of Li-ion in the α phase during the discharge process, which is defined as the concentration when no current is passing through the electrode and no Li-ion concentration gradient exists in the material, and it changes along the extension of A-B line in Figure 2.1; E_{de} is the corresponding discharge equilibrium potential of the electrode, which can be obtained from the equilibrium potential-composition isotherm (Figure 2.1); γ is the transfer coefficient, which is a measure of the symmetry of the forward and backward reaction energy barrier for Li-ion insertion reaction [14]; E_{app} is the applied voltage on the electrode; $I(t)$ is the transient current density of the electrode; and R_e is the electrode resistance, which includes the electrolyte resistance R_{ele} and the SEI film resistance R_{SEI}. It is necessary to point out that above parameters E_{app}, E_{de}, C_α^e and $I(t)$ all change with time.

When the Li-ion concentration at the particle surface reaches the solid solubility in the α phase, phase transformation occurs. According to mixed-control phase transformation model, the control equations for the two-phase region are:

β phase

$$\frac{\partial C_\beta}{\partial t} = D_\beta \left(\frac{\partial^2 C_\beta}{\partial x^2} \right) \tag{5.5}$$

t=0 for $x_i(t) \le x \le L$, C_β=$C_{\beta i}$ (5.6)

$t \ge 0$ x=L,

$$-\frac{D_\beta \left(\frac{\partial C_\beta}{\partial x} \right) F}{\rho L} = i_0 \left[\frac{1-C_\beta}{1-C_\beta^e} \exp\left(-\frac{\gamma F}{RT} \left(E_{app} - E_{de} - I(t) R_e \right) \right) - \frac{C_\beta}{C_\beta^e} \exp\left(\frac{(1-\gamma) F}{RT} \left(E_{app} - E_{de} - I(t) R_e \right) \right) \right] \tag{5.7}$$

α phase

$$\frac{\partial C_\alpha}{\partial t} = D_\alpha \left(\frac{\partial^2 C_\alpha}{\partial x^2} \right) \tag{5.8}$$

t=0 for $0 \le x \le x_i(t)$, C_α=$C_{\alpha i}$ (5.9)

$t \ge 0$ x=0, $\frac{\partial C_\alpha}{\partial x} = 0$ (5.10) where C_β is the Li-ion concentration in the β phase, D_β is the chemical diffusion coefficient of Li-ion in the β phase, C_β^e is the equilibrium concentration of Li-ion in β phase during the discharge process, which changes along the extension of D-C line (Figure 2.1), $x_i(t)$ is the position of the phase boundary which separates the α and β phases, $C_{\alpha i}$ is the initial value of the Li-ion concentration profile for the α phase and is the concentration at the termination of the single α phase region, $C_{\beta i}$ is the initial Li-ion concentration profile for the β phase which can be calculated according to the Li-ion concentration relationship between two phases at the phase boundary, and all other symbols have the same meaning as above.

For the mixed-control model integrated GITT and PITT in Chapter 4, by extrapolating the equilibrium potential-composition isotherm at the single-phase regions, we approximately obtained the linear relationships between the equilibrium potential and Li-ion concentration for the α and β phase, respectively. In this Chapter, to obtain the expression more precisely, the relationship between the equilibrium potential and the Li-ion concentration for Li-ion insertion reaction is expressed as the Nernst behavior as:

$$E_{\alpha/\beta}(C_{\alpha/\beta}) = \mathrm{P}_1\text{-}\mathrm{P}_2\ln\left(\frac{C_{\alpha/\beta}}{1-C_{\alpha/\beta}}+\mathrm{P}_3\right) \tag{5.11}$$

where $C_{\alpha/\beta}$ is the Li-ion concentration in either the α or β phase. Since the Nernst equation is expressed as activity not concentration, the parameters P_1, P_2 and P_3 are compensations for the activity coefficients. So, according to mass balance and mixed-control model, at the phase boundary separating α and β phase, the boundary conditions can be written as:

at the interface $x=x_i(t)$,

$$\frac{dx_i(t)}{dt} = \frac{D_\alpha\left(\frac{\partial C_\alpha}{\partial x}\right) - D_\beta\left(\frac{\partial C_\beta}{\partial x}\right)}{(C_\beta - C_\alpha)} \tag{5.12}$$

$$\frac{dx_i(t)}{dt} = M\Delta G_{\alpha\to\beta} \tag{5.13}$$

$$E_\alpha(C_\alpha) = E_\beta(C_\beta) \tag{5.14}$$

where $x_i(t)$ is the position of the phase boundary separating two phases; M (m mol J^{-1} s^{-1}) is the interface mobility and depends on the degree of interface coherence, the buildup of stress, and the deformation in the electrode material [15]; and $\Delta G_{\alpha\to\beta}$ is the total driving force for the phase transformation (from α phase to β phase). Eq. (5.14) comes from the assumption that during the charge/discharge process, the Li-ion in the α phase is equilibrium with the Li-ion in the β phase at the phase boundary, where $E_\alpha(C_\alpha)$ and $E_\beta(C_\beta)$ are the expressions between equilibrium potential and Li-ion concentration for the α and β phase, respectively.

As stated in Chapter 2, the total driving force $\Delta G_{\alpha\to\beta}$ for phase transformation consists of three contributions: chemical driving force $\Delta G^{chem}_{\alpha\to\beta}$, strain accommodation energy $\Delta G^{accom}_{\alpha\to\beta}$ and interface energy $\Delta G^{surface}_{\alpha\to\beta}$.

$$\Delta G_{\alpha\to\beta} = \Delta G^{chem}_{\alpha\to\beta} + \Delta G^{accom}_{\alpha\to\beta} + \Delta G^{surface}_{\alpha\to\beta} \tag{5.15}$$

According to Chapter 2, the chemical driving force can be expressed as:

$$\Delta G^{chem}_{\alpha\to\beta} = u^{\beta}_{FePO_4} - u^{\alpha}_{FePO_4} = \left(\frac{C^i_\beta - C^i_\alpha}{C_t}\right)F\left(E_{eq} - E_\beta\left(C^i_\beta\right)\right) \tag{5.16}$$

where C^i_β and C^i_α are the transient Li-ion concentrations in β and α phases at the phase boundary during the discharge process respectively, C_t is the maximum concentration of Li-ion that can be incorporated into the $FePO_4$ lattice, $E_\beta(C^i_\beta)$ is the transient potential at the phase boundary during discharge process which can be calculated by Eq. (5.11) from C^i_β, and E_{eq} is the theoretical (*strain-free*) equilibrium potential for the two-phase region.

The accommodation energy can be calculated from the following equation:

$$\Delta G^{accom}_{\alpha\to\beta} = F\left(\frac{C^{de}_\beta - C^{de}_\alpha}{C_t}\right)\left(E_{eq} - E_{de}\right) = Ff\left(x_i\right) \tag{5.17}$$

where E_{de} is the discharge equilibrium potential measured from GITT experiments (Figure 2.1), and C^{de}_β and C^{de}_α are the Li-ion concentrations in the β and α phase corresponding to equilibrium potential E_{de}, which can be obtained from the equilibrium potential-composition isotherm (Figure 2.1). $\Delta G^{accom}_{\alpha\to\beta}$ is the function of the phase boundary position $x_i(t)$ (*fraction of transformed volume to total volume*), which can be expressed as $f(x_i(t))$. The above accommodation energy is expressed as *joules per mole of β phase*, and the expression $(\frac{C^{de}_\beta - C^{de}_\alpha}{C_t})$ is the amount of electrons/Li-ion accompanied with the forming of one mole of β phase (i.e. $\Delta n_{\alpha\to\beta}$ in Eq. (2.8)).

So, according to Eqs. (5.15)-(5.17), Eq.(5.13) becomes:

at $x=x_i(t)$

$$\frac{dx_i(t)}{dt} = M\Delta G_{\alpha\to\beta} = MF\left[-\frac{\left(C_\beta^i - C_\alpha^i\right)}{C_t}\left(E_{eq} - E_\beta\left(C_\beta^i\right)\right) + f\left(x_i(t)\right)\right] \tag{5.18}$$

When the phase boundary reaches the center of the particles, the phase transformation is considered to be finished. The electrode material becomes a solid solution again. The main equations for this region are:

single β phase region

$$\frac{\partial C_\beta}{\partial t} = D_\beta\left(\frac{\partial^2 C_\beta}{\partial x^2}\right) \tag{5.19}$$

$$t=0,\ 0 \le x \le L,\ C_\beta = C_{\beta f} \tag{5.20}$$

$$t \ge 0\ \ x=0,\ \frac{\partial C_\beta}{\partial x} = 0 \tag{5.21}$$

$x=L$,

$$-\frac{D_\beta\left(\frac{\partial C_\beta}{\partial x}\right)F}{\rho L} = i_0\left[\frac{1-C_\beta}{1-C_\beta^e}\exp\left(-\frac{\gamma F}{RT}\left(E_{app} - E_{de} - I(t)R_e\right)\right) - \frac{C_\beta}{C_\beta^e}\exp\left(\frac{(1-\gamma)F}{RT}\left(E_{app} - E_{de} - I(t)R_e\right)\right)\right] \tag{5.22}$$

where $C_{\beta f}$ is the initial Li-ion concentration profile for the single β phase region, which is the same as the Li-ion concentration profile at the end of the phase transformation.

Overall, Eqs. (5.1)-(5.10) and Eqs. (5.12)-(5.22) describe the discharge process under the CV test condition, which starts from the fully charged state, goes through the phase transformation region, and finally ends at the fully discharged state. The above equations are also suitable for the charge process. Unlike the discharge process, for the charge process, β phase is inside and α phase is outside.

5.3. Results and Discussions

5.3.1. Parameters Determination for the Calculation of $LiFePO_4$ CV Profiles

Particle size: As stated in Chapter 4, the characteristic length of a $LiFePO_4$ particle is the length of the aggregated particles, which is around 300 nm for the utilized $LiFePO_4$ sample (Figure 5.1).

Equilibrium potential and accommodation energy**:** Figure 5.2a shows the plot of the equilibrium potential versus normalized capacity for $LiFePO_4$ obtained from the GITT test. The plateaus in Figure 5.2a correspond to the two-phase regions, and the descending curves correspond to the single-phase region. Functions were used to fit the equilibrium potential-composition isotherms (Table 5.1), and the resultant fitting lines (dashed lines in Figure 5.2a) well described the experimental data. The phase transformation accommodation energies during the charge and discharge process were calculated from the plot of equilibrium potential versus composition (Figure 5.2a). The calculated phase transformation accommodation energy during charge and discharge are plotted in Figure 5.2b, and the relationship between the accommodation energy and the interface position (*ratio of transformed volume to total volume*) was expressed in Table 5.1 for both the charge and discharge processes. The theoretical (*strain-free*) equilibrium potential E_{eq} in the two-phase region, which was used to calculate the accommodation energy is determined by averaging the initial equilibrium phase transformation potentials during charge and discharge. As shown in Figure 5.2b, the discharge accommodation energy is larger than the charge accommodation energy at 50% SOD. The equilibrium potential-composition curves and accommodation energies of $LiFePO_4$ during lithiation and delithiation are similar to the results in the previous GITT study in Chapter 4, although the two $LiFePO_4$ samples are provided by different vendors.

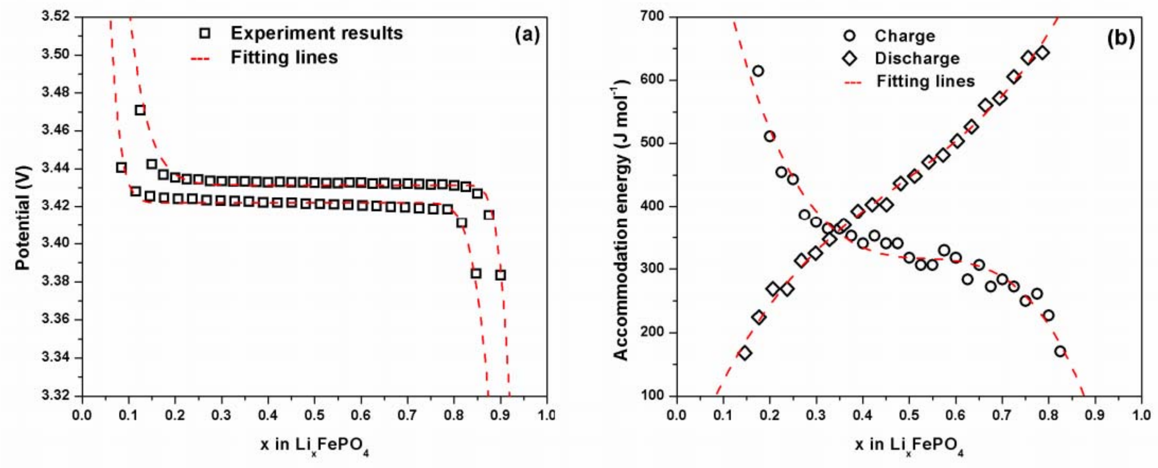

Figure 5.2. (a) Equilibrium potential-composition isotherm obtained using GITT, and (b) charge and discharge accommodation energy during phase transformation.

Table 5.1. Parameters used for CV simulation.

Parameters	Charge	Discharge
Particle size (*nm*)	300	300
Density of $FePO_4$ particle (ρ) (*g/cm³*)	3.6	3.6
$C_{\max}$ (*mol/cm³*)	0.02119	0.02119
Strain-free equilibrium potential E_{eq} (*V*)	3.4279	3.4279
$\Delta G_{accom} = f(x_i)$ (*J/mol*)	$f(x_i) = 0.006113 - 0.01416x_i$ $+0.02510x_i^2 - 0.01510x_i^3$	$f(x_i) = 0.007197 - 0.007835x_i$ $+0.008458x_i^2 - 0.005820x_i^3$
Equilibrium potential-composition isotherm for phase transformation *E(x)*	$E_c(x) = 3.43128 + 0.67858\exp(-36.6886x^{1.27087})$ $-2.1254\exp(-\frac{1.02622}{x^{12.56987}})$	$E_d(x) = 3.4219 + 0.69926\exp(-140.28201x^{1.52179})$ $-2.16183\exp(-\frac{1.06065}{x^{7.86426}})$
Equilibrium potential-composition isotherm for α phase	$E_{\alpha c}(x_\alpha) = 2.7082 - 0.4301\ln(\frac{x}{1-x} + 0.03782)$	$E_{\alpha d}(x_\alpha) = 2.0311 - 0.6648\ln(\frac{x}{1-x} + 0.4296)$
Equilibrium Potential-composition isotherm for β phase	$E_{\beta c}(x_\beta) = 4.0760 - 0.3200\ln(\frac{x}{1-x} - 0.4613)$	$E_{\beta d}(x_\beta) = 3.8537 - 0.2884\ln(\frac{x}{1-x} - 0.1123)$
Exchange current density i_0 for β phase (A g^{-1})	0.25	0.35
Exchange current density i_0 for α phase (A g^{-1})	0.4	0.5
Electrode resistance (Ω) (including both SEI film and electrolyte resistance)	33	33

Transfer coefficient γ	0.5	0.5

Exchange current density and electrode resistance: To obtain the exchange current density i_0, the electrolyte resistance R_{ele}, and the SEI film resistance R_{SEI}, EIS tests were performed on $LiFePO_4$ electrodes at different SOD and SOC. Figure 5.3 a & b show the Nyquist plot of the $LiFePO_4$ electrode at different charge and discharge states. The Nyquist plots of the $LiFePO_4$ electrode consist of two semicircles at high and middle frequency and a straight line at low frequency. The high frequency semicircle is attributed to the SEI film, the middle frequency semicircle to the charge transfer, and the low frequency line to the Li-ion diffusion. As shown in Figure 5.3 a & b, both the SEI film resistance and the charge transfer resistance slightly increase with the SOD and decrease with the SOC, but the electrolyte resistance remains stable. The charge transfer, SEI film, and electrolyte resistances at different SOC and SOD were obtained by fitting the impedance data with the equivalent circuit (inset in Figure 5.3a). The combined electrolyte resistance and SEI film resistance are defined as the electrode resistance in this study. The exchange current was calculated from the charge transfer resistance R_{ct} according to following equation

$$i_0 = \frac{RT}{FR_{ct}} \tag{5.23}$$

where R is the universal gas constant (J mol^{-1} K^{-1}), T is the temperature (K), F is Faraday constant (C mol^{-1}) and R_{ct} is the charge transfer resistance (Ω).

During the discharge process of a fully charged $LiFePO_4$ electrode, the outer phase in contact with the electrolyte changes from the initial Li-ion deficient phase (α phase) to the Li-ion rich phase (β phase) when phase transformation starts. Since the charge transfer reaction occurs on the surface of $LiFePO_4$ particles in contact with the electrolyte, the exchange current of α phase was determined from EIS at 0% SOD (Table 5.2) and the exchange current of β phase was obtained by averaging the exchange currents measured from EIS at SOD of 20%, 40%, 60%, 80% and 100% (Table 5.2). The exchange currents of α and β phases are listed in Table 5.1. Similarly, the average value of the exchange current of the initial β phase and the following α phase in the charge process were also measured using EIS in Figure 5.3a and listed in Table 5.1. Since the double layer capacitance and SEI layer capacitance are small, and the scan rates in CV are low, SEI film impedance is treated as pure resistance.

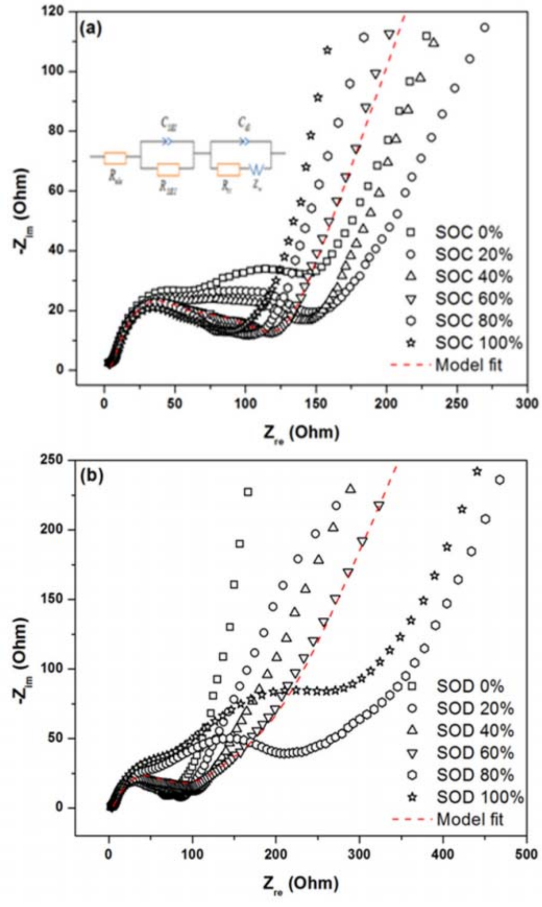

Figure 5.3. Electrochemical impedance spectroscopes of $LiFePO_4$ at different state of charge (a) and different state of discharge (b). The red dashed lines in both figures are fitting curves using the

equivalent circuit inserted in (a). The equivalent circuit consists of a resistor, a resistor paralleled with a constant phase element (CPE), and a CPE parallels with a resistor which is connected with a Warburg element in series.

Table 5.2. Charge transfer resistance and exchange current density at different SOD and SOC.

	Charge		Discharge	
SOD/(SOC)	R_{ct} (Ω)	i_0 (A g^{-1})	R_{ct} (Ω)	i_0 (A g^{-1})
0%/(100%)	103.3	0.248	158.1	0.16
20%/(80%)	90.42	0.281	134.3	0.19
40%/(60%)	95.8	0.296	63.68	0.4
60%(40%)	71.29	0.356	60.8	0.42
80%/(20%)	61.21	0.420	54.0	0.47
100%/(0%)	60.86	0.422	47.1	0.54

By numerically solving the differential equations under corresponding initial and boundary with the numerical method of lines (MOL) approach by the Maple software, the Li-ion concentration profiles and the current densities during the CV process can be obtained. Since the particle size, equilibrium potential, accommodation energy, exchange current density, and electrode resistance in the mixed-control model integrated CV are already determined, unknown parameters are only diffusion coefficients and interface mobility which can be obtained by curve fitting between experimental CV data and simulated results from the mixed-control model through adjusting these parameters.

5.3.2. Validation of Mixed-Control Model Integrated CV and Comparison with Traditional CV

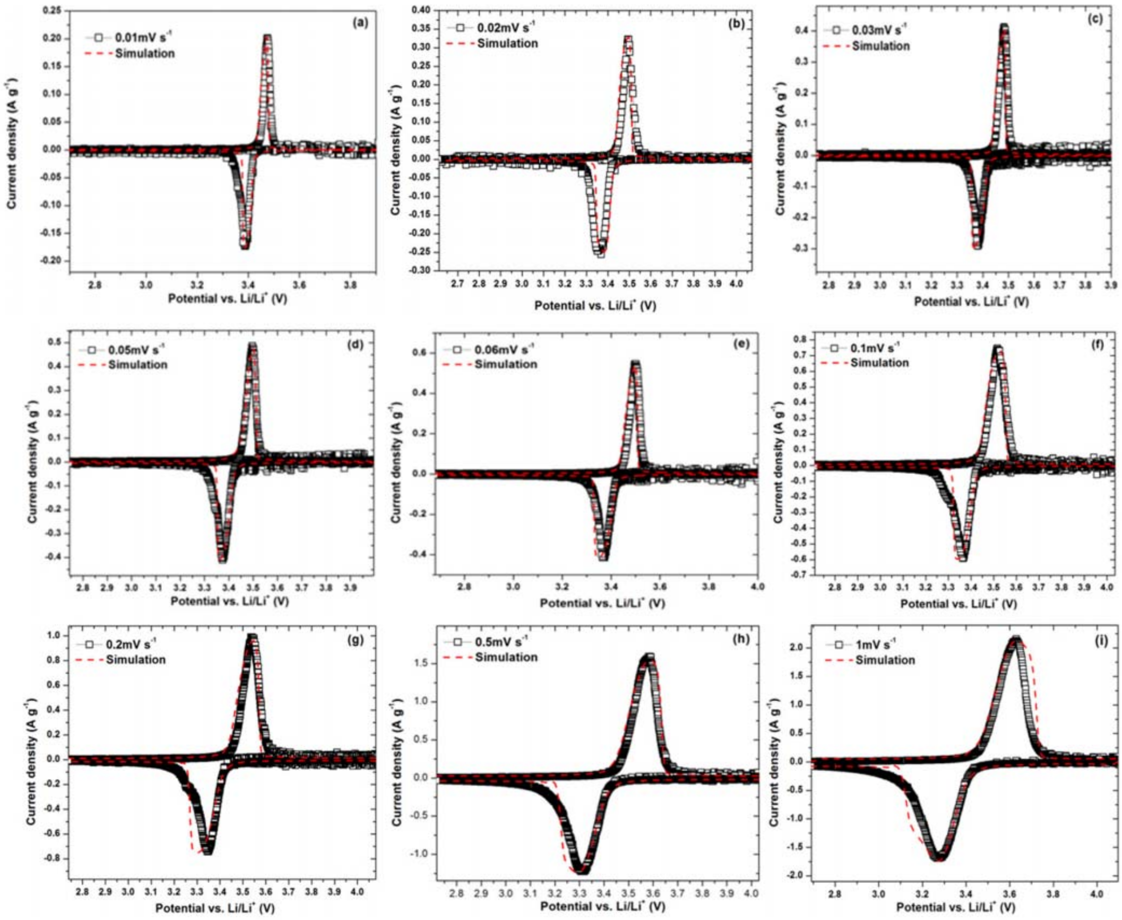

Figure 5.4. Comparison between measured CV profiles and simulated CV curves at different scan rates, (a) 0.01mV s^{-1}, (b) 0.02 mV s^{-1}, (c) 0.03 mV s^{-1}, (d) 0.05 mV s^{-1}, (e) 0.06mV s^{-1}, (f) 0.1 mV s^{-1}, (g) 0.2 mV s^{-1}, (h) 0.5 mV s^{-1}, (i) 1 mV s^{-1}.(symbols, experiments; dashed lines, model).

Figure 5.4 shows the experimental and simulated CV curves of $LiFePO_4$ at different scan rates. As shown in Figure 5.4, the charge and discharge CV scans consist of anodic and cathodic current peaks corresponding to the Fe^{2+}/Fe^{3+} redox couple. Both the peak current values and peak potential separations increase with the scan rates, which is in agreement with results reported by other researches [3-6]. The experimental CV scans were fitted by using mixed-control model integrated CV with determined parameters (exchange current, electrode resistance, particle size, equilibrium potential and accommodation energy) and three adjustable parameters (diffusion coefficients in α (D_α) and β (D_α) phases and the interface mobility (M)). As presented in Figure 5.4, the well agreement between the experimental data and simulation results at various scan rates validates the mixed-control model integrated CV.

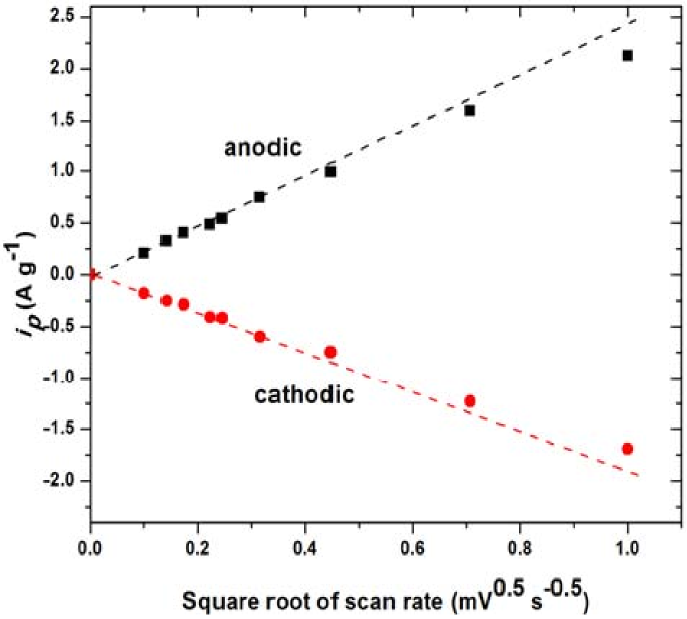

Figure 5.5. Dependence of peak currents of $LiFePO_4$ on square root of scan rate for $LiFePO_4$ sample.

Figure 5.5 shows the relationship between peak current and square root of scan rate obtained from the experimental data in Figure 5.4. As shown in Figure 5.5, the anodic (delithiation) and cathodic (lithiation) peak currents both show linear dependence on the square root of the scan rate at the scan rates under 0.2 mV s^{-1}. However, when the scan rate is higher than 0.2 mV s^{-1}, the peak currents are smaller than the values predicted by the traditional CV (dashed line in Figure 5.5). This observation is in agreement with results reported by other researchers [4]. This deviation from a linear relationship suggests that $LiFePO_4$ may not be solely controlled by Li-ion diffusion, and that phase transformation needs to be considered.

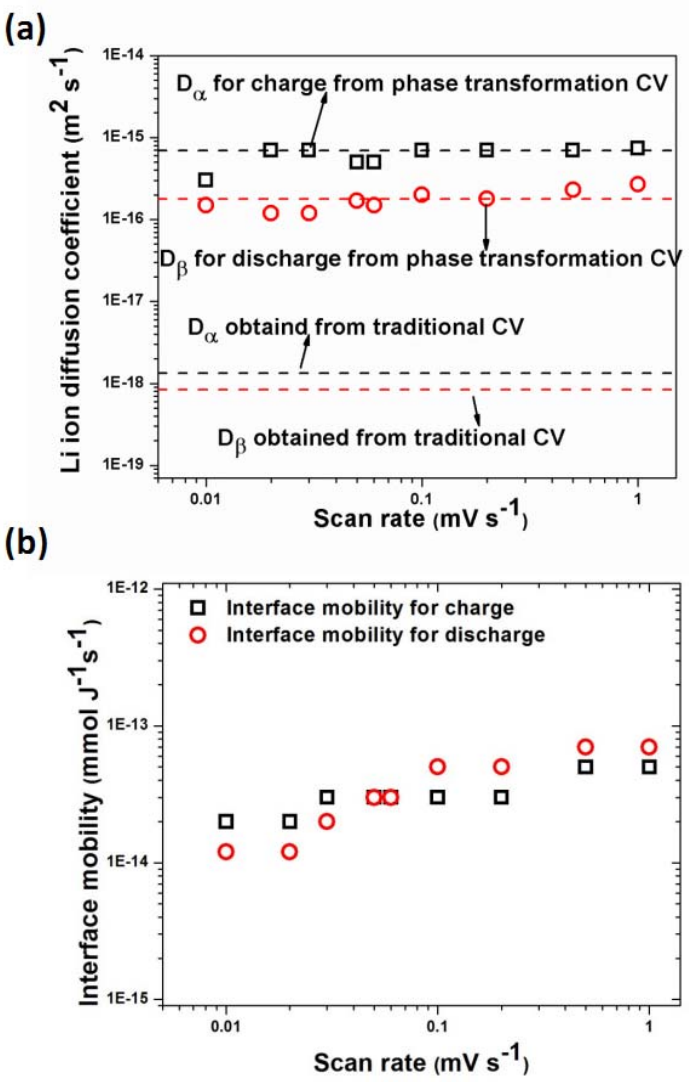

Figure 5.6. (a) Li-ion diffusion coefficient, and (b) interface mobility in $LiFePO_4$ obtained by curve fitting from mixed-control model integrated CV**.**

According to Figure 5.5, the diffusion coefficients for both the anodic and cathodic processes were calculated based on the traditional CV by using Eq. (1.3), and the obtained values were presented in Figure 5.6a as dashed lines. As shown in Figure 5.6a, the diffusion coefficient calculated from Eq. (1.3) by using traditional CV is on the order of 10^{-19}~10^{-18} m^2 s^{-1}, which agrees with the value obtained by other researchers using traditional CV [4, 5]. However, the obtained diffusion coefficients from traditional CV are one or two orders of magnitude lower than those measured in the single-phase region by using traditional PITT [1] and GITT [16]. This result is unreasonable since the composition and structure of the α phase before and after β phase deposition are almost the same, so the diffusion coefficient of Li-ion in the α phase should be similar before and after β phase formation. The reduced diffusion coefficient by using traditional CV may be attributed to the neglected phase transformation.

Using mixed-control model integrated CV, the Li-ion diffusion coefficient and interface mobility for both the anodic and cathodic processes were obtained by curve fitting, and plotted in Figure 5.6 a & b. The current density is directly related to the Li-ion flux on the surface of outer phase which directly contacts with electrolyte. In the phase transformation region, the outer phase is α phase and the inner phase is β phase during the charge process, while the inner phase is α phase and the outer phase is β phase during discharge process. Our simulations appropriately found that the Li-ion diffusion coefficient of the inner phase had a minor effect on the resultant CV profiles when compared to the outer phase. So, only the Li-ion diffusion coefficients for the outer phase, e.g. D_α for the anodic (charge) and D_β for the cathodic (discharge) process, were plotted against scan rate in Figure 5.6a. The diffusion coefficient obtained through curve fitting by the mixed-control model integrated CV is on the order of 10^{-16} m^2 s^{-1}, which is two or three orders higher than the value calculated from Eq. (1.3) using traditional CV, but is close to the values in the single α or β phase region obtained through PITT [1], EIS [1] and PITT [16]. Therefore, the mixed-control model integrated CV can accurately determine the diffusion coefficient of phase transformation electrode materials at the phase transformation region. The interface mobility obtained from mixed-control model integrated CV is plotted against scan rate in Figure 5.6b, which is on the order of 10^{-14} m mol J^{-1} s^{-1}. Both the Li-ion diffusion coefficient (Figure 5.6a) and the interface mobility (Figure 5.6b) obtained through mixed-control model integrated CV in this study are slightly higher than THE obtained values using mixed-control model integrated GITT in previous Chapter [16]. Two possible reasons are (1) the disregard of the charge transfer and SEI/electrolyte resistance in the mixed-control model integrated GITT, and (2) the use of different $LiFePO_4$ samples in the two studies. It has been demonstrated that, without consideration of electrode resistance (charge transfer, SEI film and electrolyte), the obtained diffusion coefficient is lower than its actual value [17]. Yu *et al* [4]. reported that the electrolyte compositions and electrode thickness also affect the peak current, suggesting that the electrode resistance and exchange current need to be included in the model. As shown in Figure 5.6a, the Li-ion diffusion coefficient obtained by curve fitting is higher for the anodic process (D_α) than the cathodic process (D_β) which means that Li-ion diffusion coefficient in Li_xFePO_4 is slightly higher than that in $Li_{1-y}FePO_4$, although the interface mobility is on the same order in Figure 5.6b. This might be one of the reasons why the charge rate capability is better than discharge rate capability for $LiFePO_4$ [18].

5.3.3. Characterization of Phase Transformation Electrodes Using Mixed-Control Model Integrated CV

To realize the power of CV technique in the characterization of phase transformation electrode materials, the CV profiles of phase transformation electrode materials are analyzed by using mixed-control model integrated CV. Therefore, the effects of phase transformation, electrode resistance, and ion diffusion on the CV profiles are all accounted for.

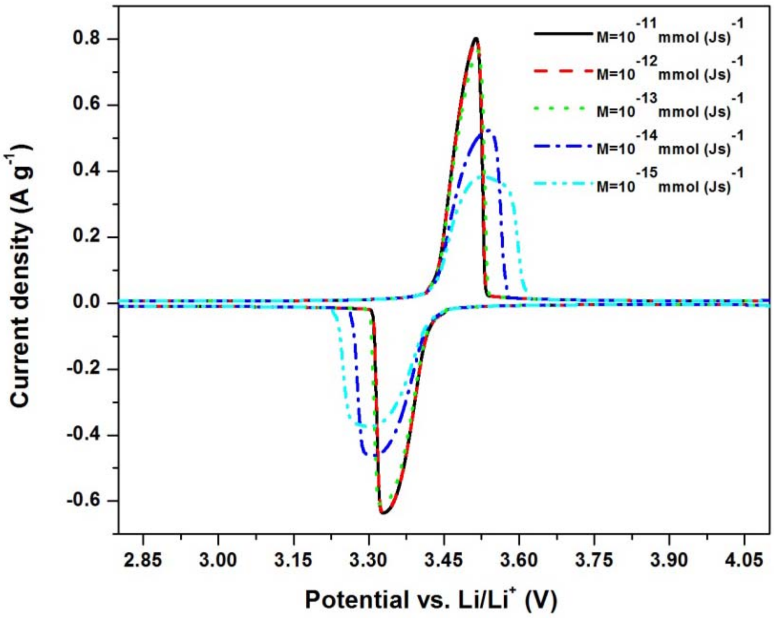

Figure 5.7. Simulated CV profiles of $LiFePO_4$ at different interface mobility values (scan rate: 0.1 mV s^{-1}. D_α=5×10^{-16} m^2 s^{-1} and D_β=2×10^{-16} m^2 s^{-1}).

Effect of phase transformation on CV profiles. Figure 5.7 presents simulated CV profiles at a scan rate of 0.1 mV/s with the interface mobility values ranging from 10^{-15} to 10^{-11} m mol J^{-1} s^{-1}. As shown in Figure 5.7, both the anodic and cathodic peak currents increase as the interface mobility increases. No significant difference exists between CV profiles when interface mobility is larger than 10^{-12} m mol J^{-1} s^{-1}. As the interface mobility increases, the peak current profile becomes sharp, and the potential separation between the anodic and the cathodic peak currents becomes narrow.

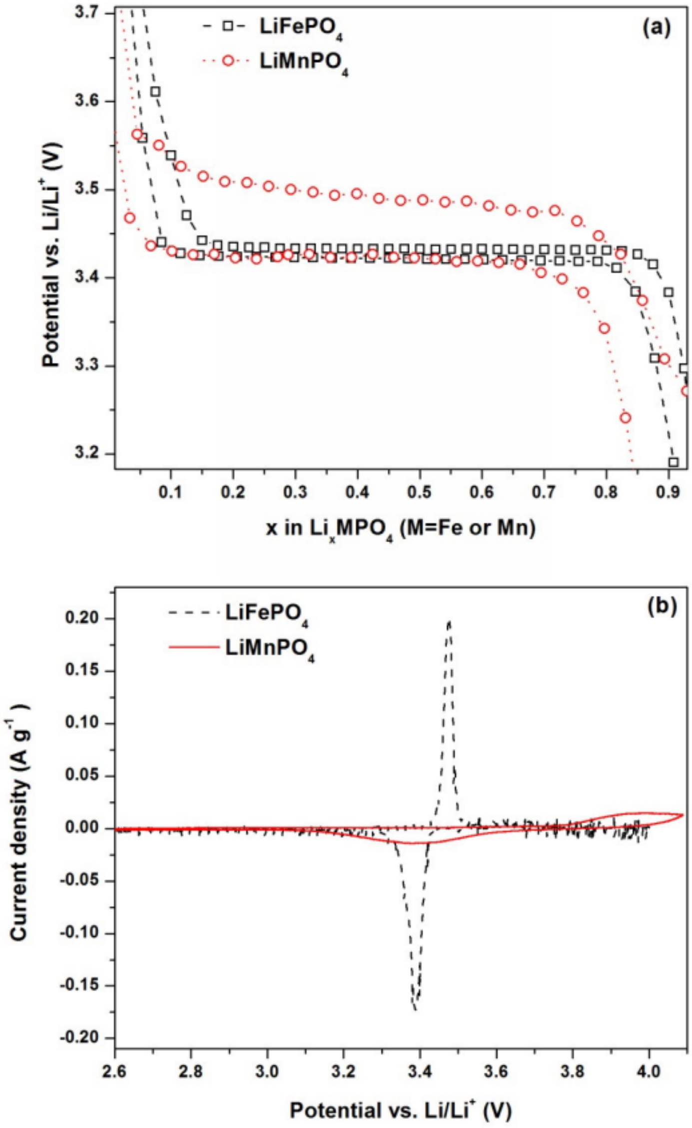

Figure 5.8. (a) Equilibrium potential-composition isotherm of $LiFePO_4$ and $LiMnPO_4$ electrodes measured using GITT, (b) measured CV curves of $LiFePO_4$ and $LiMnPO_4$ at scan rate 0.01 mV s^{-1} (To better compare both GITT and CV results between $LiFePO_4$ and $LiMnPO_4$, the Li insertion potential of $LiMnPO_4$ was shifted to the same lithiation potential of $LiFePO_4$).

The effect of interface mobility on CV curves in Figure 5.7 was confirmed by the difference of CV profiles between $LiFePO_4$ and $LiMnPO_4$ in Figure 5.8. As $LiFePO_4$,

$LiMnPO_4$ also undergoes a first order phase transformation during charge and discharge but at a higher redox potential of 4.1 V, which makes it a promising candidate for cathode materials of Li-ion batteries. To easily compare two CV curves, the discharge equilibrium potential (4.1 V) of $LiMnPO_4$ is shifted to the discharge equilibrium potential (3.4 V) of $LiFePO_4$. Unlike $LiFePO_4$, $LiMnPO_4$ has much lower interface mobility than that of $LiFePO_4$ due to a large volume change during phase transformation [11, 19, 20]. The large volume change in $LiMnPO_4$ also enhances the strain accommodation energy in phase transformation, resulting in a larger potential hysteresis in Figure 5.8a and wider potential separation between anodic and catholic peak-currents in Figure 5.8b. Figure 5.8a shows a comparison of the equilibrium potential-composition isotherms between shifted $LiMnPO_4$ and $LiFePO_4$ measured by GITT. The potential hysteresis between the charge and discharge equilibrium potential is around 70 mV for $LiMnPO_4$, which is 7 times higher than that of $LiFePO_4$ (10 mV). Figure 5.8b shows the CV curves for both materials at scan rate 0.01mV s^{-1}. A slow scan rate was used because of the poor kinetics of $LiMnPO_4$. The $LiMnPO_4$ and $LiFePO_4$ samples tested in Figure 5.8 have a comparable particle size, and both were coated with carbon to increase the electronic conductivity. Compared to the $LiFePO_4$ CV curve, the CV curve for $LiMnPO_4$ has much smaller peak current values, a wider peak shape, and larger peak potential separation, which is in agreement with the simulated CV profile of phase transformation electrode materials with low interface mobility (Figure 5.7). Therefore, if all other electrode properties are the same, the peak current value and peak shape can be used to roughly judge the relative value of the interface mobility between phase transformation electrode materials. The peak potential separation can be used to evaluate both thermodynamic potential hysteresis and reaction kinetics, which will be shown below.

Effects of the electrode properties on the CV profiles. Different electrode parameters have different effects on CV profiles. If we know how the electrode parameters affect the resultant CV profiles of phase transformation electrode materials, we can analyze the thermodynamics and kinetics of the reaction by comparing the CV profiles.

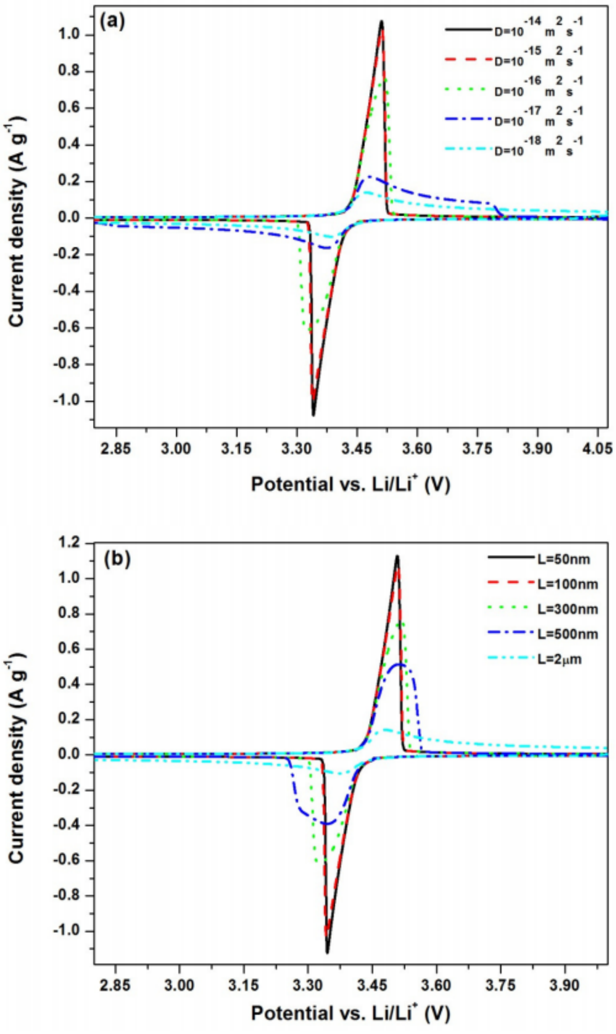

Figure 5.9. Simulated CV profiles of $LiFePO_4$ at (a) different Li ion diffusion coefficients, (b) different sample particle sizes with scan rate 0.1 mV s^{-1} (interface mobility M=10^{-13} m mol (J s)$^{-1}$, particle size in (a): L=300nm).

The effect of the Li-ion diffusion coefficient and the particle size on CV profiles was investigated. As shown in Figure 5.9, with the increasing of Li-ion diffusion coefficient or decreasing of particle size, the peak currents increase and become sharp due to the improvement of Li-ion transport. The potential separation between anodic and cathodic peak currents did not show a general increase or decrease as of the Li-ion diffusion coefficient or sample particle size changed.

The diffusion coefficient mentioned above is a chemically effective diffusion coefficient that considers the movement of both the Li-ion and electron, and can be obtained by following equation [21]

$$D = \frac{2D_{Li^+}D_e}{D_{Li^+}D_e} \tag{5.24}$$

where D is the chemical diffusion coefficient, and D_{Li^+} and D_e are the diffusion coefficients for the Li-ion and electron, which can be related to the ionic and electronic conductivity by the Nernst-Einstein equation [22]. Coating carbon or other conductive materials can greatly improve the electronic conductivity of the electrode materials, which also increases the chemical diffusion coefficient. The CV profiles of uncoated and carbon nanotube coated $LiFePO_4$ in Ref [23], and the CV curves of uncoated and PbZe coated $LiFePO_4$ in Ref [24] are very similar to the simulation results shown in Figure 5.9, validating the mixed-control model integrated CV.

Figure 5.10 demonstrates the effects of different electrode resistances on CV profiles. Figure 5.10a shows CV profiles for different charge transfer resistances with the exchange current density ranging from $0.01i_0$ to $100i_0$, where i_0 is the exchange current density measured for current $LiFePO_4$ sample. As shown in Figure 5.10a, with the increasing of the charge transfer resistance (decreasing of exchange current density), the peak currents of the CV profile decreased, the potential separation between the anodic and the cathodic peak current enlarged, and the peak current profiles became wide. In Figure 5.10b, as the electrode resistance R_e (includes the electrolyte and SEI film resistance) increases from 0 to 100 ohms, the changes in the CV profiles are analogous to the above described changes in Figure 5.10a.

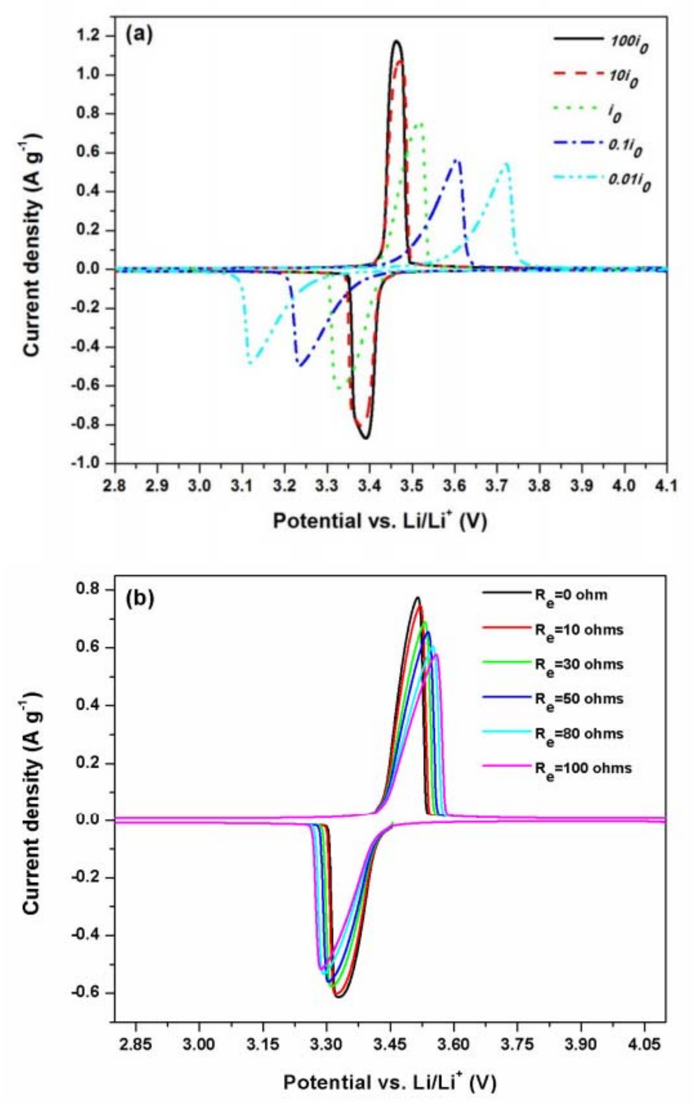

Figure 5.10. Simulated CV profiles at (a) different charge transfer resistances, (b) different electrode resistances (scan rate 0.1 mV s^{-1}; D_α=5×10^{-16} m^2 s^{-1}, D_β=2×10^{-16} m^2 s^{-1} and M=10^{-13} m mol (J s)$^{-1}$).

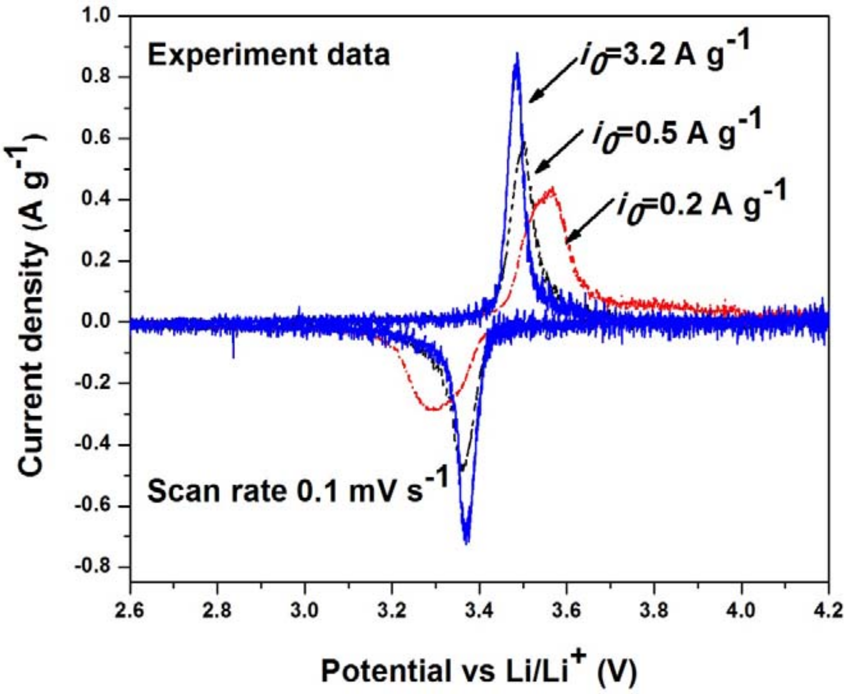

Figure 5.11. Measured CV curves of a $LiFePO_4$ electrode with different exchange currents.

The simulated CV profiles under different exchange current densities in Figure 5.10a were confirmed by the CV results of $LiFePO_4$ electrodes with different exchange currents (Figure 5.11). The different exchange currents for $LiFePO_4$ electrode were obtained by using EIS after charging/discharging the electrode at 1*C* rate for different cycles. As shown in Figure 5.11, with the increasing of the charge transfer resistance (decreasing of exchange current density), the peak currents of the CV profiles decreased, the peak potential separation increased, and the peak shape became wider, which are the predicted trends from the mixed-control model integrated CV. The CV profile of a $LiFePO_4$ electrode in different electrolytes reported by Yu *et al*. [4] is also similar to the simulated CV profile in Figure 5.10a. Since the charge transfer resistance of $LiFePO_4$ electrodes changes with electrolyte composition, the difference in CV profiles in Ref. [4] can be attributed to the difference in exchange current densities of $LiFePO_4$ in different electrolytes.

5.4. Summary

Mixed-control model integrated cyclic voltammetry (CV) is developed in this Chapter. $LiFePO_4$ is used as a specific example to validate this model. The agreement between the simulated CV profiles and the experimental data at different scan rates validates this mixed-control model integrated CV. The diffusion coefficient (10^{-16} m^2 s^{-1}) of $LiFePO_4$ obtained through curve fitting by using mixed-control model integrated CV is two or three orders of magnitude larger than that determined by using traditional CV, which is due to the inclusion of phase transformation, charge transfer and electrode resistances in the mixed-control model. The interface mobility (10^{-14} m mol J^{-1} s^{-1}) obtained by the mixed-control model integrated CV is slightly higher than that obtained from the mixed-control model integrated GITT, since the charge transfer resistance and electrode resistance, which were not considered in mixed-control model integrated GITT, are included in this comprehensive CV model.

Mixed-control model integrated CV is also a powerful technique for analyzing the thermodynamics and kinetics of phase transformation electrode materials. The potential separation between peak currents in CV will provide relative values of the potential hysteresis or charge transfer resistance. The change in peak current and peak shape can be used to evaluate the interface mobility (M) and diffusion capability (L^2/D). The mixed-control model integrated CV demonstrated that the peak potential separation increased with increasing potential hysteresis and decreasing exchange current, which was confirmed through comparisons of CV profiles of $LiFePO_4$ and

$LiMnPO_4$ electrodes and the profiles of the $LiFePO_4$ electrode at different charge/discharge cycles. Also, the peak current increases and peak shape becomes sharp with increasing interface mobility and diffusion capability, which is in agreement with reported CV profiles.

5.5. References

1. J. Xie, N. Imanishi, T. Zhang, A. Hirano, Y. Takeda, and O. Yamamoto, Li-ion diffusion kinetics in $LiFePO_4$ thin film prepared by radio frequency magnetron sputtering. *Electrochimica Acta* **54**, 4631-4637 (2009).
2. T. Nakamura, K. Sakumoto, S. Seki, Y. Kobayashi, M. Tabuchi, and Y. Yamada, Apparent diffusion constant and electrochemical reaction in $LiFe_{1-x}Mn_xFePO_4$ olivine cathodes. *J. Electrochem. Soc.* **154**, A1118-A1123 (2007).
3. S. Franger, C. Bourbon, and F. Le Cras, Optimized lithium iron phosphate for high-rate electrochemical applications. *J. Electrochem. Soc.* **151**, A1024A-A1027 (2004).
4. D. Y. Yu, C. Fietzek, W. Weydanz, K. Donoue, T. Inoue, H. Kurokawa, and S. Fujitani, Study of $LiFePO_4$ by cyclic voltammetry. *J. Electrochem. Soc.* **154**, A253-A257 (2007).
5. T. Nakamura, K. Sakumoto, M. Okamoto, S. Seki, Y. Kobayashi, T. Takeuchi, M. Tabuchi, and Y. Yamada, Electrochemical study on Mn^{2+}-substitution in $LiFePO_4$ olivine compound. *J. Power Sources* **174**, 435-441 (2007).

6. M. Takahashi, S. Tobishima, K. Takei, and Y. Sakurai, Reaction behavior of $LiFePO_4$ as a cathode material for rechargeable lithium batteries. *Solid State Ionics* **148**, 283-289 (2002).

7. M. Konarova and I. Taniguchi, Preparation of $LiFePO_4/C$ composite powders by ultrasonic spray pyrolysis followed by hear treatment and their electrochemical properties. *Mater. Res. Bull.* **43**, 3305-3317 (2008).

8. J. F. Ni, H. H. Zhou, J. T. Chen, and X. X. Zhang, $LiFePO_4$ doped with ions prepared by co-precipitation method. *Mater. Lett.* **59**, 2361-2365 (2005).

9. H. Liu, Q. Cao, L. J. Fu, C. Li, Y. P. Wu, and H. Q. Wu, Doping effects of zinc on $LiFePO_4$ cathode material for lithium ion batteries. *Electrochem. Commun.* **8**, 1553-1557 (2006).

10. J. Ma and Q. Qin, Electrochemical performance of nanocrystalline $LiMPO_4$ thin-films prepared by electrostatic spray deposition. *J. Power Sources* **148**, 66-71 (2005).

11. N. Meethong, H. -Y. S. Huang, S. A. Speakman, W. C. Carter, and Y. M. Chiang, Strain accommodation during phase transformations in olivine-based cathodes as a materials selection criterion for high-power rechargeable batteries. *Adv. Funct. Mater.* **17**, 1115-1123 (2007).

12. Y-M. Chiang, N. Meethong, H-Y. S. Huang, W. C. Carter, S. Chang, A. Hsiao, and A. S. Gozdz, ESC Meeting, Cancun, Mexico, November 2006.

13. N. Meethong, H-Y. S. Huang, S. A. Speekman, W. C. Carter, and Y-M. Chiang, Size-dependent lithium miscibility gap in nanoscale $Li_{1-x}FePO_4$. *Electrochem. Solid-State Lett.* **10**, A134-A138 (2007).

14. A. J. Bard and L. R. Faulkner, *Electrochemical Methods*, John Wiley & Sons, Inc., New York, (**1980**).

15. D. A. Porter and K. E. Easterling, *Phase transformation in metal and alloys*; New York, **1981**, 287-290.

16. Y. Zhu and C. Wang, Galvanostatic intermittent titration technique for phase-transformation electrodes. *J. Phys. Chem. C* **114**, 2830-2841 (2010).

17. C. Montella. Discussion of the potential step method for the determination of the diffusion coefficient of guest species in host materials: Part Ⅰ. Influence of charge transfer kinetics and ohmic potential drop. *J. Electroanal. Chem.* **518**, 61-83 (2002).

18. V. Srinivasan and J. Newman. Existence of path-dependence in the $LiFePO_4$ electrode. *Electrochem. Solid-state Lett.* **9**, A110-A114 (2006).

19. M. Yonemura, A. Yamada, Y. Takei, N. Sonoyama, and R. Kanno. Comparative kinetic study of olivine Li_xMPO_4 (M=Fe, Mn). *J. Electrochem. Soc.* **151**, A1352-A1356 (2004).

20. H. Gabrisch, J. Wilcox, and M. M. Doeff, TEM study of fracturing in spherical and plate-like LiFePO4 particles. *Electrochem. Solid-state Lett.* **11**, A25-A29 (2008).

21. K. Striebel, J. Shim, V. Srinivasan, and J. Newman, Comparison of $LiFePO_4$ from different sources. *J. Electrochem. Soc.* **152**, A664-A670 (2005).

22. M. S. Whittingham, Y. Song, S. Lutta, P. Y. Zavalij, and N. A. Chernova, Some transition metal (oxy)phosphates and vanadium oxides for lithium batteries. *J. Mater. Chem.* **15**, 3362-3379 (2005).

23. J. Xu, G. Chen, and X. Li, Electrochemical performance of $LiFePO_4$ cathode material coated with multi-wall carbon nanotubes. *Mater. Chem. Phys.* **118**, 9-11 (2009).

24. J. Xu and G. Chen, Electrochemical performance of $LiFePO_4$ cathode material coated with PbTe. *Electrochem. Solid-state Lett.* **12**, H399-H401 (2009).

Chapter 6: *In Situ* Atomic-Scale Imaging of Phase Boundary Migration in $FePO_4$ Microparticles during Electrochemical Lithiation

Orthorhombic Li_xFePO_4 ($0 \leq x \leq 1$) system has attracted much attention for its application as a high power cathode material in lithium ion batteries [1]. Although the performance of this material has been greatly improved by cation doping [2], surface coating [3] and size reduction [4], the fundamental phase transformation mechanisms accompanying lithiation/delithiation are still controversial [5-18]. As shown in previous Chapters, the lithiation/delithiation of $LiFePO_4$ is usually accompanied by phase transition between $LiFePO_4$ and $FePO_4$, which is characterized by a voltage plateau around 3.4 V versus Li^+/Li in the charge/discharge curves. To account for the two-phase mechanism, a shrinking-core model [1, 5] was initially proposed to describe the lithiation/delithiation process in $LiFePO_4$ in which the $FePO_4$ core is covered by a $LiFePO_4$ shell during lithiation and the opposite is true during delithiation. Subsequently, Anderson *et al.* [6] proposed a "mosaic model" which considered the effect of different nucleation sites for Li-ion insertion/extraction and was essentially similar to the shrinking-core model. However, recent calculations [7-9] and experiments [10-12] have revealed that the lithiation/delithiation in $LiFePO_4$ is highly anisotropic and Li-ion diffusion is mainly confined in the [010] direction which invalidated the shrinking-core model. $LiFePO_4/FePO_4$ phase transition also exhibits strong misfit anisotropy in its lattice parameters. $FePO_4$ expands along [100]

(5%) and [010] (3.7%) directions but contracts in the [001] direction (-1.9%) upon Li-ion insertion [12].

Chen *et al*. [10] investigated chemically delithiated $Li_{0.5}FePO_4$ by high resolution transmission electron microscopy (HRTEM) and found out that the $LiFePO_4/FePO_4$ domains in a single particle were separated by dislocation lines running along the *c* ([001]) axis. The phase boundary was found to lie on (100) plane and suggested to move along the [100] direction upon Li-ion insertion/extraction. This phase transition mechanism was elaborated by Delmas *et al*. [13] in a "domino-cascade" model. On the basis of the facts that the partially delithiated $LiFePO_4$ electrodes consisted of either fully lithiated ($LiFePO_4$) or fully delithiated ($FePO_4$) particles, Delmas *et al*. [13] proposed that the growth kinetics of nano-$LiFePO_4$ are much faster than the nucleation and the phase transition between $LiFePO_4$ and $FePO_4$ is nucleation limited. The "domino-cascade" model was further elaborated by Singh *et al*. [14] through developing a dynamic lithiation/delithiation model which predicts that the movement of $LiFePO_4/FePO_4$ phase boundary is perpendicular to the direction of Li-diffusion and behaves like a "travelling wave". Laffont *et al*. [12] characterized the $LiFePO_4/FePO_4$ system with high-resolution electron energy loss spectroscopy (HREELS). They observed that the phase boundary between $LiFePO_4$ and $FePO_4$ is the juxtaposition of two phases rather than a solid solution with a concentration gradient. The phase boundary at the particle surface is not perfectly aligned with the (010) plane but has an inclination toward the [100] axis which is also suggested by Tang *et al*. from a comprehensive phase-field model [15]. The observed anisotropy of phase boundary is thermodynamically limited by the largest linear misfit strain along

[100] between $LiFePO_4$ and $FePO_4$, but kinetically favored by the fast Li-ion surface-reaction, high Li-ion diffusion anisotropy [15] and quick nucleation rate [16]. As recently reported by Chiang *et al.* [16], at a moderate overpotential of 25 mV, stress relaxation causes $LiFePO_4$ to grow along the [100] direction upon lithiation with the phase boundary parallel with (100) plane which has been observed by Chen *et al.* [10]. However, at a higher overpotential above 100 mV, the influence of strain energy is overcome and nucleation rate is fast. The lateral Li-ion diffusion dominates the phase transition and the phase boundary aligns much close to (010) plane [16]. The overpotential-dependent phase transition in $LiFePO_4$ was also simulated by Kao *et al.* [17] using a comprehensive phase-field model. The phase-field model predicted that a crystalline-to-crystalline phase transition pathway will appear at a high overpotential range.

One major challenge for current *ex situ* techniques is that all the experiments were conducted after fully relaxation of partially charged/discharged $LiFePO_4$, and lack of direct evidence of dynamic lithiation/delithaition processes which can be quite different from the equilibrium state. Malik *et al.* [18] recently calculated the free energy of Li_xFePO_4 ($0 \le x \le 1$) system and found out the existence of some non-equilibrium but low energy solid-solution states. Based on the calculation, the authors proposed that the discharge/charge of $LiFePO_4$ might follow a single-phase transition pathway rather than nucleation and growth of a second phase, since only very small overpotential is needed to change the particle from fully discharged to fully charged state or vice versa. At the same time, Bai *et al.* [19] developed a surface-reaction-limited phase field model and predicted that for nano-$LiFePO_4$, the phase transition from $FePO_4$ to $LiFePO_4$ will be suppressed if the discharge current density is higher than certain value and the particle is supposed to behave like a solid solution. However, the equilibrium state is always two-phase system with most stable configurations [18, 19].

Obviously, real-time atomic-scale observation of lithiation/delithiation of $LiFePO_4$ is critical to clarify the phase transformation mechanisms. However, such dynamic observations have not been achieved due to technical difficulties associated with the experiments. Here we report the first dynamic HRTEM observations of the phase boundary migration in microsized $FePO_4$ single-crystals during electrochemical lithiation, providing the first direct atomic-scale evidence for the phase boundary migration mechanism.

6.1. Experiments

6.1.1. Materials Synthesis

$LiFePO_4$ is synthesized by using a hydrothermal method. 10 mL of 4 M LiOH aqueous solution was mixed with 5 mL aqueous solution of 0.015 mol H_3PO_4 and 0.005 mol $(NH_4)_2HPO_4$ to form a white suspension. Then, 10 mL of 2 M $FeSO_4{\cdot}7H_2O$ aqueous solution was slowly added into above suspension with continuous stirring and argon purging. The molar ratio of Li:Fe:P was kept at 2:1:1. The mixture was transferred to a Parr autoclave, which was then held at 180 °C for 12 h. After natural cooling to room temperature, the product was collected and washed with ethanol and deionized (DI) water for several times. The final product was dried at 80 °C in a vacuum oven for overnight.

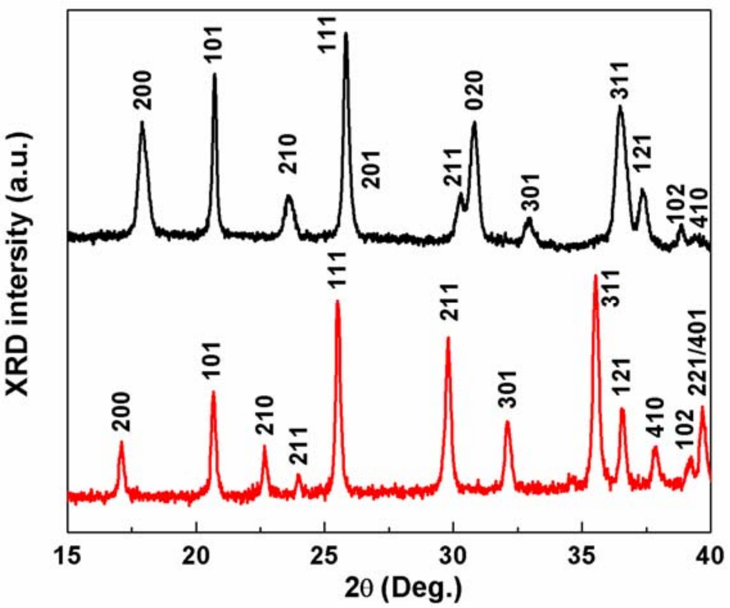

Figure 6.1. XRD patterns for synthesized $LiFePO_4$ and chemically delithiated $FePO_4$. The red and black lines are corresponding to $LiFePO_4$ and $FePO_4$, respectively. Both XRD patterns were indexed in the orthorhombic (*Pnma*) crystallographic system.

$FePO_4$ was obtained from chemical delithiation of $LiFePO_4$ using nitronium tetrafluoro-borate NO_2BF_4 in acetonitrile. 0.1 g $LiFePO_4$ was added into a solution of 0.17 g NO_2BF_4 in 10 mL acetonitrile. The mixture was stirred for 24 h at room temperature with continuous Ar bubbling, followed by centrifugation and washing with acetonitrile and DI water for several times. The product was dried at 80 °C in a vacuum oven for overnight. The crystal structures of both $LiFePO_4$ and $FePO_4$ were characterized by a powder X-ray diffraction (XRD) (Figure 6.1). Both XRD patterns were indexed in the orthorhombic (*Pnma*) crystallographic system and showed that there were no detectable impurities in the samples. The morphology of obtained $FePO_4$ was characterized by SEM. The results are shown in Figure 6.2. As shown by the SEM and TEM images in Figure 6.2, the $FePO_4$ samples used in this study were nearly needle-like with few micrometers in the longest dimension.

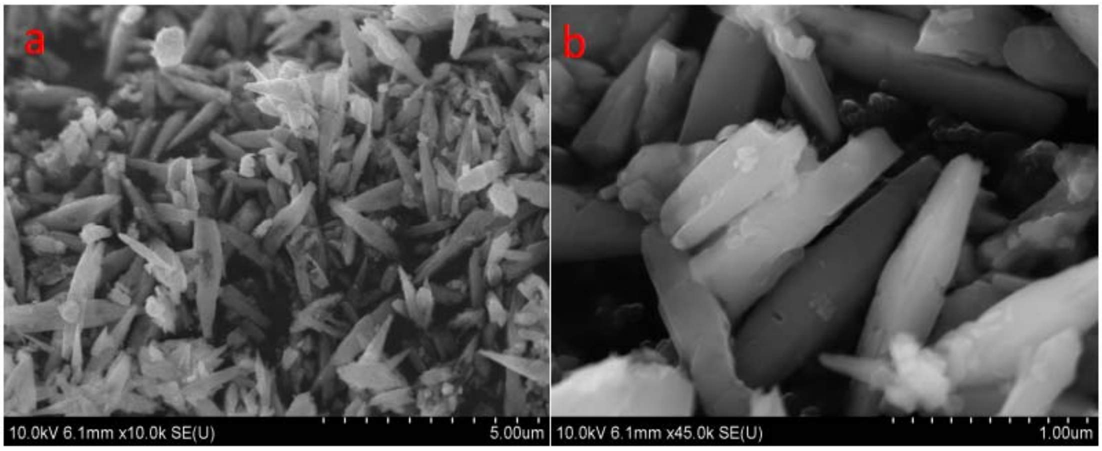

Figure 6.2. a,b, SEM images of pristine $FePO_4$ sample.

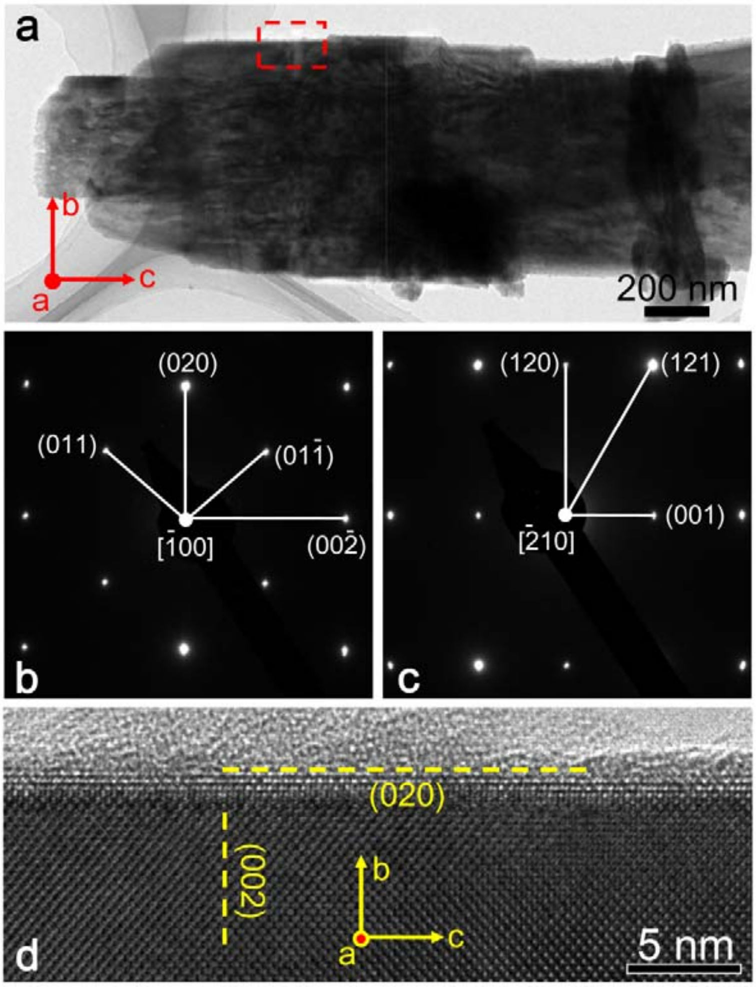

Figure 6.3. Determination of crystal orientation for the $FePO_4$ crystals. (a) Morphology of a typical $FePO_4$ crystal with *a*, *b* and *c* directions. (b,c) Two zone axes of the $FePO_4$ crystal in (a) were achieved

by using double tilt holder. (d) HRTEM image from the red dashed line rectangle zone in (a), which is tilted into $[\bar{1}00]$ zone axis. (020) plane and (002) plane are parallel and perpendicular to the length direction of the $FePO_4$ crystal, respectively, which confirms that the *c*-axis is along the length direction of present samples.

The orientation of $FePO_4$ crystals was determined by HRTEM and the results were shown in Figure 6.3. As shown in Figure 6.3b and c, the electron diffraction patterns (EDPs) are indexed with the lattice parameters: a = 9.826 Å, b=5.794 Å, and c=4.784 Å, and can be indexed as $[\bar{1}00]$ zone axis for Figure 6.3b and $[\bar{2}10]$ zone axis for Figure 6.3c with the orthorhombic structure, respectively. The EDPs indicate that the $FePO_4$ crystal is single-crystal with the *c*-axis parallel to the length direction.

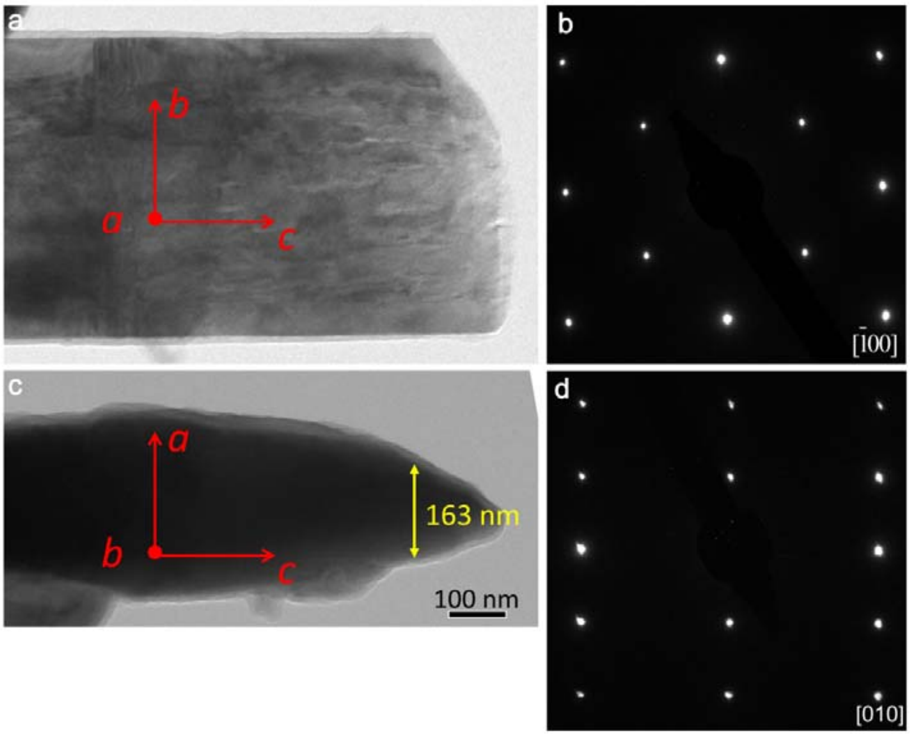

Figure 6.4. A typical $FePO_4$ particle tilted into both [-100] and [010] zone axes. (a,b) The morphology and diffraction pattern of $FePO_4$ particle in [-100] zone axis. (c,d) The morphology and diffraction pattern of $FePO_4$ particle in [010] zone axis with the thickness along *a*-axis (~160 nm) for the region, where $FePO_4$/$LiFePO_4$ phase boundary was observed, is marked.

To estimate the typical geometry, tilting experiments were conducted to show both the span and thickness of the $FePO_4$ particles. Figure 6.4 presents such an example, in which the pristine $FePO_4$ particle was tilted into the orthogonal [-100] and [010] zone axes. As shown in Figure 6.4, the sample has a thickness of 500 nm along *b*-axis and 300 nm along *a*-axis. To obtain the HRTEM images, we choose a thin part of the sample, which has a thickness around 160 nm along *a*-axis.

6.1.2. Electrode Preparation and Electrochemical Tests

The hydrothermally synthesized $LiFePO_4$ was coated with carbon by ball milling the as-prepared $LiFePO_4$ with 20wt. % sucrose in acetone for 1 h. The mixture was then heated to 600 °C for 5 h under Ar atmosphere with a heating rate of 2 °C/min. The $FePO_4$ sample was prepared by chemically delithiating above carbon-coated $LiFePO_4$ with nitronium tetrafluoroborate (NO_2BF_4) in acetonitrile.

$FePO_4$ electrodes were prepared by the slurry coating method. The active material was mixed with 15 wt% carbon black and 8 wt% polyvinylidene fluoride (PVDF) in 1-methyl-2-pyrrolidinone (NMP) solvent to form a viscous paste, which was then mixed for 30 min using a planetary ball milling machine. The obtained slurry was then coated onto aluminum foil and dried in a vacuum oven at 100 °C for overnight. The loading amount of the active material was 1-2 mg/cm^2. A coin cell consisting of a $FePO_4$ cathode, a Li metal anode, Celgard 3501 microporous film separators, and 1.0 M $LiPF_6$ in ethylene carbonate (EC): diethyl carbonate (DEC) (1:1 by volume) liquid electrolyte was used for electrochemical measurements. The galvanostatic charge/discharge tests with different specific currents were performed by using Solatron 1260/1287 Electrochemical Interface (Solatron Metrology, UK), and the results are shown in Figure 6.5. As shown in Figure 6.5, the electrochemical behaviors of chemically delithiated $FePO_4$ showed well-defined voltage plateaus during both charge and discharge processes similar to the electrochemical behaviors of typical $LiFePO_4$ electrodes, demonstrating that the lithiation mechanism of chemically delithiated $FePO_4$ also reflects the lithiation mechanism of electrochemically delithiated $FePO_4$ [20].

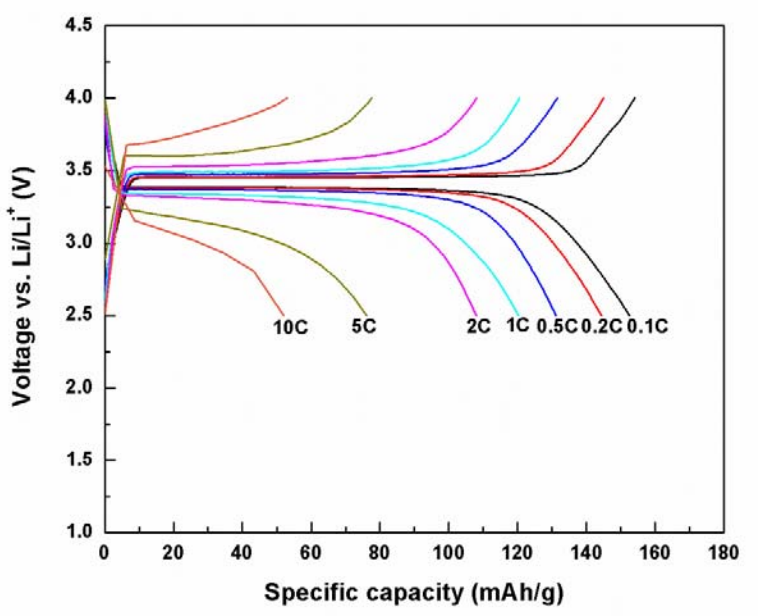

Figure 6.5. Galvanostatic charge-discharge curves for $FePO_4$ sample at different currents. Note: different C-rates are calculated based on the theoretical capacity of $LiFePO_4$ (170 mAh/g).

6.1.3. Setup of *In Situ* Experiments

In situ HRTEM observation of electrochemical lithiation in $FePO_4$ was conducted in an all-solid electrochemical cell setup, which consisted of a $FePO_4$ crystal working electrode, a naturally-grown Li_2O solid electrolyte, and a bulk lithium metal counter electrode (Figure 6.6a). The $FePO_4$ crystals were glued onto the aluminum rod with conductive epoxy. Fresh lithium metal was scratched from a fresh cut lithium metal surface by using a tungsten wire inside a glove box, and transferred into the TEM using a sealed bag filled with dry helium. During the transfer process, the lithium metal was exposed in air for about 2 s. The naturally-grown Li_2O served as the solid electrolyte. It has been shown that Li_2O can be functioned as an effective solid electrolyte for the lithium ion transport [21, 22]. The Li/Li_2O was driven to contact the $FePO_4$ crystal using a piezomanipulator (Nanofactory® transmission electron microscopy – scanning tunneling microscopy (TEM-STM) holder). Comparing with the conventional liquid cell, this kind of solid cell offers the advantage of direct observation of the microstructure evolution inside TEM, especially for the *in situ* HRTEM.

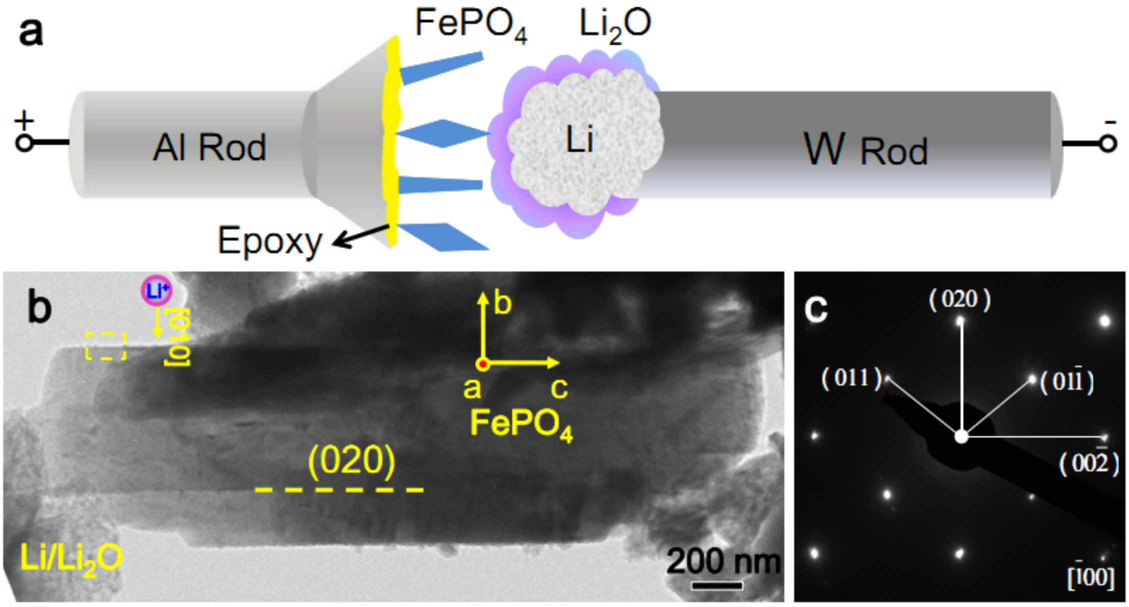

Figure 6.6. *In situ* TEM electrochemical experiment setup and morphology of $FePO_4$ crystal. (a) Schematic illustration of the *in situ* electrochemical cell. (b) A pristine $FePO_4$ crystal in [-100] zone axis was connected with the Li_2O electrolyte to form an electrochemical device. The propagation of a phase boundary between $FePO_4$ and $LiFePO_4$ in the rectangle zone marked by yellow dashed line was captured in real time under HRTEM, as presented in Figure 6.7. (c) The electron diffraction pattern

(EDP) of the $FePO_4$ crystal as shown in (b), indicating it is a single-crystal with the orthorhombic structure.

6.2. Results and Discussion

Figure 6.6b presents a TEM image of a pristine $FePO_4$ crystal connected to the Li_2O electrolyte. The EDPs of the $FePO_4$ crystal (Figure 6.6c and Figure 6.3) indicated that it was a single-crystal with the orthorhombic structure, and the growth direction was [001] (Figure 6.3). Before lithiation, the $FePO_4$ crystal was tilted into $[\bar{1}00]$ zone axis (Figure 6.6c) and the maximum thickness of the particle along this axis was around 300 nm (Figure 6.4). Different from many anode materials (Si, Sn, SnO_2 etc.), the volume change for $FePO_4$ upon lithiation is only 7%, which is too small to be observed at a low magnification TEM image. So HRTEM was used to follow the lithiation process.

Figure 6.7 shows HRTEM images of the phase boundary evolution from the rectangular zone in Figure 6.6b, during lithiation of $FePO_4$. The thickness along *a*-axis for this HRTEM observation region is less than 300 nm (Figure 6.4). A positive voltage of 2 V versus lithium metal was applied to the $FePO_4$ crystal in Figure 6.7 to drive lithium ion insertion into the crystal. To increase the conductivity and decrease the electron beam damage to $FePO_4$, 10 nm amorphous carbon (a-C) was coated on the surface of $FePO_4$ crystals (Figure 6.7a) and weak electron beam was used for imaging. To further minimize the electron beam damage to the sample, the electron beam was blanked immediately after the voltage was applied, and was re-turned on 10 min later to take the HRTEM images. It was found that below the a-C coating layer, a thin layer of $LiFePO_4$ was already formed on the surface of $FePO_4$ due to lithium insertion (Figure 6.7a). A clear phase boundary (pointed out by the red arrows in Figure 6.7a), as evidenced by the image contrast and the misfit strain near the phase boundary, was developed between $FePO_4$ and $LiFePO_4$ due to lithium ion insertion. After 176 s, a thicker $LiFePO_4$ layer (pointed out by red arrows in Figure 6.7b) was developed. The phase boundary migrated from the surface inward the core as more lithium ions were inserted into the $FePO_4$ (Figure 6.8).

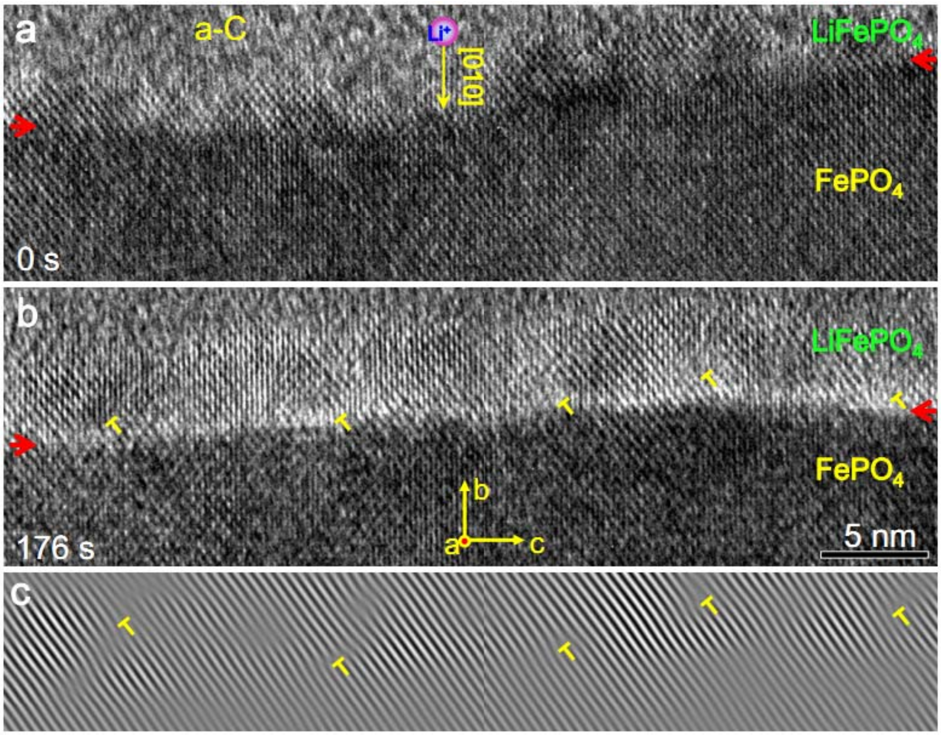

Figure 6.7. Migration of phase boundary between $FePO_4$ and $LiFePO_4$ along the [010] direction during lithiation. (a) After re-turning on the electron beam, a clear phase boundary between $FePO_4$ and $LiFePO_4$ was already developed due to lithiation, as pointed out by the red arrows. A layer of 10 nm amorphous carbon (a-C) was deposited on the surface of $FePO_4$ crystal to decrease the electron beam induced damage. (b) At 176 s, the thickness of the $LiFePO_4$ layer increased. The phase boundary was pointed out by the red arrows. The invert “T” marks mismatch dislocations at the phase boundary. (c) Inverse FFT (IFFT) image of (b), showing the distribution of mismatch dislocations near the phase boundary.

The phase boundary was clearly a sharp interface (Figure 6.7a & b), which is consistent with the electron energy loss spectroscopy (EELS) study reported by Laffont *et al*. [12] in which the phase boundary was shown to be the juxtaposition of $FePO_4$ and $LiFePO_4$ rather than a solid solution region with a concentration gradient. The phase transformation from $FePO_4$ to $LiFePO_4$ induces nearly periodic array of dislocations on the $FePO_4$ side at the phase boundary, as outlined by the inverted “T” in Figure 6.7b & c.

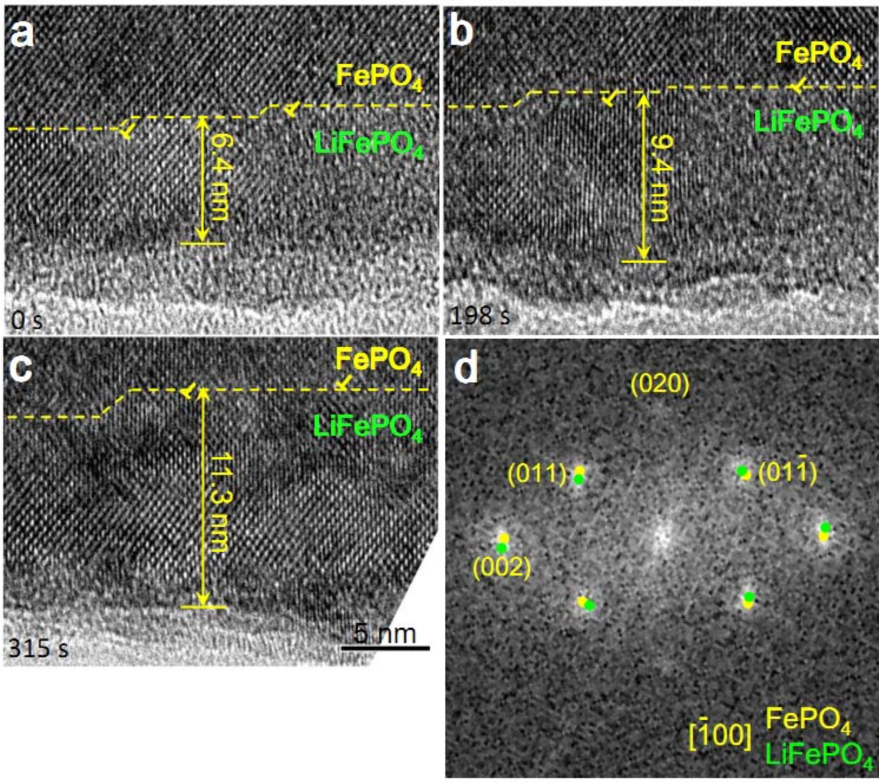

Figure 6.8. The sequential images showing the thickness of $LiFePO_4$ increased from 6.4 nm to 11.3 nm during further *in situ* lithiation of $FePO_4$ particle presented in Fig. 6.7. (a-c) Some dislocations are observed at the $LiFePO_4/FePO_4$ phase boundary. (d) The FFT pattern obtained from $LiFePO_4/FePO_4$ zone shows two sets of FFT patterns.

Detailed analyses of the HRTEM images (see Appendix B for data processing procedure of HRTEM images) indicated that the phase boundary was nearly parallel to the *ac* plane, and it migrated along the *b*-axis inward. It is worth noting that although the $FePO_4$ crystal was connected with Li_2O solid electrolyte on the left edge where *ab* face was exposed (Figure 6.6b), the lithium ion insertion did not occur along the *c*-axis but along the *b*-axis which is far away from the lithium source, indicating that lithium ion was inserted into $FePO_4$ only along the *b*-axis of $FePO_4$ crystal, probably after transported via surface diffusion. The one-dimensional lithiation mechanism along the [010] direction (*b*-axis) is in accordance with theoretical calculations [7-9]. Therefore, our *in situ* HRTEM observation provides the first direct evidence for the anisotropic lithiation mechanism in $FePO_4$.

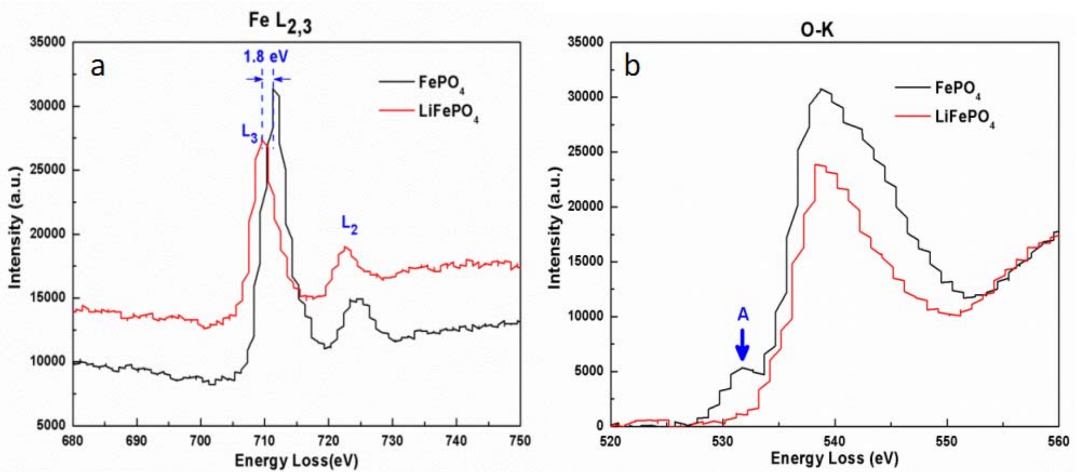

Figure 6.9. EELS results for the particle shown in Figure 6.7. (a) Fe-$L_{2,3}$, and (b) O-K edge spectra of pristine $FePO_4$ and $LiFePO_4$ generated by *in situ* lithiation.

EELS characterization was performed on both the pristine $FePO_4$ and the $LiFePO_4$ generated by *in situ* lithiation for the particle in Figure 6.7. Figure 6.9 shows the EELS results for the Fe-$L_{2,3}$ (Figure 6.9a) and the O-K (Figure 6.9b) edge spectra of the pristine $FePO_4$ and the $LiFePO_4$ generated by *in situ* lithiation in Figure 6.8c. For the Fe-$L_{2,3}$ spectra (Figure 6.9a), strong L_3 and L_2 lines were observed and the maxima of L_3 and L_2 lines were separted by about 12 eV, which is consistent with literature [12]. Peak shifts about 1.8 eV have also been observed at the maximum of the Fe-L_3 line between $FePO_4$ and $LiFePO_4$ which is a charateristic behavior of changed Fe valence state [12]. The O-K edge (Figure 6.9b) for pristine $FePO_4$ shows a clear initial peak (marked as A in Figure 6.9b), whereas $LiFePO_4$ with Fe^{2+} is lack of this feature. Our O-K edge spectra for $FePO_4$ and $LiFePO_4$ are consistent with the results reported in literature. According to literature [12], this A peak indicates the valence state of iron in $LiFePO_4$/$FePO_4$ system. Both Fe-$L_{2,3}$ and O-K edge spectra confirm that the lithiated phase is $LiFePO_4$ and the observed phase boundary is the $LiFePO_4$/$FePO_4$ phase boundary.

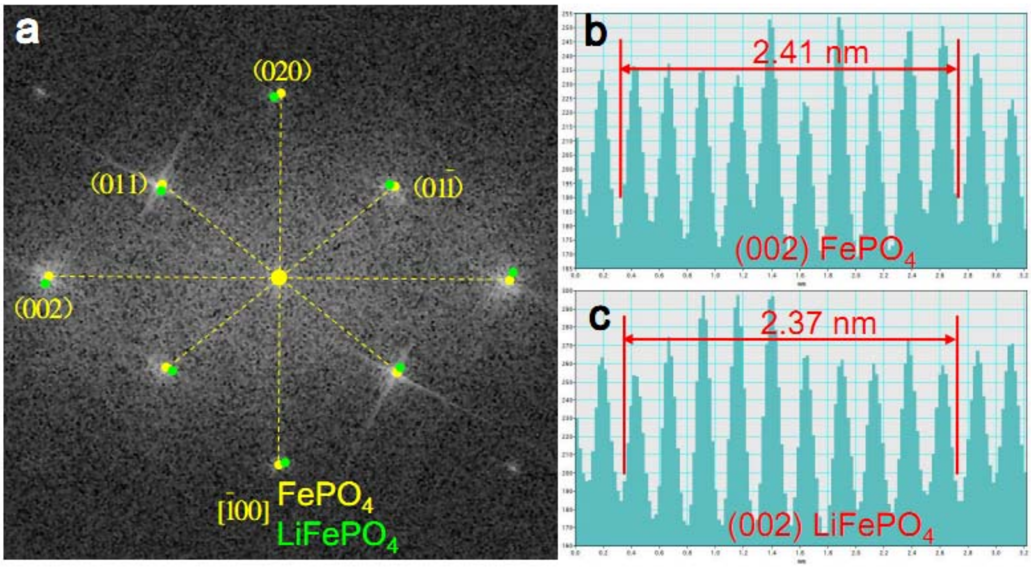

Figure 6.10. (a) The FFT patterns of $FePO_4$ and $LiFePO_4$ produced from $FePO_4$ and $LiFePO_4$ regions in (b). To make comparison, FFT pattern of $LiFePO_4$ (green) was overlaid with that of $FePO_4$ (yellow). (b-c) Lattice spacing of (002) plane from $FePO_4$ and $LiFePO_4$ was measured from HRTEM image shown in (b), showing the lattice spacing of (002) plane decreased about 1.7% after lithium ion insertion into $FePO_4$.

Figure 6.10a presents the superimposed Fast Fourier Transformation (FFT) patterns of $FePO_4$ (yellow dots) and $LiFePO_4$ (green dots) produced from the HRTEM image (Figure 6.7b). Obviously, after lithiation, the orientation of newly formed $LiFePO_4$ slightly rotated comparing with $FePO_4$, which was also observed by Chen *et al.* [10] in chemically delithiated $Li_{0.5}FePO_4$ using *ex situ* HRTEM. This may be attributed to inhomogeneous elastic deformation of the particle to accommodate the transformation strain. Also, as shown in Figure 6.10b & c, after $FePO_4$ was transformed into $LiFePO_4$, the lattice spacing of the (002) plane decreased about 1.7%, which is close to the theoretically expected lattice difference between $FePO_4$ and $LiFePO_4$ in this direction, i.e. 1.9%. If the phase boundary was fully coherent, the lattice constant near phase boundary should be quite different from the stress-free lattice constant of the particular phase, and should approach the mean of the two phases. The fact that the measured lattice constants are quite close to the stress-free lattice constants means majority of the elastic misfit energy along this direction has indeed been relaxed away, due to the presence of the misfit dislocations.

The phase boundary migration mechanism is repeatable in our experiments. Figure 6.11 are the HRTEM images showing the phase boundary migration in another $FePO_4$ single-crystal during lithiation. A positive voltage of 2.7 V versus lithium metal was applied to the $FePO_4$ crystal. The pristine $FePO_4$ crystal had a uniform thickness (Figure 6.11a) and was coated with a thin layer of a-C (Figure 6.11b). After lithiation for 215 s, a phase boundary on the (020) plane with few steps was formed between $FePO_4$ and $LiFePO_4$, as marked by the yellow dashed line in Figure 6.11c, and the lithium ion insertion direction was also [010] direction (b-axis). After another 67 s, the thickness of the $LiFePO_4$ layer increased as the step-like phase boundary propagating along the [010] direction (Figure 6.11d), and it was found that these steps moved along the [010] direction by simply following the movement of phase boundary. Figure 6.11e presents the inverse FFT (IFFT) image from the rectangle area, marked by red dashed line in Figure 6.11d, showing the mismatch dislocations at the phase boundary, which is similar to the results shown in Figure 6.7c.

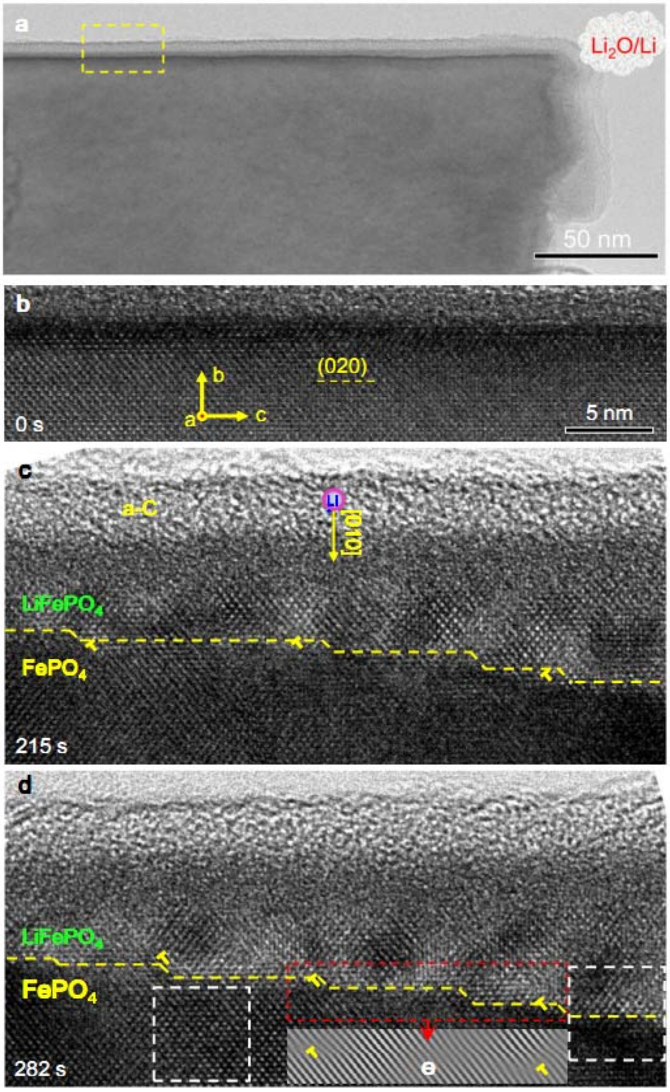

Figure 6.11. Step-like phase boundary between $FePO_4$ and $LiFePO_4$ and its migration along the [010] direction during lithiation. (a) The pristine carbon-coated $FePO_4$ sub-micron particle with no crack and

uniform thickness, as demonstrated by the uniform contrast. The yellow dashed line marked the region, where the HRTEM images were taken. (b) A HRTEM image of the pristine $FePO_4$ in [$\bar{1}00$] zone axis. The crystal orientation and (020) plane were denoted. (c) At 215 s after applying the voltage, a step-like phase boundary was formed between $FePO_4$ and $LiFePO_4$, as pointed out by the yellow dashed line. (d) At 282 s, the thickness of the $LiFePO_4$ layer increased as the step-like phase boundary propagating along the [010] direction. The regions, marked by white dashed lines, show where we took the FFT patterns for $LiFePO_4$ and $FePO_4$ phases. The inset image shows Fig. 3d. (e) Inset of (d) with inverse FFT (IFFT) image from the rectangle zone marked by red dashed line in (d), showing the lattice mismatch induced dislocations at the phase boundary between $FePO_4$ and $LiFePO_4$.

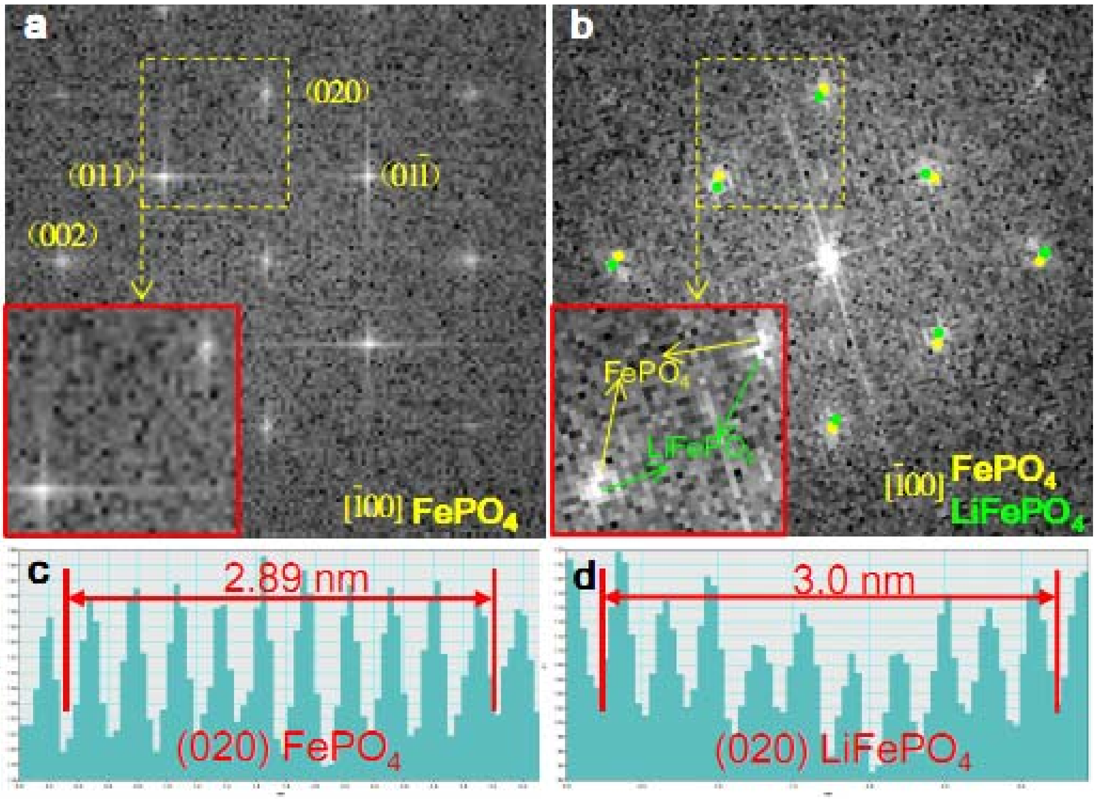

Figure 6.12. (a) The FFT pattern of $FePO_4$ side showing sharp single spots at each diffraction points. The inset image shows that each diffraction spots do have one point. (b) The FFT pattern of the $LiFePO_4/FePO_4$ co-existing zone. Two sets of diffraction patterns are identified to be $LiFePO_4$ and $FePO_4$, respectively. The inset image shows that each diffraction spots do split into two points. (c,d) Lattice spacing of (020) plane for $FePO_4$ and $LiFePO_4$.

The FFT patterns, from both the single-phase $FePO_4$ and the two-phase $FePO_4/LiFePO_4$ regions marked by white dashed squares in Figure 6.11d, were shown in Figure 6.12a & b, respectively. For the $FePO_4$ region, very sharp single diffraction spots were observed in the pattern (Figure 6.12a and its inset). However, the diffraction spots in the FFT pattern from the two-phase $LiFePO_4/FePO_4$ region were split, showing two sets of FFT patterns (Figure 6.12b and its inset) and diffuse intensity distributions, which is obviously different from the single-phase pattern shown in Figure 6.12a. By measuring the lattice spacing in Figure 6.12b, one set of the FFT pattern was identified as $LiFePO_4$, while the other was from $FePO_4$. As shown in Figure 6.12c & d, after $FePO_4$ was transformed into $LiFePO_4$, the lattice spacing of the (020) plane increased by about 3.8%, which is consistent with the theoretical lattice misfit value (i.e. 3.6%) in this plane. Besides the two particles presented in Figures 6.7 and 6.11, the third $FePO_4$ particle was also studied and showed the similar results (Figure 6.13). These similar results further confirmed that the dynamic phase boundary in the $FePO_4$ microparticles was parallel to the (010) plane, and its propagation direction was along [010]. This is different from the post mortem TEM observation of the (100) inclined phase boundaries [10].

The theoretical misfit strains along *a*, *b* and *c* directions between $LiFePO_4$ and $FePO_4$ are $\delta_{[100]} = 5\%$, $\delta_{[010]} = 3.6\%$, and $\delta_{[001]} = -1.9\%$ [23], respectively. It is obvious that *a*-axis misfit contributes the most to the elastic misfit strain, which unfortunately we were not able to observe due to the zone axis condition in imaging. However, the dislocation nucleation is so favorable, as shown in Figures 6.7 and 6.12, that at room temperature even a small misfit strain of 1.9% can drive it. This implies that the larger misfit strain of 5.0% in *a*-axis, which ought to give larger driving force for dislocation nucleation, should sustain significant coherency loss efficiently as well. In Figure 6.7b, we count 5 misfit dislocations over a length of ~ 45 nm along the *c*-axis. The Burgers vector was identified to be [011]/2 (Figure 6.13d). So the contribution to *c*-axis misfit displacement per dislocation was 4.7Å/2=2.35Å, and five dislocations would contribute 2.35Å×5 = 11.75 Å of inelastic accommodation in *c*-axis with 11.75 Å / 45nm = 2.6%, which is very close to the theoretical mismatch of 1.9% in *c*-axis,

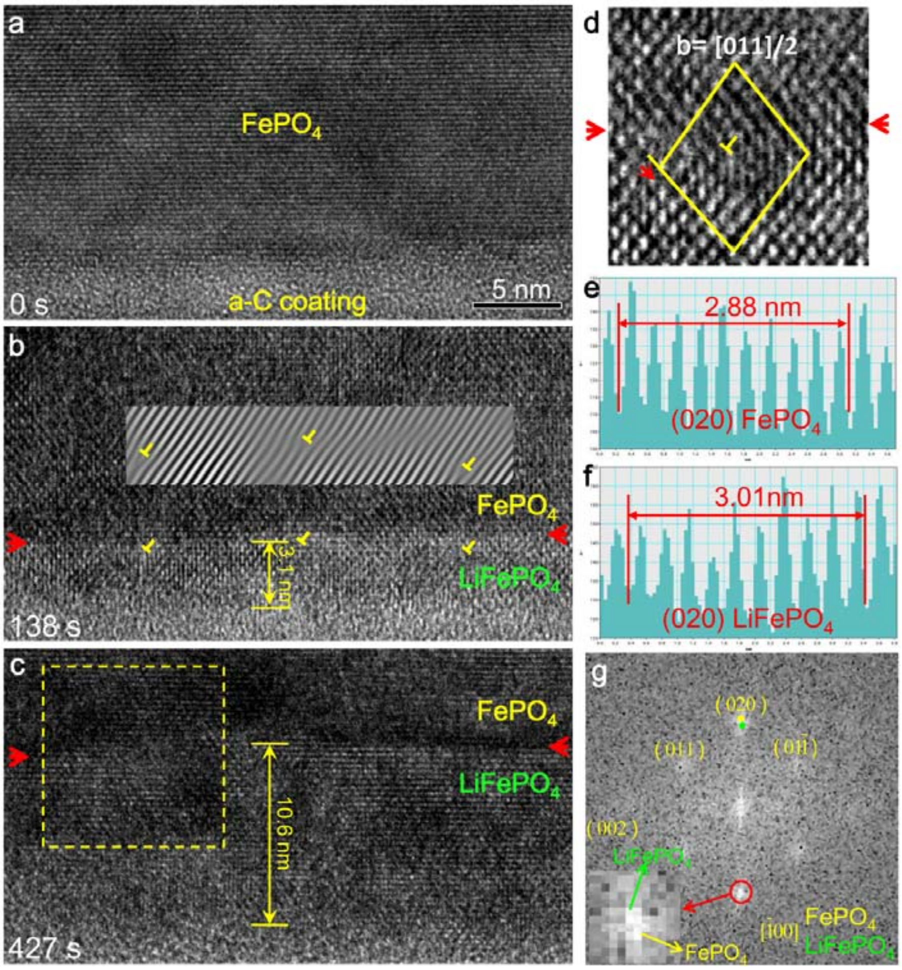

Figure 6.13. Migration of phase boundary between $FePO_4$ and $LiFePO_4$ along the [010] direction during lithiation. (a) The pristine $FePO_4$ with a-C coating. (b) At 138 s, 3.1 nm $LiFePO_4$ was developed due to lithiation. A clear phase boundary between $FePO_4$ and $LiFePO_4$ was formed, as pointed out by

the red arrows. The misfit dislocations were uniformly distributed near the phase boundary between $FePO_4$ and $LiFePO_4$, as marked out by the reversed “T”. The insert is the IFFT showing the dislocations at the phase boundary. (c) At 427 s, the thickness of $LiFePO_4$ layer increased to 10.6 nm. The phase boundary moved along [010] direction, which is perpendicular to the [020] plane. (d) The Burger’s vector of mismatch dislocation are identified to be [011]/2. (e,f) Lattice spacing of (020) plane for $FePO_4$ and $LiFePO_4$ respectively, which was measured from HRTEM image shown in (c). The lattice spacing of (020) plane increased about 4.2% after lithium ion insertion into $FePO_4$. (g) The FFT patterns produced from $FePO_4$ and $LiFePO_4$ regions marked by yellow dashed line in (c). Clearly, the spots of (020) plane split into two spots at each diffraction point. Note: a positive voltage of 2.5 V versus lithium metal was applied to the $FePO_4$ crystal.

given the statistical sampling errors in a small view field. Thus, the system is able to generate just the right density of dislocations to nearly entirely cancel out the misfit elasticity strain in *c*-axis. Dislocation nucleation was apparently facile in this system, which enables the coherency loss. Dislocation migration was also sustainable, since the dislocations appeared to follow the motion of the chemical interface (Figure 6.8). Previous theoretical models [13,15] assumed that the differences in lattice constant between $LiFePO_4$ and $FePO_4$ are entirely taken up as elastic strain energy when phase transformation happens, giving rise to local stress as high as ~1 GPa. Such a high stress may couple into lithium migration and give rise to interesting physical effects such as exceedingly fast phase boundary migration in nanosized $LiFePO_4$ [13]. However, our in situ experiment reveals that, at least for particles with facile generation of misfit dislocations, the elastic strain energy term should be greatly reduced. Facile generation of misfit dislocations should favor the particle to be a two-phase mixture with a sharp interface between $Li_{1-x}FePO_4$ and Li_xFePO_4 ($x \sim 0$) phases, rather than as a single-phase solid solution (no solubility gap), since the elastic coherency energy closes up the spinodal gap and delays or prevents the onset of concentration wave instability of supersaturated homogenous solid solution [19]. While the coherency loss caused by misfit dislocations favors the $LiFePO_4/FePO_4$ two-phase transition mechanism, it also has a significant effect on the phase boundary orientation. As recently suggested by Cogswell *et al*. [24] through a fully anisotropic analysis, a fully coherent phase boundary between $LiFePO_4$ and $FePO_4$ would align on the (101) plane which was shown to be the lowest energy orientation. The observed (100) phase boundary by ex situ HRTEM [10] was attributed to a partial loss of coherency along *c*-axis. In our study, the observed (010) phase boundary is a consequence of even more severe coherency loss. Also, in reference to Tang *et al.*'s lithiation model [16, 25], while a high overpotential may override the thermodynamic consideration of strain energy and rotates the (100) inclined phase boundary towards kinetics-controlled (010) inclination, introducing the misfit dislocations would serve a similar purpose, by reducing the strain energy itself.

While the introduction of misfit dislocations has significant impacts on the thermodynamics of Li_xFePO_4 ($0 < x < 1$) system, it also influences the kinetic processes of phase transformation. First, the coherent phase boundary to semicoherent phase boundary transition is itself a thermally activated, size-dependent process with possibility of hysteresis, and depends sensitively on "extrinsic" or processing-dependent factors such as crystalline quality of the particle, confinement of nearby particles and binder, etc., which are not necessarily just functions of the particle size. Second, while the presence of misfit dislocations reduces the total energy of system, they also "pin" the chemical interface, in the sense that they need to co-move with the advancing chemical front by climbing, which is another thermally activated dissipative process that is generally quite slower than a coherent displacive process [13].

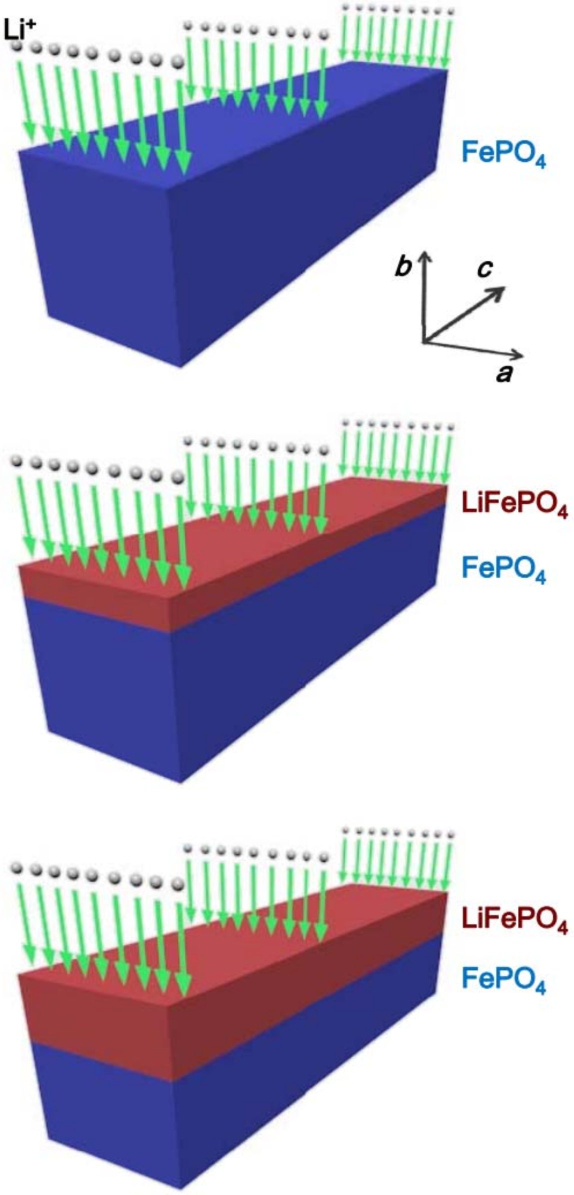

Figure 6.14. Schematic illustrations of lithiation mechanism discovered in this study. The migration direction of the phase boundary is the same as the lithium ion diffusion direction (i.e. [010] direction), which was observed in this study. The green arrows mark the lithium ion insertion direction.

Figure 6.14 shows the dynamic lithiation mechanism discovered in this study. With lithium ion insertion only along the [010] direction, the reduction of lattice misfit strain energy by dislocations favors the two-phase transition mechanism and changes the phase boundary from the thermodynamics-controlled (100) plane (or (101) plane [24]) to kinetics-controlled (010) plane. Our in situ HRTEM observations provide evidence that microscopic damage in the form of nucleated dislocations accompanies chemical transformations in microparticles. These dislocations are expected to accumulate during electrode cycling, which could form preferential sites for cracking. This is expected to be a general degradation mechanism in Li intercalation compounds. Here, it needs to be emphasized that the $FePO_4$ particles studied here are microsized, so the lithiation mechanism is expected to change when the sample goes down to nanoscale as suggested by recent studies [23, 24, 26, 27]. It has been shown that particle size, as well as electrode nanostructures (such as porous electrode etc.), plays a critical role on determining the phase behavior of Li_xFePO_4 system [18-20, 23, 24, 26-29]. For example, Weichert *et al.* [20] recently studied the phase boundary propagation in a $LiFePO_4$ particle, whose size was much larger than the samples in present study, upon chemical delithiation by *in situ* optical microscopy and the phase boundary was shown to migrate along the [001] direction (*c*-axis), which was clearly different from the previous [10] and present HRTEM results. Also, significant amount of cracks were observed and the formed $FePO_4$ was highly porous. The transformation was shown to be diffusion-limited due to the large length scale [20]. Decreasing the sample size to nanoscale would result in a different regime. Besides the short ion transport length, it has been shown that the lithium ion diffusivity in nanoparticles is much higher than that in the bulk materials [26]. Also, it would be more difficult for dislocations to nucleate in smaller particles [30], and a coherent phase boundary is preferable in nanoparticles. This is supported by previous study in which the 43-nm $LiFePO_4$ particle was shown to have a much higher retained strain than the 113-nm sample when two samples were at the same state-of-charge [23]. The coherency strain also changed the phase diagram in Li_xFePO_4 system [24], specifically, stabilizing the solid solution at relatively low temperature and shrinking the miscibility gap between $FePO_4$ and $LiFePO_4$.

Cycle life and capacity fading of batteries are closely related to the fatigue of electrodes, which is caused by accumulation of microscopic damage defects such as dislocations during electrochemical cycling, that eventually leads to cracking [10, 30]. We have identified a detailed pathway where dislocations may be generated, due to coherency loss transition during fast lithiation. Since coherency loss is more likely in microsized particles than in nanosized particles, from well-known size effect similar to that of epitaxial thin film growth and alloy precipitation, we can predict that nanosized particles should have better fatigue life. Also, the accumulation of dislocations may lead to amorphization, which was observed in many electrode materials during electrochemical cycling [17]. Recently, solid-state amorphization due to accumulation of dislocations has been directly observed [31, 32].

6.3. Summary

In this Chapter, we investigated the electrochemical lithiation of $FePO_4$ particles by *in situ* high resolution transmission electron microscopy (HRTEM), and the anisotropic lithiation mechanism was directly observed. For the first time and in contrast to the previous post mortem HRTEM observations, a sharp (010) phase boundary between $LiFePO_4$ and $FePO_4$ was observed, which migrated along the [010] direction during lithiation. We attribute this contrast to the competition between the misfit elastic energy, which favors (101) phase boundary or (100) phase boundary, and the kinetic factor of anisotropic diffusion, which favors (010) phase boundary. Furthermore, our *in situ* HRTEM observations revealed misfit dislocation populations on the (010) phase boundary, overthrowing previous model assumption of fully coherent phase boundary. These misfit dislocations not only greatly relax the elastic energy, but also change the kinetics of nucleation and growth, as well as provide a mechanism for long-term lithium ion battery electrode fatigue and failure, due to repeated coherency loss. The accumulation of dislocations during cycling may also lead to solid-state amorphization observed in some electrode materials.

6.4. References

1. A. K. Padhi, K. S. Nanjundaswamy, and J. B. Goodenough, Phospho-olivines as positive-electrode materials for rechargeable lithium batteries. *J. Electrochem. Soc.* **144**, 1188-1194 (1997).
2. S. Y. Chung, J. T. Bloking, and Y. M. Chiang, Electronically conductive phospho-olivines as lithium storage electrodes. *Nat. Mater.* **1**, 123-128 (2002).
3. B. Kang and G. Ceder, Battery materials for ultrafast charging and discharging. *Nature* **458**, 190-193 (2009).
4. X. L. Wu, L. Y. Jiang, F. F. Cao, Y. G. Guo, and L. J. Wan, $LiFePO_4$ nanoparticles embedded in a nanoporous carbon matrix: superior cathode

material for electrochemical energy-storage devices. *Adv. Mater.* **21**, 2710-2714 (2009).

5. V. Srinivasan and J. Newman, Discharge model for the lithium iron-phosphate electrode. *Journal. Electrochem. Soc.* **151**, A1517-A1529 (2004).

6. A. S. Andersson and J. O. Thomas, The source of first-cycle capacity loss in $LiFePO_4$. *J. Power Sources* **97-8**, 498-502 (2001).

7. D. Morgan, A. Van der Ven, and G. Ceder, Li conductivity in Li_xMPO_4 (M = Mn, Fe, Co, Ni) olivine materials. *Electrochem. Solid State Lett.* **7**, A30-A32 (2004).

8. M. S. Islam, D. J. Driscoll, C. A. J. Fisher, and P. R. Slater, Atomic-scale investigation of defects, dopants, and lithium transport in the $LiFePO_4$ olivine-type battery material. *Chem. Mater.* **17**, 5085-5092 (2005).

9. J. L. Allen, T. R. Jow, and J. Wolfenstine, Kinetic study of the electrochemical $FePO_4$ to $LiFePO_4$ phase transition. *Chem. Mater.* **19**, 2108-2111 (2007).

10. G. Y. Chen, X. Y. Song, and T. J. Richardson, Electron microscopy study of the $LiFePO_4$ to $FePO_4$ phase transition. *Electrochem. Solid State Lett.* **9**, A295-A298, (2006).

11. C. V. Ramana, A. Mauger, F. Gendron, C. M. Julien, and K. Zaghib, Study of the Li-insertion/extraction process in $LiFePO_4$/$FePO_4$. *J. Power Sources* **187**, 555-564 (2009).

12. L. Laffont *et al.*, Study of the $LiFePO_4/FePO_4$ two-phase system by high-resolution electron energy loss spectroscopy. *Chem. Mater.* **18**, 5520-5529 (2006).

13. C. Delmas, M. Maccario, L. Croguennec, F. Le Cras, and F. Weill, Lithium deintercalation in $LiFePO_4$ nanoparticles via a domino-cascade model. *Nat. Mater.* **7**, 665-671 (2008).

14. G. K. Singh, G. Ceder, and M. Z. Bazant, Intercalation dynamics in rechargeable battery materials: General theory and phase-transformation waves in $LiFePO_4$. *Electrochim. Acta* **53**, 7599-7613 (2008).

15. M. Tang, J. F. Belak, and M. R. Dorr, Anisotropic phase boundary morphology in nanoscale olivine electrode particles. *J. Phys. Chem. C* **115**, 4922-4926 (2011).

16. Y. M. Chiang, Building a better battery. *Science* **330**, 1485-1486 (2010).

17. Y. H. Kao *et al.*, Overpotential-dependent phase transformation pathways in lithium iron phosphate battery electrodes. *Chem. Mat.* **22**, 5845-5855 (2010).

18. R. Malik, F. Zhou, and G. Ceder, Kinetics of non-equilibrium lithium incorporation in $LiFePO_4$. *Nat. Mater.* **10**, 587-590 (2011).

19. P. Bai, D. A. Cogswell, and M. Z. Bazant, Suppression of phase separation in $LiFePO_4$ nanoparticles during battery discharge. *Nano Lett.* **11**, 4890-4896 (2011).

20. K. Weichert *et al.* Phase boundary propagation in large $LiFePO_4$ single crystals on delithiation. *J. Am. Chem. Soc.* **134**, 2988-2992 (2012).

21. X. H. Liu *et al.,* Anisotropic swelling and fracture of silicon nanowires during lithiation. *Nano Lett.* **11**, 3312-3318 (2011).

22. X. H. Liu *et al.,* In situ TEM experiments of electrochemical lithiation and delithiation of individual nanostructures. *Adv. Energy Mater.* **2**, 722-741 (2012).

23. N. Meethong, H. Y. S. Huang, S. A. Speakman, W. C. Carter, and Y. M. Chiang, Strain accommodation during phase transformations in olivine-based cathodes as a materials selection criterion for high-power rechargeable batteries. *Adv. Funct. Mater.* **17**, 1115-1123 (2007).

24. D. A. Cogswell and M. Z. Bazant, Coherency strain and the kinetics of phase separation in $LiFePO_4$ nanoparticles. *ACS Nano* **6**, 2215-2225 (2012).

25. M. Tang, W. C. Carter, J. F. Belak, and Y. M. Chiang, Modeling the competing phase transition pathways in nanoscale olivine electrodes. *Electrochim. Acta* **56**, 969-976 (2010).

26. R. Malik, D. Burch, M. Z. Bazant, and G. Ceder, Particle size dependence of the ionic diffusivity. *Nano Lett.* **10**, 4123-4127 (2010).

27. M. Bazant, Phase-field theory of ion intercalation kinetics. arXiv:1208.1587v1.

28. P. Gibot *et al.* Room-temperature single-phase Li insertion/extraction in nanoscale Li_xFePO_4. *Nat. Mater.* **7**, 741-747 (2008).

29. T. R. Ferguson and M. Bazant, Nonequilibrium thermodynamics of porous electrodes. arXiv:1204.2934v2.

30. T. Zhu and J. Li, Ultra-strength materials. *Prog. Mater. Sci.* **55**, 710-757 (2010).

31. J. Y. Huang *et al.* In situ observation of the electrochemical lithiation of a single SnO_2 nanowire electrode. *Science* **330**, 1515-1520 (2010).

32. S. W. Nam *et al.* Electrical wind force-driven and dislocation-templated amorphization in phase-change nanowires. *Science* **336**, 1561-1566 (2012).

Chapter 7: Summary and Future Plans

7.1. Summary

The major contributions of this dissertation are summarized as follow:

1. A mixed-control phase transformation model has been proposed to describe the charge/discharge process for phase transformation electrode materials in Li-ion batteries. This model considers the effect of misfit strain induced accommodation energy on the phase transformation. The mixed-control model provides a new opportunity to discover the fundamental principles that govern the electrochemical performance of phase transformation electrode materials, which are essential for exploration of next generation of high power batteries.
2. The equilibrium potential hysteresis of $LiFePO_4$ in the phase transformation region is determined by using the GITT method, and the corresponding accommodation energy is calculated according to the potential hysteresis. The $LiFePO_4$ with small particle size is found to have low accommodation energy during lithiation and delithiation.
3. The $LiFePO_4$ is found to behave like a solid solution inside the potential hysteresis region, and a reliable EIS test is suggested to be obtained at the center of potential hysteresis.
4. The mixed-control model is integrated with GITT, PITT and CV. The chemical diffusion coefficients in two-phase region of phase transformation electrode materials are precisely determined, and for the first time, the interface mobility of phase transformation electrode materials is obtained.

5. From our *in situ* HRTEM experiments, we show the first real-time atomic-scale observation of anisotropic lithiation mechanism in $FePO_4$, which was shown to take place only along the *b*-axis of orthorhombic $FePO_4$ single-crystals.
6. Our results show the first direct evidence that there exists a phase boundary between the lithiated and the non-lithiated phases during dynamic lithiation, and the phase transformation is governed by the phase boundary migration along the *ac* plane. The phase boundary is shown to be semi-coherent shape interface which is the juxtaposition of $FePO_4$ and $LiFePO_4$ rather than previously reported solid solution region.
7. Lattice misfit at the phase boundary, which is manifested by the presence of nearly periodic dislocations on the $FePO_4$ side at the phase boundary, was observed and shown to significantly slow down the phase boundary movement.
8. Although this research focuses on Li-ion storage electrode materials, the knowledge created here is of fundamental importance for a broad range of applications, including hydrogen, sodium and magnesium storage materials.

7.2. Future Research

To further improve the mixed-control model and investigate the delithiation/lithiation mechanisms of phase transformation electrode materials by *in situ* HRTEM, some important issues related to present research are proposed as follow:

7.2.1. Integration of Mixed-Control Model with EIS

We have integrated the mixed-control model with GITT, PITT and CV. Compared to these electrochemical techniques, EIS is more powerful since it can separate different resistances (electrolyte resistance, electrolyte interface resistance, diffusion resistance and/or phase transition resistance) according to their different response time scales. Similar to GITT, the calculation of diffusion coefficient with EIS needs the information of d$E(x)$/dx, but the theoretical value of $dE(x)/dx$ is zero in the two-phase region, so, the Li-ion diffusion coefficient cannot be directly determined by EIS according to Eq. (1.4). In addition, a reliable EIS can be obtained only if the system satisfies the criteria of linearity and time invariance (LTI) [1], but phase transformation is not a linear behavior because of the existence of an intrinsic potential hysteresis in the first-order phase transformation, and the nonlinearity makes the low-frequency-response of the impedance spectroscopy unstable.

It is well-known that $Li_4Ti_5O_{12}$ undergoes a first-order phase transformation under charge/discharge, which is similar to $LiFePO_4$. The uniqueness of $Li_4Ti_5O_{12}$ is that the lattice parameters for the two phases during the phase transformation are almost the same, which makes the charge and discharge equilibrium potentials of $Li_4Ti_5O_{12}$ show almost no hysteresis. So, $Li_4Ti_5O_{12}$ electrode can be used to develop the mixed-control integrated EIS. If EIS is measured at the open-circuit of the phase transformation region for $Li_4Ti_5O_{12}$, the phase transformation will occur in both the forward and backward potential scans, which make the system linear and time invariance.

7.2.2. *In situ* HRTEM Study of Delithiation/Lithiation Processes in Nanosized $LiFePO_4$

As shown in Chapter 6, we have studied the lithiation mechanism of $FePO_4$ microparticles. However, recent experiments [2, 3] and simulations [4, 5] have shown that when the size of $LiFePO_4$ goes down to nanoscale, the lithiation/delithiation mechanism is supposed to be completely different from that in the microsized particle. Although the rate performance of nano-$LiFePO_4$ has been greatly improved, the delithiaion/lithiation mechanism in nano-$LiFePO_4$ seems to be still very unclear so far. The lattice misfit induced strain energy scales with the reciprocal of the sample size. This indicates that, under certain critical particle size, when the energy of de-mixing is smaller than the strain energy, phase transition is not thermodynamically favorable and the delithiation/lithiation processes might follow a complete solid solution pathway, which has been proposed by Gibot *et al* [3]. Kinetically, the lithium ion diffusivity has been predicted to be much higher in nano-$LiFePO_4$ than that in the bulk materials [6]. So, a systematic investigation of delithiation/lithiation in nano-$LiFePO_4$ is critical.

We have synthesized nano-$LiFePO_4$ from a solvothermal method (Figure 7.1a and b). The experiment setup is proposed in Figure 7.1c. The major challenge of this part is to capture the real-time microstructure changes during the delithiation/lithiation reaction. Since the volume change of $LiFePO_4$ is very small, it is hard to know if any lithium is extracted from the material. Here, we propose to use LiAlSiO-coated Si as the counter electrode material. Since the volume change of Si upon lithiation is very large (~400%), it can be served as a sensor. This kind of setup makes sure we can capture the microstructure change at real time. Moreover, since the setup shown in Figure 7.1c consists of a full cell, we can observe the microstructure changes for both cathode and anode at the same time.

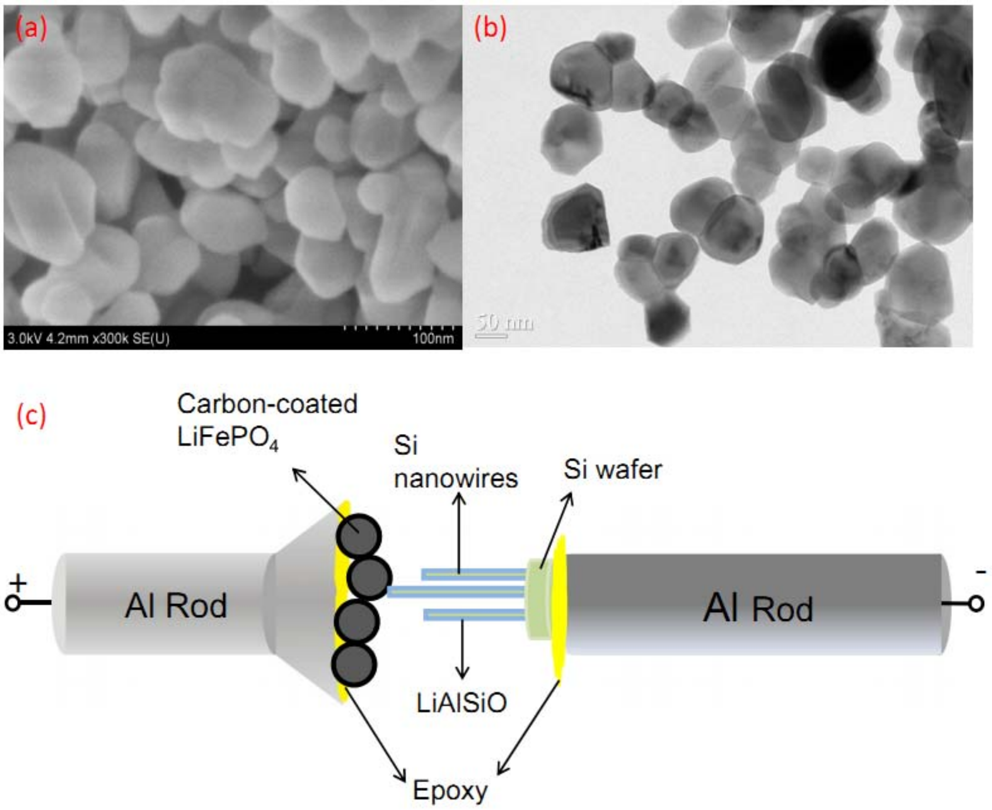

Figure 7.1. (a) SEM image of nano-$LiFePO_4$, (b) TEM image of nano-$LiFePO_4$, and (c) setup of *in situ* HRTEM experiment.

7.2.3. Application of Mixed-Control Model Integrated Techniques on Electrode Materials with Different Volume Changes

We have applied the mixed-control model integrated electrochemical techniques to analyze the $LiFePO_4$ electrode. To further improve the mixed-control model, electrode materials with different volume changes upon charge/discharge should be studied with the mixed-control model integrated electrochemical techniques. To make a reasonable comparison, the host material is kept with $FePO_4$, but the insertion ion is changed from lithium ion to sodium ion which has a larger radius than lithium ion and ought to give a larger volume change of $FePO_4$ upon discharge.

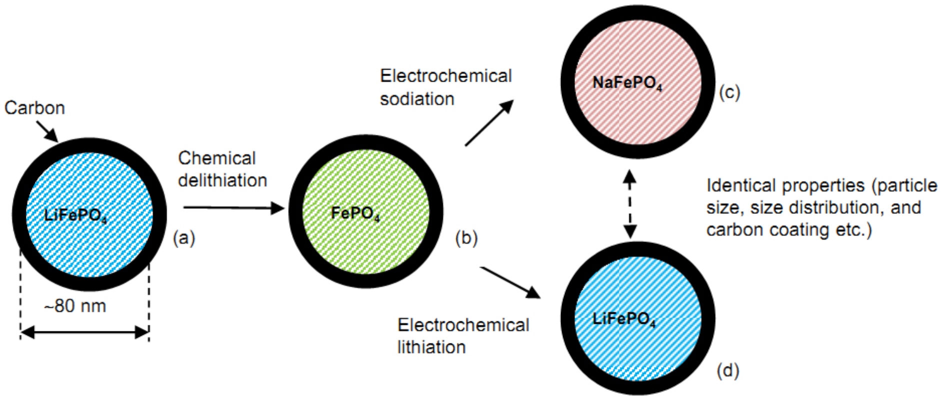

Figure 7.2. Illustration of synthesis process for C-$LiFePO_4$ and C-$NaFePO_4$ with identical properties.

Figure 7.2 shows the synthesis process of materials. Carbon-coated $LiFePO_4$ (C-LiFePO4) is synthesized from a solvothermal method followed by carbon coating with sucrose. Then, C-$LiFePO_4$ is delithiated to form carbon-coated FePO4 (C-$FePO_4$). Finally, C-$FePO_4$ is used in both Li-ion batteries and Na-ion batteries to electrochemically form C-$LiFePO_4$ and C-$NaFePO_4$, which guarantees the identical properties between $NaFePO_4$ and $LiFePO_4$ electrodes. The mixed-control model can be used to analyze and compare the effect of volume change on the interface mobility and performance of the electrode materials.

7.3. References

1. McC Siebert, W. *Circuits, Signals and System;,* The MIT Press and McGraw-Hill Book Company, New York, **1986**.
2. C. Delmas, M. Maccario, L. Croguennec, F. Le Cras, and F. Weill, Lithium deintercalation in $LiFePO_4$ nanoparticles via a domino-cascade model. *Nat. Mater.* **7**, 665-671 (2008).
3. P. Gibot *et al.* Room-temperature single-phase Li insertion/extraction in nanoscale Li_xFePO_4. *Nat. Mater.* **7**, 741-747 (2008).

4. R. Malik, F. Zhou, and G. Ceder, Kinetics of non-equilibrium lithium incorporation in $LiFePO_4$. *Nat. Mater.* **10**, 587-590 (2011).

5. P. Bai, D. A. Cogswell, and M. Z. Bazant, Suppression of phase separation in $LiFePO_4$ nanoparticles during battery discharge. *Nano Lett.* **11**, 4890-4896 (2011).

6. R. Malik, D. Burch, M. Z. Bazant, and G. Ceder, Particle size dependence of the ionic diffusivity. *Nano Lett.* **10**, 4123-4127 (2010).

Appendix A: Numerical Methods for the Mixed-Control Model under GITT Condition

The numerical approach we used to solve the PDEs is method of lines (MOL). The MOL approach involves two steps, which are:

(1) The boundary condition is first algebraically approximated by finite difference on a spatial grid.

(2) The resulting ODEs system with initial values in (1) is integrated by a built-in ODE solver in Maple software.

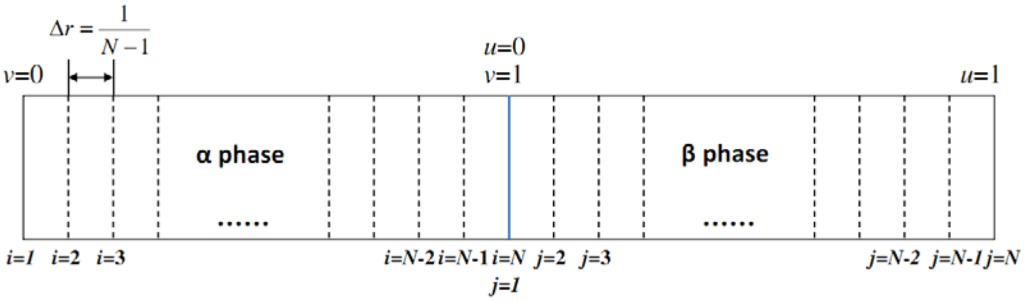

Scheme Al. Discretizing the space co-ordinate by finite difference.

Scheme A1 shows how we discretized the PDEs over space co-ordinate.

For α phase region

The dimensionless form for each parameter is defined as:

$$C_1 = \frac{C_\alpha^{'}}{C_t},\ t_1 = \frac{t}{L^2 / D_\beta},\ l = \frac{x_i(t)}{L} \text{ with } u = \frac{x}{x_i(t)}$$

Eq. (2.36) can be converted into:

$$\frac{\partial C_1}{\partial t_1} = \frac{D_\alpha}{D_\beta} \frac{\partial^2 C_1}{\partial u^2} \frac{1}{l^2} + \frac{\partial C_1}{\partial u} \frac{u}{l} \frac{dl}{dt_1} \tag{A1}$$

As shown in Scheme A1, we discretize the space co-ordinate of *u* at *N* point. For *i*=2, 3… *N*-1, Eq. (A1) becomes

$$\frac{dC_1(i)}{dt_1} = \frac{D_\alpha}{D_\beta}\frac{1}{l^2}\left(\frac{C_1(i+1)-2C_1(i)+C_1(i-1)}{\Delta r^2}\right)+\left(\frac{C_1(i+1)-C_1(i-1)}{2\Delta r}\right)\frac{u}{l}\frac{dl}{dt_1} \qquad \text{(A2)}$$

where $\Delta r = \dfrac{1}{N-1}$

For i=1, the boundary condition Eq. (2.37) becomes

$$\frac{dC_1(1)}{du} = \frac{-3C_1(1)+4C_1(2)-C_1(3)}{2\Delta r} = 0 \qquad \text{(A3)}$$

For $i=N$,

$$\frac{dC_1(N)}{du} = \frac{3C_1(N)-4C_1(N-1)+C_1(N-2)}{2\Delta r} \qquad \text{(A4)}$$

For β phase region

We define $C_2 = \dfrac{C_\beta^{'}}{C_t}$, with $v = \dfrac{x - x_i(t)}{L - x_i(t)}$,

Eq. (2.38) can be converted into

$$\frac{\partial C_2}{\partial t_1} = \frac{\partial^2 C_2}{\partial v^2}\frac{1}{[1-l]^2} + \frac{1-v}{1-l}\frac{\partial C_2}{\partial v}\frac{dl}{dt_1} \qquad \text{(A5)}$$

We discretize the space co-ordinate v at N point. For j=2, 3… N-1, Eq. (A5) becomes

$$\frac{dC_2(i)}{dt_1} = \frac{1}{[1-l]^2}\left(\frac{C_2(i+1)-2C_2(i)+C_2(i-1)}{\Delta r^2}\right)+\left(\frac{C_2(i+1)-C_2(i-1)}{2\Delta r}\right)\frac{1-v}{1-l}\frac{dl}{dt_1} \qquad \text{(A6)}$$

For $j=1$,

$$\frac{dC_2(1)}{dv} = \frac{-3C_2(1)+4C_2(2)-C_2(3)}{2\Delta r} \qquad \text{(A7)}$$

For $j=N$, the boundary condition (Eq. 2.39) becomes

$$\frac{dC_2(N)}{dv} = \frac{3C_2(N)-4C_2(N-1)+C_2(N-2)}{2\Delta r} = -\frac{I\rho L^2}{C_t D_\beta F}(1-l) \qquad \text{(A8)}$$

At the phase boundary, Eq. (2.40) becomes

$$\frac{D_\alpha}{D_\beta}\frac{1}{l}\frac{3C_1(N)-4C_1(N-1)+C_1(N-2)}{2\Delta r}-\frac{1}{1-l}\frac{-3C_2(1)+4C_2(2)-C_2(3)}{2\Delta r}=\left(C_2(1)-C_1(N)\right)\frac{dl}{dt_1} \quad \text{(A9)}$$

After discretizing the PDEs and corresponding boundary conditions over space co-ordinate, the PDEs become a system of ODEs with initial value and the boundary conditions become algebra equations. These differential algebra equations (DAEs) are solved by Maple with a built in DAE solver (Maple code is available upon request). Below, we give an example to show the transient voltage profile calculated with above methods.

The parameters used in the simulation are listed below:

Applied current density: I=0.001 A/g,

The diameter of the particle: L=1 μm

Faraday constant: F=96500 C/mol,

Density of $LiFePO_4$: $\rho=3.6*10^6$ g/m^3,

The maximum concentration of Li that can be incorporated into $FePO_4$:

$C_t=0.02119*10^6$ mol/m^3,

Diffusion coefficient of Li-ion in β phase: $D_\beta=0.48*10^{-16}$ m^2/s,

Diffusion coefficient of Li in α phase: $D_\alpha=6*10^{-16}$ m^2/s,

Interface mobility of phase boundary: $M=10^{-14}$ m mol J^{-1} s^{-1}.

The relationship between accommodation energy and the volume ratio of new phase:

$f(l(t))=-1215.93l(t)^3+2095.80l(t)^2-1429.50l(t)+690.15$.

Expression between Li-ion concentration and equilibrium potential in α and β phase:

$$E_\alpha=-12.03C_1+3.94 \quad \text{(A10)}$$

$$E_\beta=-4.80C_2+7.57 \quad \text{(A11)}$$

The space co-ordinate is discretized with N=22 points.

Potential before applying the constant current: V_0=3.42196 V

The time is calculated from 0 sec to 3600 sec, and the results are shown below.

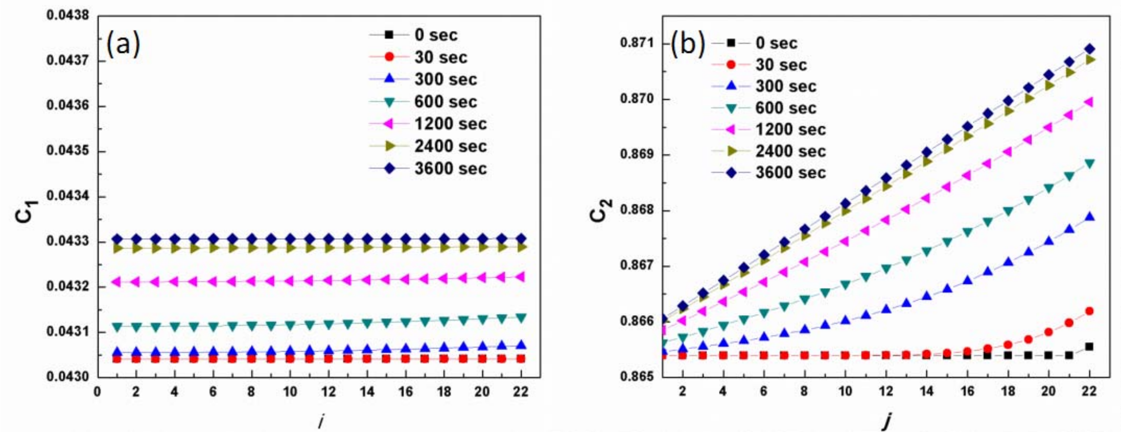

Figure A1. Transient Li-ion concentration at different locations in (a) α phase, and (b) β phase.

Figure A1 shows the transient Li-ion concentration profile at the different discretized points in the α and β phase calculated from about parameters.

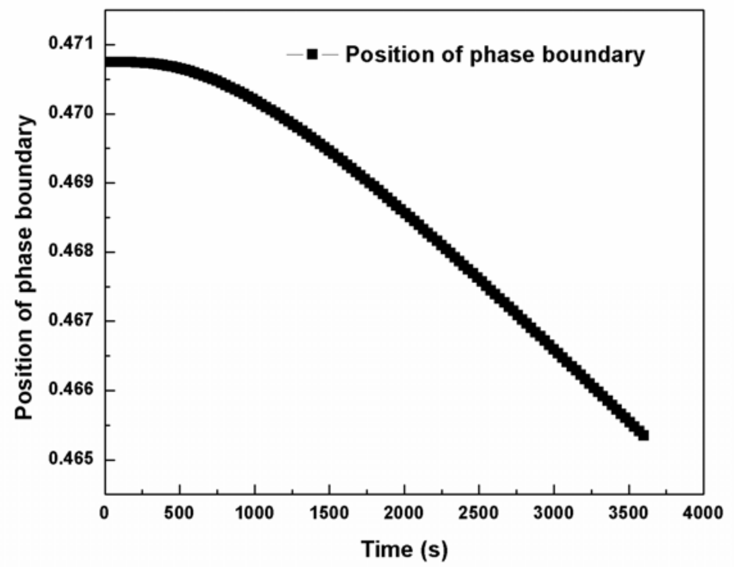

Figure A2. Position of phase boundary during the time of calculation.

Figure A2 shows the position of phase boundary during the time of calculation.

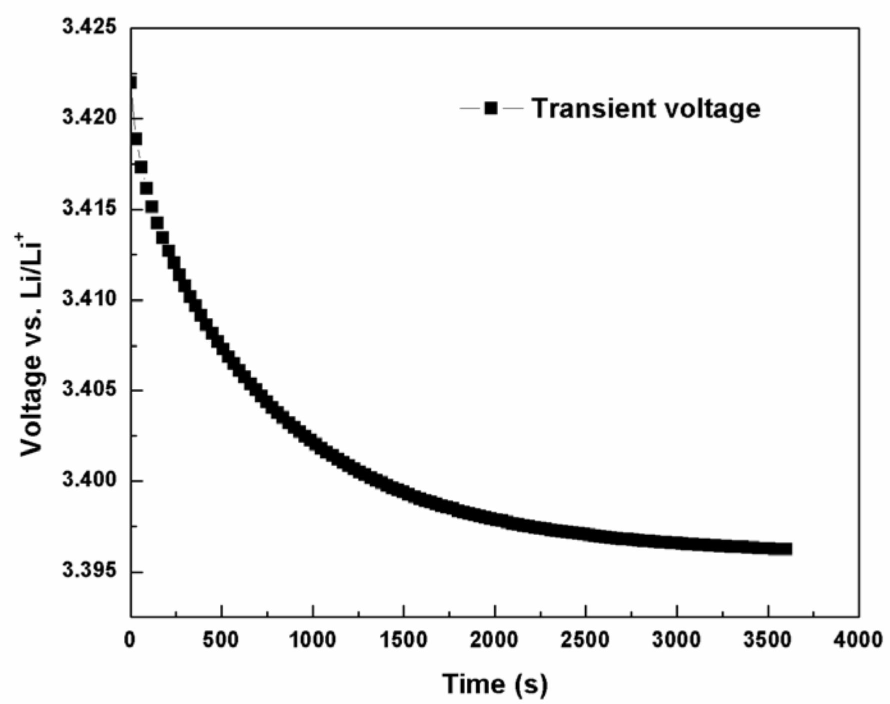

Figure A3. The calculated transient voltage profile.

Figure A3 shows the transient voltage profile which is calculated by plugging in the transient Li-ion concentration at *j*=22 into Eq. (A11)

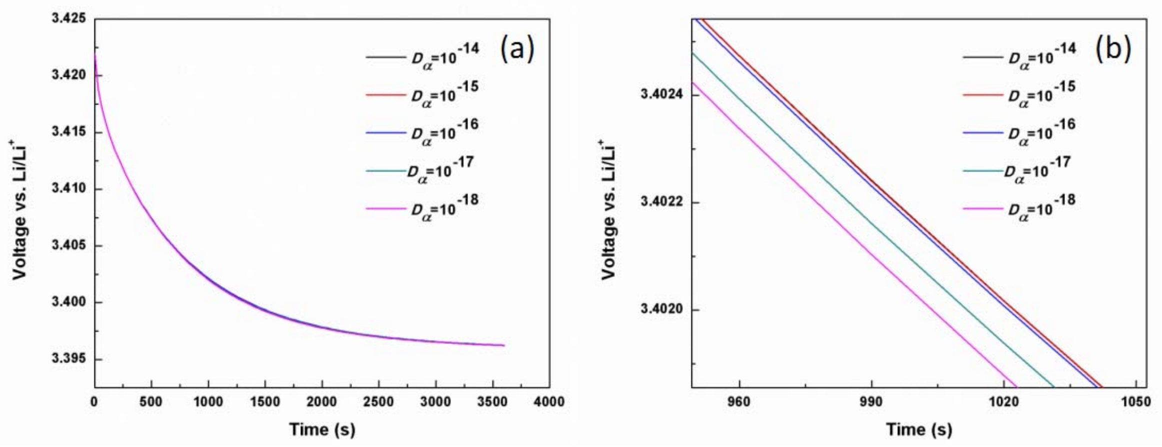

Figure A4. Transient voltage profiles change with D_α. (a) Full scale, and (b) zoomed-in curve.

Figure A4 shows how the resulted voltage profile changes with different values of D_α.

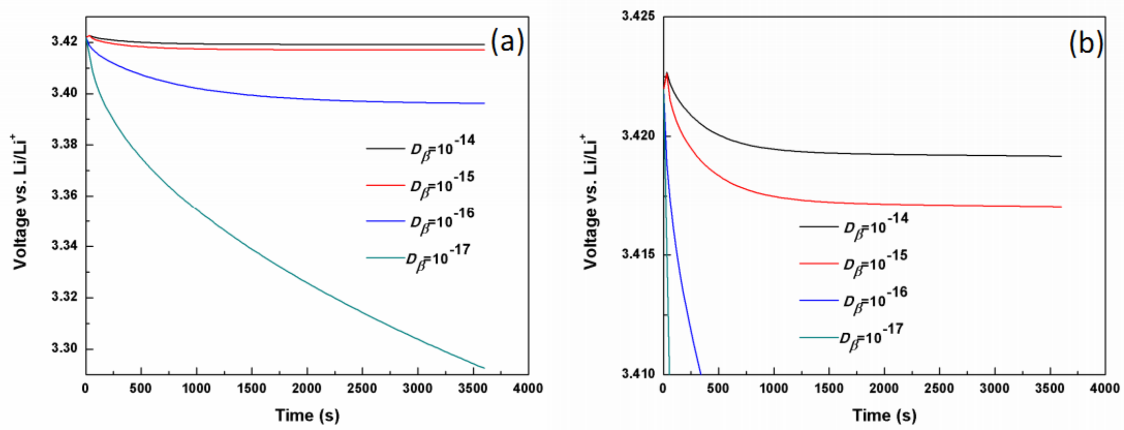

Figure A5. Transient voltage profiles change with D_β. (a) Full scale, and (b) zoomed-in curve.

Figure A5 shows how the resulted voltage profile changes with different values of D_β.

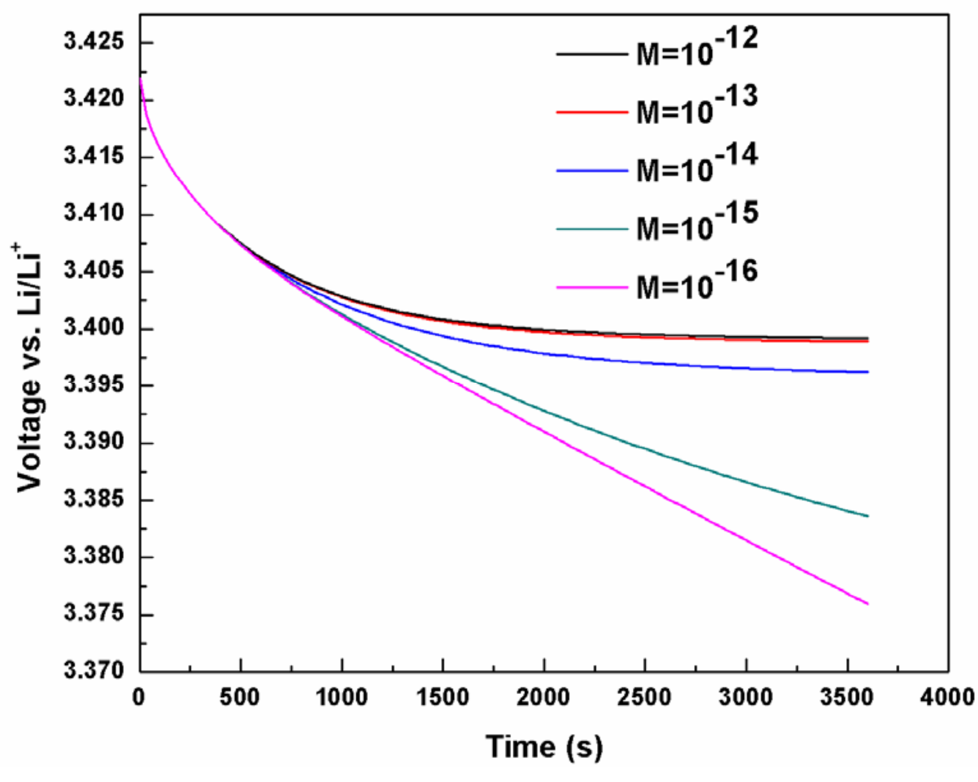

Figure A6. Transient voltage profile changes with different values of interface mobility *M*.

Figure A6 shows how the resulted voltage profile changes with different values of interface mobility *M*.

Appendix B: Data Processing Procedure for HRTEM Images

To make sure what we observed was truly phase boundary rather than some artifacts, we used four measures for confirmation, which are established and also widely used for analysis of HRTEM images about phase boundaries in different materials.

(1) **Contrast difference**. Such contrast difference is usually associated with some changes in the material, such as composition, thickness, orientation with respect to the incident electron beam, or their combinations. Compositional changes can be perceived from very large to very small length scales. At small length scales, as in HRTEM images of a system containing several phases, the contrast is different across the phase boundaries due to the different crystal fields that modulate propagation of the incident electron beam, even on a width of 1 nm such as an atomically sharp interface. When the Li ions insert into an anode material, such as Si [1], a sharp phase boundary is produced and the lithiated part has the brighter contrast. Similar to the case of Li diffusion into $FePO_4$, in the *in situ* heating of Si nanodevices, a sharp phase boundary is created when Ni atoms diffused from the Ni contact-side into the Si nanowires by forming $NiSi_2$ phase [2]. For $LiFePO_4/FePO_4$ system, same contrast difference across the phase boundary has been observed in the *ex situ* experiments [3-5], *i.e.* in which the $LiFePO_4$ region showed a lighter contrast than the $FePO_4$. The contrast difference induced by the atomic weight (i.e., different atomic scattering factors) is also observed in other materials, such as AlAs-GaAs [6] and Al-Pb [7]. The contrast difference tells us the location where a phase boundary may exist.

(2) **Lattice spacing difference between different phases.** The $LiFePO_4/FePO_4$ phase boundary is such a kind of interface that the two phases have almost the same orientation on two sides. However, the spacing difference, despite small, is measurable. This method is also frequently used in the analysis of $LiFePO_4/FePO_4$ two-phase systems [2, 4, 5].

(3) **Fast Fourier Transform (FFT) analysis.** Power spectrum (i.e. FFT pattern) is generated from the HRTEM, which directly visualizes tiny difference of atomic arrangements of the closely related phases. Two sets of diffraction patterns were observed and indexed to $LiFePO_4$ and $FePO_4$, respectively, which confirms that the interface we observed was truly a $LiFePO_4/FePO_4$ phase boundary. The FFT image computer-generated by using the Gatan DigitalMicrograph® software was the general method used to analyze the HRTEM images of $LiFePO_4$ and $FePO_4$ [3-5].

(4) **Misfit dislocations.** The mismatch between $LiFePO_4$ and $FePO_4$ might produce misfit dislocations at the phase boundary, which are shown as the extra half atom planes. Such misfit dislocations are the most important feature for most phase boundaries, such as Al-Pb [7], $SrZrO_3$-$SrTiO_3$ [8] and GaSb-GaAs [9]. For the $LiFePO_4/FePO_4$ system, the well-organized extra half planes show up at the $FePO_4$ side due to the smaller lattice spacing, and such dislocations are distributed at expected densities in agreement with the amount of lattice mismatch of the given interfaces. This corroborates that the interface we observed undoubtedly is the $LiFePO_4/FePO_4$ phase boundary.

References

1. Liu, X. H. & Huang, J. Y. *In situ* TEM electrochemistry of anode materials in lithium ion batteries. *Energy Environ. Sci.* **4,** 3844-3860 (2011).
2. Tang, W., Dayeh, S. A., Picraux, S. T., Huang, J. Y. & Tu, K-N. Ultra-short channel silicon nanowire transistors with nickel silicide source-drain contacts. *Nano Lett. DOI: 10.1021/nl3011676.*
3. Laffont, L. *et al.* Study of the $LiFePO_4/FePO_4$ two-phase system by high-resolution electron energy loss spectroscopy. *Chem. Mater.* **18,** 5520-5529 (2006).
4. Ramana, C. V., Mauger, A., Gendron, F., Julien, C. M. & Zaghib, K. Study of the Li-insertion/extraction process in $LiFePO_4/FePO_4$. *J. Power Sources* **187,** 555-564 (2009).
5. Chen, G. Y., Song, X. Y. & Richardson, T. J. Electron microscopy study of the $LiFePO_4$ to $FePO_4$ phase transition. *Electrochem. Solid State Lett.* **9,** A295-A298 (2006).
6. Braun, W., Trampert, A., Daweritz, L. & Ploog, K. H. Nonuniform segregation of Ga at AlAs/GaAs heterointerfaces. *Phys. Rev. B.* **55**, 1689-1695 (1997).
7. Rosner, H., Weissmuller, J. & Wilde, G. HRTEM observation of misfit dislocations at non-faceted Al-Pb interfaces. *Philosophical Magazine Letters.* **86**, 623–632 (2006).
8. Ernst, F., Recnik, A., Langjahr, P. A., Nellist, P. D. & Ruhle, M. Atomistic structure of misfit dislocations in SrZrO3/SrTiO3 interfaces. *Acta Mater.* **47**, 183-198 (1999).

9. Wang, Y., Ruterana, P., Desplanque, L., Kazzi, S. E. & Wallart, X. Growth mode dependence of misfit dislocation configuration at lattice mismatched Ⅲ-Ⅴ semiconductor interfaces. *EPL*, **97**, 98011P1-P6 (2012).

Publications

Journal Publications

1. **Y. Zhu** and C. Wang, "Strain accommodation and potential hysteresis of $LiFePO_4$ cathodes during Li ion insertion/extraction", *Journal of Power Sources* **2010**, 196, 1442.
2. **Y. Zhu** and C. Wang, "Galvanostatic intermittent titration technique for phase-transformation electrodes", *J. Phys. Chem. C* **2010**, 114, 2830-2841.
3. **Y. Zhu** and C. Wang, "Novel CV for phase transformation electrodes", *J. Phys. Chem. C* **2011**, 115, 823-832.
4. **Y. Zhu,** J. Wang, Y. Liu, X. Liu, A. Kushima, Y. Liu, Y. Xu, S. X. Mao, C. Wang and J. Huang, "*In situ* atomic-scale imaging of phase boundary migration in $FePO_4$ microparticles during electrochemical lithiation", accepted by *Advanced Materials*.
5. **Y. Zhu**, Y. Xu, Y. Liu, C. Luo and C. Wang, "Comparison of electrochemical performance between olivine $NaFePO_4$ in sodium-ion batteries and olivine $LiFePO_4$ in lithium-ion batteries", accepted by *Nanoscale*.
6. **Y. Zhu**, Y. Liu, T. Li, C. Wang and J. Huang, "*In situ* TEM study of particle size effect on the lithiation of Al", in preparation.
7. Y. Xu, **Y. Zhu**, Y. Liu and C. Wang, "Electrochemical performance of porous carbon/tin composite anodes for sodium-ion and lithium-ion batteries" *Advanced Energy Materials*, **2012**, DOI: *10.1002/aenm.201e00346*.
8. Y. Liu, Y. Xu, X. Han, C. Pellegrinelli, **Y. Zhu**, H. Zhu, J. Wan, A. C. Chung, O. Vaaland, C. Wang and L. Hu, "Porous amorphous $FePO_4$ nanoparticles connected

by single-wall carbon nanotubes for sodium ion battery cathodes", *Nano Letters,* **2012**, DOI: 10.1021/nl302819f.

Conference Presentations

1. **Y. Zhu**, J. Wang, Y. Liu, A. Kushima, Y. Liu, J. Li, C. Wang and J. Huang, "*In situ* atomic-scale investigation of electrochemical lithiation in $FePO_4$" (Oral), The 221th ECS meeting, Seattle, WA 2012.
2. **Y. Zhu**, C. Wang and J. Huang. "Synthesis and TEM in-situ investigation of lithiation in $FePO_4$" (Oral), The 220th ECS meeting, Boston, MA 2011.
3. **Y. Zhu** and C. Wang, "Novel cyclic voltammetry study for phase transformation electrode" (Oral), The 218th ECS meeting, Las Vegas, NV 2010.
4. **Y. Zhu** and C. Wang, "Kinetics of phase transformation electrodes" (Oral), AIChE Annual Conference, Nashville, TN 2009.